Imperial College of Science, Technology and Medicine
Department of Materials

Enhancing Room-temperature Solid-state Maser: Approaches in Multiphysics Simulation, Zero-Field Time-Resolved EPR Spectroscopy, and Quantum-Cumulant Modeling

Xiaotian Xu

Submitted in part fulfilment of the requirements for the degree of
Doctor of Philosophy in Materials of Imperial College London, October 2024

Abstract

Masers, the microwave analogues of lasers, have attracted significant attention following the discovery of gain materials that operate at room temperature and zero magnetic fields. However, no room-temperature maser design has yet demonstrated continuous operation with robust performance suitable for practical applications. This thesis presents three approaches to enhance room-temperature solid-state masers.

A novel design for the maser cavity using piezoelectric materials is proposed. Correspondingly, a simulation tool based on weak forms and finite-element-method (FEM) software has been developed. This tool surpasses the limitations of the quasi-static approximation. It enables accurate prediction of the magnetic field strength generated by the piezoelectric cavity, which can directly interact with maser gain materials. Three test cases illustrate the accuracy and capability of this tool. Although this new design ultimately demonstrates limited magnetic energy conversion efficiency, the simulation tool offers broad applicability in designing antennas, resonators, and waveguides that utilize bulk or surface acoustic waves.

Another approach is to find new maser gain materials. Zero-field time-resolved electron paramagnetic resonance (ZF-trEPR) spectroscopy provides a quick inspection of their potential performance, especially the spin-lattice relaxation and depopulation rates. The theoretical background and experimental procedures are introduced. The ZF-trEPR was conducted on various candidate materials, with relatively strong signals observed for 0.01% mol/mol 6,13-diazapentacene-doped para-terphenyl (DAP:PTP), 0.1% mol/mol 5,12-diazatetracene-doped 1,3,5-tri(1-naphthyl)benzene (DAT:1-TNB), 0.1% mol/mol 1,5,12-triazatetracene-doped 1,3,5-tri(1-naphthyl)benzene (TrAT1:1-TNB), and 0.1% mol/mol 2,5,12-triazatetracene-doped 1,3,5-tri(1-naphthyl)benzene (TrAT2:1-TNB). The results are presented and analyzed in detail.

The quantum-cumulant method, implemented using the *Julia* programming language and the *QuantumCumulant.jl* package, is employed to simulate maser signals. This approach validates the masers' theoretical framework and predicts the masing performance of potential materials. It can provide a guide to on further research. A comprehensive guide is provided, accompanied by results from simulations of complex models that are not tractable through analytical methods.

Declaration

I, Xiaotian Xu, hereby declare that all the work presented here is my own, and that all else is properly referenced.

Copyright

The copyright of this thesis rests with the author. Unless otherwise indicated, its contents are licensed under a Creative Commons Attribution-NonCommercial 4.0 International Licence (CC BY-NC).

Under this licence, you may copy and redistribute the material in any medium or format. You may also create and distribute modified versions of the work. This is on the condition that: you credit the author and do not use it, or any derivative works, for a commercial purpose.

When reusing or sharing this work, ensure you make the licence terms clear to others by naming the licence and linking to the licence text. Where a work has been adapted, you should indicate that the work has been changed and describe those changes.

Please seek permission from the copyright holder for uses of this work that are not included in this licence or permitted under UK Copyright Law.

Acknowledgements

As I reach the end of my PhD journey, I reflect on these past four years as both a deeply rewarding and profoundly challenging period in my life. If I could offer a single piece of advice to young, ambitious PhD researchers, it would be this: the academic path is a long and often uncertain one, full of doubts and failures. Success requires both perseverance and a bit of luck. So, keep going, work hard, and best of luck on your journey forward!

I would like to express my deepest gratitude to my supervisor, Professor Mark Oxborrow. He guided me with patience and care, introducing me to the world of research and supporting me through each step. His mentorship allowed me to explore independently while providing a steady foundation, for which I am profoundly thankful. He generously shared his experience, insights, knowledge, and support, which have become the most valuable assets in my academic journey.

I would like to extend my sincere thanks to Professor Neil Alford. Your support has been invaluable to my career, and I am deeply grateful for the encouragemtn you have provided.

I extend my sincere condolences to my esteemed co-supervisor, Professor Norbert Klein. Your dedication, expertise, and unwavering commitment to the college have inspired countless young individuals to pursue their research passions, much like you. Your legacy will continue to shape the future of academia. May your soul rest in peace.

I would like to extend my gratitude to my mom and dad. Reaching this milestone would not have been possible without standing on your shoulders. You have been there for me through every high and low, providing unwavering support and guidance. You have shaped the person I am today, and I am committed to making you proud.

I would also like to say thanks to my senior colleagues, Eric, Wern, and Max. They have collaborated with me on EPR projects and have consistently shared their insights and ideas with me without reservation. They have served as mentors, providing inspiration and guidance as I strive to achieve my professional goals. I am also deeply thankful to my colleagues, Louis and Michael—working alongside you has been one of the most enjoyable aspects of this journey.

Last but certainly not least, I want to express my heartfelt thanks to my girlfriend, Yixuan, and our cat, Meeska. Your companionship has been like starlight, illuminating even the darkest

nights. Yixuan, your perspectives, often from areas beyond my research, have broadened my understanding and provided me with a more comprehensive view of the world. Deeply thank you for being my constant support.

‘Science is the search for truth.’

Linus Pauling

Contents

Abstract i

Declaration ii

Copyright iii

Acknowledgements iv

1 Introduction 1

1.1 Room-temperature Solid-state Masers 1

1.2 Stimulated Emission and Population Inversion 1

1.3 Zeeman Effect and Zero-field Splitting 3

1.4 Maser Dynamics 5

1.5 Maser Experiment Setup 7

1.6 Challenges 8

1.7 Statement of Originality 10

1.8 Publications 10

2 Simulating Magnetic Fields Around Piezoelectric Devices 12

2.1 Introduction 13

2.1.1 Proposed Design . . . 15
2.1.2 The Challenge . . . 16
2.2 Theory . . . 17
2.2.1 Constitutive Relations . . . 17
2.2.2 Christoffel Equations . . . 19
2.2.3 Rotation of Coordinates . . . 20
2.2.4 Solutions to the Christoffel Equations . . . 22
2.2.5 Quasi-static approximation . . . 23
2.2.6 Weak Forms . . . 23
2.2.7 Derivation of Weak Forms . . . 24
2.2.8 Penalty Terms . . . 26
2.2.9 Boundary Conditions . . . 26
2.2.10 M-field Method . . . 29
2.2.11 Magnetic Coupling Coefficient . . . 29
2.3 Historical Methods . . . 30
2.3.1 Superposition of Partial Waves . . . 30
2.3.2 Transverse Resonance Method . . . 30
2.4 How to Build a Model . . . 31
2.4.1 Selecting Physics . . . 32
2.4.2 Defining global parameters and variables. . . . 32
2.4.3 Rotating material coordinates . . . 36
2.4.4 Building models . . . 37

2.4.5 Configuring Weak Forms . . . 38
2.4.6 Analysing Methods . . . 40
2.5 Results . . . 41
2.5.1 Partial waves . . . 42
2.5.2 Rayleigh Mode on an Infinitely Large Substrate . . . 44
2.5.3 Torsional Mode of a Cylinder Antenna . . . 47
2.5.4 Relation between mesh size and error . . . 52
2.5.5 Relation between mesh size and calculation time . . . 53
2.6 Conclusion . . . 54

3 Zero-field Time-resolved EPR Spectroscopy 56

3.1 Introduction . . . 56
3.2 Theory . . . 57
3.2.1 Relaxation . . . 57
3.2.2 Rate Equations of the Triplet State . . . 61
3.2.3 Detection . . . 63
3.3 Instrumentation . . . 65
3.3.1 Middle Frequency Range . . . 65
3.3.2 Lower Frequency Range . . . 68
3.4 EPR Procedure . . . 68
3.4.1 Preparation . . . 69
3.4.2 Balancing . . . 69
3.4.3 Measurement . . . 70

3.4.4 Verification . . . 72
3.5 Results . . . 73
3.5.1 DAP:PTP . . . 73
3.5.2 DAT, TrAT1 and TrAT2 doped 1-TNB . . . 76
3.6 Conclusion . . . 78

4 Simulation of Maser Dynamics 80

4.1 Introduction . . . 80
4.2 Collective Effect: Tavis-Cummings Model . . . 81
4.2.1 Hamiltonian . . . 81
4.2.2 The Master Equation with Lindblad Form . . . 84
4.2.3 Solving the Master Equations . . . 86
4.3 Quantum-Cumulant Method . . . 89
4.3.1 Introduction . . . 89
4.3.2 Workflow . . . 90
4.3.3 Solving the Equations . . . 94
4.4 Discussion . . . 95
4.4.1 Maser Dynamics of Two-level and Three-level Pc:PTP Maser . . . 95
4.4.2 Error of Rotating-wave Approximation . . . 96
4.4.3 Maser Dynamics of NV Diamond Maser . . . 99
4.5 Conclusion . . . 104

5 Conclusion 106

A Properties of Some Piezoelectric Materials **109**

A.1 PZT-5H . . . 109

A.2 $LiNbO_3$ . . . 111

B Spintronic Parameters **114**

B.1 Pc:PTP . . . 114

B.2 Nitrogen-Vacancy Centres in Diamond . . . 115

C Code of the Quantum Cumulant Method **116**

C.1 Two-level Pc:PTP Maser . . . 116

C.2 Sevel-level NV Diamond Maser . . . 118

D Code of PyVisa **122**

Bibliography **124**

List of Tables

2.1 The Correspondence in Voigt notation. 17

2.2 Global parameters. In this table, `q` is a converter for global rotation from degrees into radians, `degree` is the angle of global rotation, `freq_t` is the estimated frequency in absorbing boundary condition, and `omega_t` is a converter for estimated frequency from Hz into rad/s. 33

2.3 Global variables for finding the global maximum values. In this table, `m` denotes the maximum, `E`, `D`, and `H` are the electric field strength, electric displacement field and magnetic field strength, respectively. 34

2.4 Global variables used in an acoustic field. 34

2.5 Global variables used in an internal electromagnetic field. 35

2.6 Global variables used in an external electromagnetic field. 35

2.7 Global variables required in the application of Absorbing Boundary Conditions. 36

2.8 Global parameters representing the reduced form of the stiffness tensor. 37

2.9 Global parameters representing the reduced form of the coupling tensor. 38

2.10 Global parameters representing the reduced form of the permittivity matrix. . . 38

2.11 Energy densities in the internal fields. 41

2.12 Energy densities in the external fields. 41

2.13 The properties of three partial wave modes propagating along the X-axis on PZT-5H ceramic, the acoustic energy dominates. 42

2.14 Comparison between velocities obtained from methods. 46

2.15 The coupling coefficients for Rayleigh mode with different materials. 48

3.1 Spintronic parameters on DAT:1-TNB, TrAT1:1-TNB, and TrAT2:1-TNB. These parameters were derived by fitting each transition's most intense ZF-trEPR signals to the rate equations. 78

B.1 Spintronic parameters of pentacene-doped *para*-terphenyl (Pc:PTP) 114

B.2 Spintronic parameters of nitrogen-Vacancy centres in diamond 115

List of Figures

1.1 The depiction of stimulated emission. Amber circles labelled with "e" represent electrons, while yellow circles labelled "$h\nu$" represent photons. Initially, more electrons reside in the higher energy level, E_2. As a photon travels through the two-level system, it simulates one electron to transit down to the lower energy level, E_1, resulting in the emission of another photon. 2

1.2 At room temperature and zero magnetic field, the ground state energy levels of the NV^- centre consist of a lower-energy state $|0\rangle$ and degenerate higher-energy states $|\pm1\rangle$, shown as the portion of the image to the left of the dashed line. Due to Boltzmann statistics and optical pumping, approximately 80% of electrons occupy the $|0\rangle$ state [1]. To achieve population inversion, an external magnetic field (the x-axis represents its strength) is applied along one of the four axes of the NV^- defects, causing Zeeman splitting of the $|\pm1\rangle$ states. When the magnetic field exceeds 102.5 mT, the energy of the $|-1\rangle$ state drops below that of the $|0\rangle$ state, resulting in population inversion [1]. 3

1.3 The Jablonski diagram of Pentacene. Reprinted with permission from [2]. Copyright 2012, Springer Nature. 6

1.4 The distribution of (a) the electric field strength and (b) the magnetic field strength on a cross-section. The warmer the colour, the stronger the fields. Red arrows in the subfigure (b) indicate the direction and magnitude of the magnetic field. Inner rectangles are the boundaries of the dielectric ring, and the outer ones are the metal cavity walls. These figures show that the electric field populates at the dielectric ring in a ring shape, whereas the magnetic field is concentrated at the gain material. 8

1.5 The typical structure of a maser (left), and a closer look at the Pc:PTP placed in a dielectric ring (right). Reprinted with permission from [2]. Copyright 2012, Springer Nature. 8

2.1 The illustration of the proposed piezoelectric maser resonator. The main parts are a piezoelectric substrate (grey rectangle) and a gain material (purple rectangle). The IDTs consist of two interlocking comb-shaped arrays of metallic electrodes connected to opposite voltages. They receive RF signals and periodically generate alternating electric fields during operation, which induce mechanical vibrations via piezoelectricity. 15

2.2 The illustration for properties of three partial waves, including their velocities and vibrations in the acoustic, electric, and magnetic fields. The colour bar indicates the amplitude of the vibrations. Our method, combined with COMSOL, is used to obtain these results. 43

2.3 A similar illustration for details of three partial waves. The COMSOL with built-in *Solid Mechanics* and *AC/DC* packages are used. The blue in the electric field of the third partial wave shows the absence of the result, suggesting an inadequacy in the simulation method. 44

2.4 A sketch of the Rayleigh mode being modelled in this paper. 44

2.5 (a) Geometry of the infinitely large substrate model. "A" and "B" symbolise the areas of the piezoelectric substrate and air, respectively. The simulation results of normalised (b) acoustic wave, (c) electric wave and (d) magnetic wave patterns for the Rayleigh mode on X-prop Z-cut $LiNbO_3$ are shown. Fields with larger magnitudes have warmer colours. Note that these three waves already decayed significantly before reaching $LiNbO_3$-air interface. Relative to the buried magnetic field in the substrate, the accessible magnetic field in the head space above is thus substantially weaker. 46

2.6 Comparison of simulated (blue line) and measured [3] (amber triangles) Rayleigh velocities corresponding to different propagating directions on 128° Y-cut $LiNbO_3$. In the simulation, the propagating direction is initially along the X-axis and then rotates anti-clockwise. 47

2.7 A sketch of the cylinder antenna being modelled in this paper. An axially symmetric normal mode is shown. 48

2.8 Normalised (1) acoustic displacement field, (2) electric field, and (3) magnetic field on the YZ section of a PZT-5H cylinder. Regions with larger magnitudes have warmer colours. The height and radius of this cylinder are 5 mm and 10 mm, respectively. The frequency of this mode is 175.12 kHz. Rotation directions on different sides are opposite from each other. The torsion generates a rotational electric field concentrated at the arc-shaped surface of the cylinder. This solenoid-like electric field then induces a magnetic field concentrated at the centre. 49

2.9 How frequency (orange circles) and magnetic coupling coefficient (blue triangles) vary with aspect ratio for the T_{00} torsional mode of a PZT-5H cylinder with a 10 mm radius. By connecting solid orange and blue lines, respectively. The sphere's radius containing the analysed air space surrounding the cylinder is 300 mm. When the aspect ratio decreases (*i.e.* the cylinder becomes squatter), both the frequency and the magnetic coupling coefficient increase. The magnetic coupling coefficient can reach 2.6×10^{-7} when the aspect ratio is 0.1. This value is extremely small, although it is the largest coupling coefficient ever observed. Given the difficulty in generating the T_{00} torsional mode on a very thin device, simulating a cylinder with an even smaller aspect ratio is considered unnecessary. Note that the coupling coefficient mainly depends on the aspect ratio rather than the frequency. Changing the size, and thus the frequency, does not affect the coupling coefficient. 50

2.10 The stimulated frequencies-thickness product of three axial symmetric normal modes versus inverse aspect ratio (black curves). Simulations were performed in a barium titanate cylinder whose height was fixed (5 mm). Results are compared with experimental results (brown circles) measured by Shaw [4]. 51

2.11 Normalised acoustic displacement fields of two axial symmetric normal modes versus normalised radius on the upper surface of a barium titanate cylinder. The results were obtained from our method (blue curves) and Shaw's experiments[4] (maroon squares). The height of the cylinder was set as 5 mm, and the inverse aspect ratio was set as $2r/h = 3.86$. The two modes were found at the frequency-thickness product (a) 2685 Hz×m and (b) 2885 Hz×m. 51

2.12 The plot of logarithmic relative error versus mesh size on (a) PZT-5H and (b) ZnO. The results of our method (green) and built-in *Piezoelectric Effect* interface (pink) are included. The left subplot in each figure illustrates all results, and the right one only focuses on results with smaller mesh sizes. 52

2.13 The plot of calculation time versus the maximum mesh size on (a) PZT-5H and (b) ZnO. The results of our method (blue) and built-in *Piezoelectric Effect* & *Magnetic Field* interfaces (orange) are included. 54

3.1 (a) The figure illustrates the measurement of relaxation time $\mathcal{T}_1$. The x-axis represents the delay time, while the y-axis shows the probabilities of finding the state $|1\rangle$. The blue points correspond to the measurement results of 30 qubits, and the green dashed line represents the fitted curve. The fitting process determines that $\mathcal{T}_1 = 129.75$ µs. This data is derived from a simulation conducted on FakeLagosV2 using Qiskit (Qiskit, 2024). (b) The figure visualises the spin-relaxation process corresponding to this measurement. Initially, the state vector points along the x-axis and gradually transitions towards the z-axis, demonstrating the relaxation dynamics. 59

3.2 An illustration of the spin-spin relaxation mechanism. Initially, multiple spins are aligned along the x-axis (represented by the red vector). Over time, due to interactions between spins, they begin to spread out, eventually reaching the positions indicated by the green vectors. This dispersion of spins leads to the gradual loss of the initial spin coherence. 60

3.3 The details of applying dynamic decoupling. Assume there is only the spin-spin relaxation. The process is visualised on a Bloch sphere in the first line, with the corresponding pulse sequence shown in the second line. A $\pi/2$ pulse is initially applied to rotate the spins from the z-axis to the x-axis. Subsequently, spin-spin relaxation causes the spins to rotate at different rates. After a delay of t seconds, a π pulse is applied, which inverts the spins. Following another delay of t seconds, the spins reunite along the negative x-axis, signifying the reconstruction of quantum coherence. 60

3.4 Illustration of the rates affecting the population densities of the triplet state T_1. Blue arrows represent transitions among the triplet sublevels, yellow arrows the ISC from the excited singlet state S_1, and green arrows show the decay processes from the triplet state to the ground state S_0. 61

3.5 The internal structure of the EPR spectrometer. 65

3.6 A photo of the LC resonator with labelled main components and its abstract circuit. The image also indicates the connections to the DC bias and stub tuner. 67

3.7 The internal structure of the EPR spectrometer when the spectrum analyser is connected. The cable linking the bandpass filter and the power splitter is disconnected (indicated by a blue cross). Instead, the spectrum analyser is connected to the bandpass filter via an isolator (both in blue). 70

3.8 An example of a detected signal. The signal is present on channel 2 (in blue). Its characteristic feature is a sudden increase or decrease in voltage at $t = 0$ (indicated by the yellow arrow labelled "T"), followed by a gradual decay to the baseline. Channel 3 (in magenta) shows no signal and is close to zero voltage. An average of 32 times was used in this measurement. 71

3.9 A waterfall plot of a group of signals. The colour and y-axis denote the voltage. The signal at 1478 MHz has the largest amplitude. Four adjacent signals at higher frequencies and four at lower frequencies are measured. A step size of 2 MHz is used because the signals are relatively strong with narrow bandwidth. This group of signals was measured on DAP:PTP. 72

3.10 (a) The EPR signal of DAP:PTP measured at 1478 MHz (black curve). This signal is rescaled with the peak voltage equal to the maximum population difference between T_z and T_x (0.41[5]). A bi-exponential fitting (green curve) was plotted to estimate the spin dynamics. Other measured peak voltages are plotted in the inset figure and fitted with a Gaussian curve. (b) A closer look at the peaks of the signal at 1478 MHz and its two adjacent signals. Reprinted from [6] under the terms of the Creative Commons CC-BY 4.0 license. Copyright 2023, John Wiley & Sons, Ltd. 74

3.11 ZF-trEPR signals of DAP:PTP collected under the same experimental conditions as in Figure 3.10, but with different input microwave powers. Oscillations occur at all microwave powers. The inset plot illustrates the relation between peak trEPR voltage and the square root of the input microwave power (in watts). The proportional relation is violated when the input power is higher than -20 dBm, which indicates the onset of power saturation. Reprinted from [6] under the terms of the Creative Commons CC-BY 4.0 license. Copyright 2023, John Wiley & Sons, Ltd. 74

3.12 Structures of 1,3,5-Tri(1-naphthyl)benzene (1TNB) Host Molecule and N-Substituted Tetracene Derivatives. Reprinted from [7] under the terms of the Creative Commons CC-BY 4.0 license. Copyright 2023, American Chemical Society. 76

3.13 The captured most intense ZF-trEPR signals for DAT:1-TNB (blue), TrAT1:1-TNB (green) and TrAT2:1-TNB (red). Other measured peak voltages are shown in the insert figure. Reprinted from [7] under the terms of the Creative Commons CC-BY 4.0 license. Copyright 2023, American Chemical Society. 77

4.1 The time evolution of two quantum quantities: the probabilities of a photon existing in the cavity (blue) and the spin being in an excited state (orange). These two quantities oscillate with time but always add up to 1. These results were calculated using Equation 4.1 and a Python package named QuTiP [8]. This method is going to be introduced in Section 4.2.3. 82

4.2 The time evolution of (a) the number of photons, (b) the spin-photon correlation, (c) the spin-spin correlation, and (d) the spin population inversion. These results were obtained using the `solve_ivp` function combined with the RK45 method. The initial values are $\langle a^\dagger a \rangle = 4300$, $\langle S_+ S_- \rangle = 0$, $\langle S_+ S_- \rangle = 0$, and $\langle S_z \rangle = 0.8$. . . 89

4.3 The simulation results of the maser dynamics, including (a) number of photons, (b) spin-photon correlation, (c) spin-spin correlation, and (d) inversion, are compared between the two-level and three-level maser models. The results obtained from the two-level maser are coloured blue, while those from the three-level maser are coloured orange. These results show differences in amplitudes between the two results. 97

4.4 (a) An overview of the computational error of the RWA over the time interval from 0 to 10 microseconds. There are oscillations present, with an initial sharp increase followed by oscillatory behaviour that gradually damps out. The oscillations exhibit a significant amplitude initially, which decreases over time. And (b) a detailed view focusing on the time range from 2.25 to 2.6 microseconds. This plot reveals a more stable, finer oscillatory pattern imposed on the larger oscillation. 99

4.5 A setup of the NV^- diamond maser. The diamond is placed within a hollow cylindrical sapphire dielectric resonator, with both the sapphire resonator and the diamond enclosed in a copper cavity. The diamond is precisely oriented so that one of the NV$\langle 111 \rangle$ axes is parallel to an externally applied static magnetic field of at least 102.5 mT. A continuous-wave 532 nm Nd:YAG laser is employed for optical pumping, thus polarizing electrons in the NV^- centers. Maser emission is extracted from the cavity using a microwave loop antenna coupled to a transmission line. 100

4.6 (a) The atomic structure of an NV centre in diamond. It consists of a nitrogen atom (blue) situated next to an empty lattice site (light grey) and surrounded by carbon atoms (black). (b) The Jablonski diagram of NV centres. An NV center has a triplet ground state $^3A_2$, a triplet excited state ^3E, and two singlet states $^1A_1$ and ^1E. The ground state has three projection numbers $m_s = 0, \pm 1$ along the NV quantization axis. (c) A magnified plot of the triplet ground state $^3A_2$. The Zeeman effect appears when a magnetic field is present, causing $|+\rangle$ and $|-\rangle$ to differ. Reprinted with permission from [1]. Copyright 2018, Springer Nature. 100

4.7 The Jablonski diagram of NV centres in the presence of a magnetic field is shown. For modelling purposes, each state and sublevel is assigned an index. The diagram also depicts the pumping and damping rates. Reprinted with permission from [9]. Copyright 2024, China Science Publishing & Media LTD. 101

4.8 The maser dynamics over 12 ms period for (a) photon number. Oscillation and exponential decay are observed simultaneously. (b) the population of sublevels $|1\rangle$ (blue), $|2\rangle$ (orange), and $|3\rangle$ (green). 103

Chapter 1

Introduction

1.1 Room-temperature Solid-state Masers

A maser, an acronym for Microwave Amplification by Stimulated Emission of Radiation, is the microwave analogue of the laser. The first prototype of the maser was built in 1953, and the 1964 Nobel Prize was awarded for the theoretical work that led to its development. However, in the following decades, masers did not see widespread development, mainly because the required operation conditions (may not be on the same setup) limited their practicality [2, 10], including vacuum chambers, cryogenic environment, and strong magnets. In 2012, a zero-field room-temperature solid-state maser was demonstrated [2]. This maser operates at 1.45 GHz with optical pumping and utilizes pentacene-doped *para*-terphenyl (Pc:PTP) crystal as the gain material. Since then, other maser gain materials working at room temperature have been sought [11, 5, 12, 13], including NV-diamond [1] and diazapentacene-doped *para*-terphenyl [6].

1.2 Stimulated Emission and Population Inversion

As their name suggests, masers use stimulated emission to amplify microwaves. Stimulated emission occurs through the interaction between the two-level systems and photons. Consider

a photon travelling across a two-level system with electrons at both energy levels, as depicted in Figure 1.1. During stimulated emission, an electron in the upper energy level is stimulated and transits downward to the lower energy level, resulting in the emission of an additional photon. Consequently, this process converts one photon into two, thereby achieving amplification.

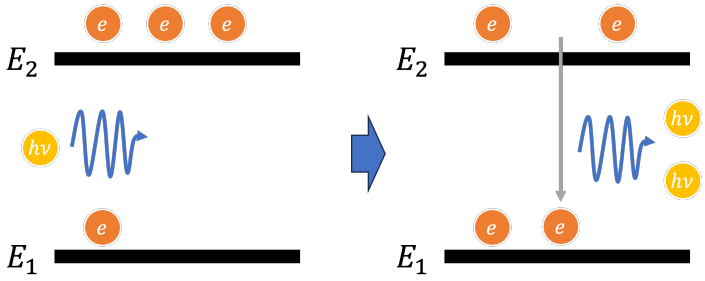


Figure 1.1: The depiction of stimulated emission. Amber circles labelled with "e" represent electrons, while yellow circles labelled "$h\nu$" represent photons. Initially, more electrons reside in the higher energy level, E_2. As a photon travels through the two-level system, it simulates one electron to transit down to the lower energy level, E_1, resulting in the emission of another photon.

However, stimulated absorption occurs simultaneously, where an electron at the lower energy level is stimulated to transition upward, absorbing one photon. The net effect of these processes depends on the relative populations of the energy levels. Specifically, the rate of stimulated emission is proportional to the population of the upper energy level, whereas the rate of stimulated absorption is proportional to the population of the lower energy level, both sharing the same proportionality constant [14]. For amplification to occur, there must be more electrons in the upper energy level, a condition known as population inversion.

However, population inversion is typically absent due to the Boltzmann distribution, mathematically expressed as Equation 1.1. In this equation, p_i and E_i indicate the population density and energy of the i-th level, respectively. k_B is the Boltzmann constant and T is the temperature in Kelvins. This equation suggests that, at thermal equilibrium, fewer electrons occupy the upper energy level.

$$\frac{p_i}{p_j} = \exp\left(-\frac{E_i - E_j}{k_B T}\right) \tag{1.1}$$

1.3 Zeeman Effect and Zero-field Splitting

The population inversion can be generated by the Zeeman effect, where electrons with different spin quantum numbers have different energy shifts when exposed to the external magnetic field [15].

$$E = -g\mu_B B_0 m_s \tag{1.2}$$

In this equation, g denotes the g-factor, μ_B denotes the Bohr magneton, B_0 is the magnetic flux density, and m_s is the spin quantum number. The Zeeman effect can alter the ordering of energy levels in certain materials, leading to population inversion. The nitrogen-vacancy (NV^-) defect centre in diamond is an example, as shown in Figure 1.2 [16, 1]. Although the Zeeman effect can be leveraged to build masers, the application of an external magnetic field introduces inconvenience to the experimental conditions.

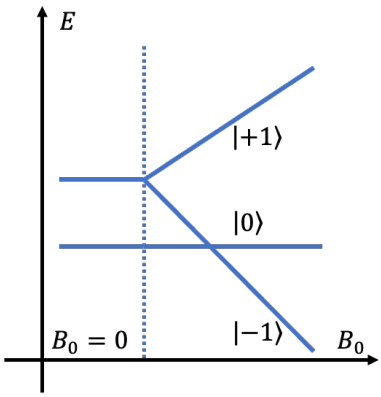


Figure 1.2: At room temperature and zero magnetic field, the ground state energy levels of the NV^- centre consist of a lower-energy state $|0\rangle$ and degenerate higher-energy states $|\pm1\rangle$, shown as the portion of the image to the left of the dashed line. Due to Boltzmann statistics and optical pumping, approximately 80% of electrons occupy the $|0\rangle$ state [1]. To achieve population inversion, an external magnetic field (the x-axis represents its strength) is applied along one of the four axes of the NV^- defects, causing Zeeman splitting of the $|\pm1\rangle$ states. When the magnetic field exceeds 102.5 mT, the energy of the $|-1\rangle$ state drops below that of the $|0\rangle$ state, resulting in population inversion [1].

In zero-field room-temperature masers, zero-field splitting (ZFS), caused by spin-orbital coupling and dipolar interactions between unpaired electrons [17], is leveraged. ZFS can be de-

scribed by a Hamiltonian [17]:

$$H_{\mathrm{ZFS}} = \hat{S}D\hat{S} = D_x S_x^2 + D_y S_y^2 + D_z S_z^2 \tag{1.3}$$

where $\hat{S}$ is the spin vector operator. D is the zero-field splitting tensor, which is a diagonal tenser with its components D_x, D_y, and D_z located on its diagonal. This tensor is generally traceless [18, 19], and thus two parameters D and E are enough to denote the ZFS Hamiltonian. They are defined as:

$$H_{\mathrm{ZFS}} = D\left(S_z^2 - \frac{1}{3}\hat{S}^2\right) + E\left(S_x^2 - S_y^2\right) \tag{1.4}$$

$$D = \frac{3}{2}D_z \tag{1.5}$$

$$E = \frac{1}{2}(D_x - D_y) \tag{1.6}$$

These two parameters D and E are collectively called the ZFS parameters. The energies of three triplet state sublevels concerning the centre of gravity (point of zero energy), which are also the eigenvalues of the ZFS Hamiltonian [17], are:

$$E_x = \frac{1}{3}D - E \tag{1.7}$$

$$E_y = \frac{1}{3}D + E \tag{1.8}$$

$$E_z = -\frac{2}{3}D \tag{1.9}$$

And their corresponding eigenstates are denoted as T_x, T_y, and T_z. In Convention, T_x has the largest energy separation from the centre of gravity, then T_y, and T_x has the least [17]. This convention suggests that the signs of D and E are always different, and the absolute value of E is bounded by $\frac{1}{3}$ of the absolute value of D [17, 20]. For building a maser, the energy differences attract more interest, and they are calculated as:

$$T_x - T_z \rightarrow E_x - E_z = |D| + |E| \tag{1.10}$$

$$T_y - T_z \rightarrow E_y - E_z = |D| - |E| \tag{1.11}$$

$$T_x - T_y \rightarrow E_x - E_y = 2|E| \tag{1.12}$$

1.4 Maser Dynamics

The triplet state generated by ZFS is leveraged to build population inversion. Here Pc:PTP is used as an example to explain the dynamics behind, whose Jablonski diagram is shown in Figure 1.3. Initially, electrons predominantly reside in the ground state, S_0. A pumping laser beam excites the electrons to the singlet excited state S_1. This laser beam should have a wavelength close to the corresponding transition energy, which is 585 nm for Pc:PTP. Some electrons decay directly back to the S_0 state via either stimulated or spontaneous optical emission, with photoluminescence emitted. Whereas, others transit to a triplet state $\mathcal{T}_2$, through a mechanism known as intersystem crossing (ISC), with an overall yield of approximately 62.5% [21]. This process is highly spin-selective, resulting in an isotropic population ratio of approximately 0.76 : 0.16 : 0.08 for T_x, T_y, and T_z, respectively [22]. In pentacene molecules, X, Y and Z denote the long in-plane axis, short in-plane axis, and out-of-plane axis, respectively [23]. For simplicity, this $\mathcal{T}_2$ state is not depicted in Figure 1.3. The ISC process is followed by rapid internal conversion (IC) to the lowest triplet state, $\mathcal{T}_1$, with the population ratio preserved. As the higher ratio is at the upper level, the prerequisite condition of a maser, the population inversion, is established. The triplet sublevels T_x and T_z are then utilized as a two-level system for masers. In the following chapters, electrons on these two states can be regarded as pseudo-spin-$\frac{1}{2}$ particles [24], and the term "spins" will be used for brevity. Note that the impact of ignoring the T_y sublevel is negligible, as will be demonstrated in Chapter 4.

Other materials used in room-temperature solid-state masers exhibit similar properties and are known as maser gain materials. Besides Pc:PTP, other maser gain materials such as NV-centers in diamond [25, 1, 26, 27, 28] and diazapentacene-doped *para*-terphenyl [6] have been discovered. Research on more materials is ongoing [7].

A threshold condition for whether a maser can operate is given by a quantity called the co-operativity, η_{mase}:

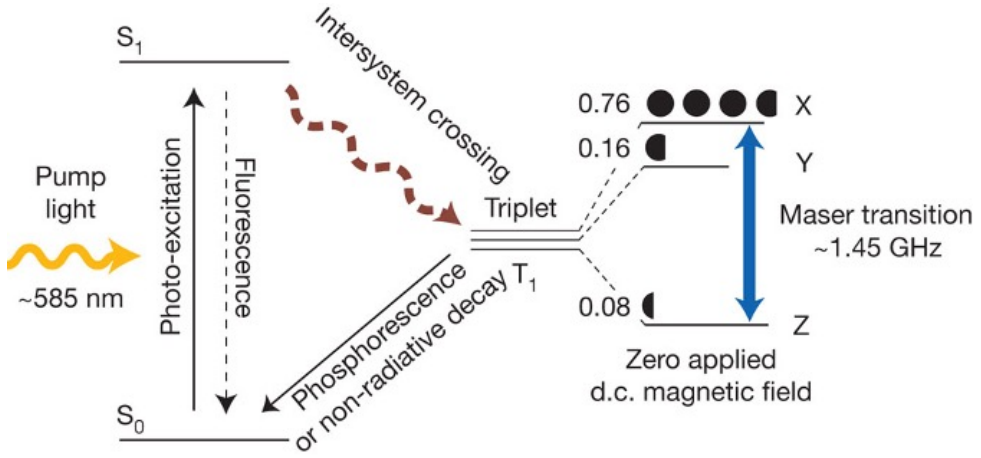


Figure 1.3: The Jablonski diagram of Pentacene. Reprinted with permission from [2]. Copyright 2012, Springer Nature.

$$\eta_{\text{mase}} = \frac{\mu_0 \gamma^2 \sigma^2}{2\pi} \times \frac{P_{\text{opt}}}{f_{\text{opt}}} \times (\kappa_{\text{opt}} \Theta_{\text{ISC}}^{\text{eff}}) \times (\mathcal{T}_1^{\text{eff}} \mathcal{T}_2) \times \frac{Q_L}{V_{\text{mode}}} > 1 \tag{1.13}$$

If $\eta_{\text{mase}} > 1$, the maser can operate. This co-operativity expression consists of five grouped factors:

- **First factor (physical constants):** This includes the vacuum permeability μ_0, the gyromagnetic ratio γ, vacuum magnetic permeability μ_0, and a constant $\sigma^2 = 0.5$ for triplet transitions.

- **Second factor (pump conditions):** This includes the optical pump power P_{opt} and the frequency of the pump light f_{opt}. These are not properties of the gain medium or the cavity.

- **Third factor (light-matter interaction):** This includes κ_{opt}, the absorption efficiency of the gain medium at the pump wavelength, and $\Theta_{\text{ISC}}^{\text{eff}}$, the effective probability that excited molecules reach the triplet state.

- **Fourth factor (spin dynamics):** This includes $\mathcal{T}_1^{\text{eff}}$, the effective spin-lattice relaxation time, and $\mathcal{T}_2$, the spin-spin relaxation time of the masing transition.

- **Fifth factor (cavity properties):** This includes the loaded quality factor Q_L, measured with the gain medium inside the cavity, and the magnetic mode volume V_{mode}.

1.5 Maser Experiment Setup

Figure 1.5 shows the structure of a maser. The main body is a metal cavity, depicted as the grey boxes in the figure. This cavity effectively suppresses decoherence but introduces another form of damping as it absorbs photons. A screw on the top controls the position of the lid, allowing for fine-tuning of the resonant frequency. The maser gain material (purple) is placed at the centre of the cavity. It is surrounded by a dielectric ring (light blue), typically made of sapphire or strontium titanate (STO). This dielectric ring supports the material and confines the electromagnetic fields around it, improving the coupling and reducing the damping of the electromagnetic field caused by the metal walls (as explained in the field distribution discussion below). The dielectric ring can also serve as a convex lens to converge the laser beams. It is lifted 3mm above the metal cavity by a Polystyrene support [29].

In the cavity, the $\text{TE}_{01\delta}$ mode is used for coupling. Figure 1.4 shows the electric and magnetic field distributions of this mode across a cross-section. The electric field is mainly located in the dielectric ring, forming a ring-like pattern, while the magnetic field is concentrated near the gain material. This field distribution is important for the fifth factor in Equation 1.13, which includes the cavity's quality factor Q and the magnetic mode volume V_m. The magnetic mode volume refers to the space where the magnetic energy is distributed, and it is defined as the total magnetic energy stored divided by the highest magnetic energy density [24]. Because the magnetic field is concentrated, the magnetic mode volume becomes smaller, which in turn increases the co-operativity and probability of a maser to operate.

When conducting maser experiments, a laser beam is directed onto the gain material through a hole in the cavity wall. This light beam is a pump, and it creates a population inversion in an extremely short time (approximately 5 ns), followed by the interaction between the gain material and the thermal photons. This interaction ultimately results in a strong resonance of

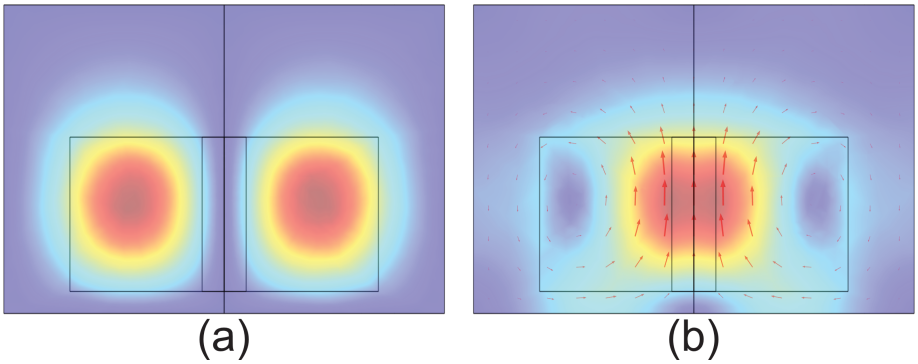


Figure 1.4: The distribution of (a) the electric field strength and (b) the magnetic field strength on a cross-section. The warmer the colour, the stronger the fields. Red arrows in the subfigure (b) indicate the direction and magnitude of the magnetic field. Inner rectangles are the boundaries of the dielectric ring, and the outer ones are the metal cavity walls. These figures show that the electric field populates at the dielectric ring in a ring shape, whereas the magnetic field is concentrated at the gain material.

the electromagnetic field, which is observed as the maser signal.

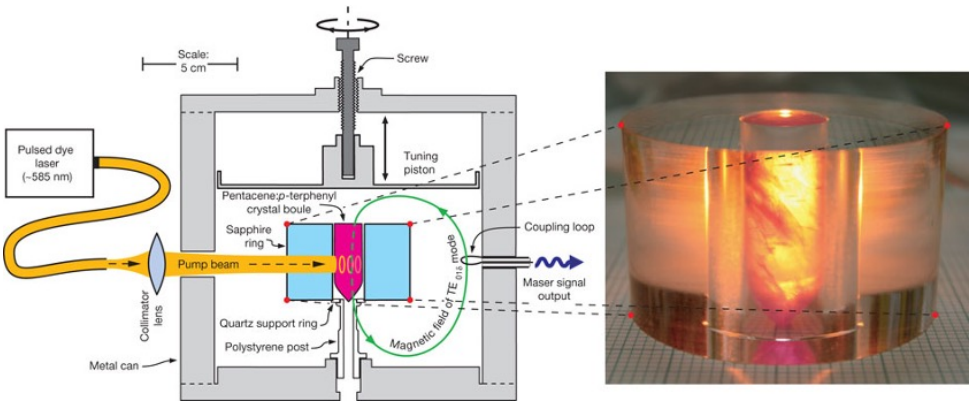


Figure 1.5: The typical structure of a maser (left), and a closer look at the Pc:PTP placed in a dielectric ring (right). Reprinted with permission from [2]. Copyright 2012, Springer Nature.

1.6 Challenges

Our ultimate goal is to build a powerful room-temperature continuous-wave maser, ideally without an external magnetic field applied. Although several materials have shown promise as maser gain media, an ideal material has yet to be identified. In 2018, a maser based on charged nitrogen-vacancy (NV^-) centres in diamond was demonstrated to work continuously [1]. However, this maser requires a uniform magnetic field of 430 mT with a relatively lower

output of -90.3 dBm [30]. Conversely, the output power of Pc:PTP maser can exceed -10 dBm [2], but due to "bottleneck" problem and poor thermal stability [25], the best record of it is working quasi-continuously with an output power of -25 dBm for approximately 4 ms [31].

To address this problem, we have several different approaches, and they are presented in the following chapters.

Chapter 2 introduces a novel design for maser cavities, where the cavities are constructed using piezoelectric materials. This new design has the potential to reduce the cavity's dimensions, which could significantly increase the Purcell factor (the 5th factor in co-operativity) and therefore increase the probability of masing. Since the maser gain materials interact solely with magnetic fields, a new simulation tool has been developed to calculate the efficiency of magnetic energy transformation. This tool is based on weak forms and can be integrated into any finite-element-method (FEM) software that supports weak forms. Three test cases are presented: (a) bulk partial waves propagating along the x-axis in PZT-5H, (b) the Rayleigh mode on an infinitely large substrate in various materials, and (c) the T_{00} torsional mode in a cylindrical piezoelectric antenna made from PZT-5H. These cases demonstrate that the new simulation tool enables the simulation of magnetic fields generated by piezoelectric materials—an ability not previously available due to the wide use of the quasi-static approximation—and that the tool exhibits satisfactory accuracy and capability.

Chapter 3 presents zero-field time-resolved electron paramagnetic resonance (ZF-trEPR) spectroscopy, a powerful characterization method for candidates of new maser gain materials. This technique examines how strong the population inversion is established in response to an optical pump and how quickly the system relaxes back to the ground state afterwards. By analyzing the signals, ZF-trEPR reveals spin-lattice relaxation (within the 3rd term of the co-opertivity) and depopulation rates and provides an estimate of the maser performance based on the signal strength. In this chapter, both the theoretical framework and experimental procedures are elaborated. Strong signals were observed in several materials, and their corresponding signals are illustrated and analyzed in this chapter.

Chapter 4 introduces the quantum-cumulant method, a simulation method for modelling maser

dynamics. This tool is built using the scientific computing language *Julia* and its *Quantum-Cumulant.jl* package. It automatically constructs and solves the master equation in Lindblad form. The chapter provides the theoretical background of this equation, along with a detailed guide on how to apply the quantum-cumulant method. The accuracy and capability of this method are demonstrated through three complex cases that cannot be solved analytically due to their complexity. This method offers valuable insights for optimizing maser performance in terms of both experimental setups and material properties.

1.7 Statement of Originality

In Chapter 2, the new design of maser cavities in piezoelectric materials was proposed by Professor Mark Oxborrow, and the rest were conducted by the author, including deriving the weak forms, implementing them into COMSOL, and proposing and analysing test cases.

During the ZF-trEPR experiments, the author built and calibrated the experimental instruments, summarizing valuable experience in the chapter. A total of eleven materials were tested, including the four discussed in detail. The data analysis was also conducted by the author. The author was not responsible for designing and synthesizing the materials.

The coupled differential equation method was first introduced in Carmichael's book [32] and later applied to maser dynamics in Breeze's paper [24]. The code for simulating maser dynamics in Julia and results in NV diamond was based on the work of Wu [9]. The author made corrections and additions to the original code, provided personal experiences and insights on the theory, developed the direct method using the *QuTiP* package, and presented the other two cases.

1.8 Publications

1. Xu X, Newns M, Oxborrow M. Simulating the magnetic fields generated by piezoelectric devices using FEM software: Beyond the quasistatic approximation[J]. Journal of Applied

Physics, 2022, 132(20).

2. Attwood M, Xu X, Newns M, et al. N-heteroacenes as an organic gain medium for room-temperature masers[J]. Chemistry of Materials, 2023, 35(11): 4498-4509.

3. Ng W, Xu X, Attwood M, et al. Move Aside Pentacene: Diazapentacene-Doped para-Terphenyl, a Zero-Field Room-Temperature Maser with Strong Coupling for Cavity Quantum Electrodynamics[J]. Advanced Materials, 2023, 35(22): 2300441.

4. Chen K C, Li X, Xu X, et al. Quantum-hpc framework with multi-gpu-enabled hybrid quantum-classical workflow: Applications in quantum simulations[J]. arXiv preprint arXiv:2403.05828, 2024.

5. Xu X, Chen K C, Wille R. HamilToniQ: An Open-Source Benchmark Toolkit for Quantum Computers[J]. arXiv preprint arXiv:2404.13971, 2024.

6. Chen K C, Xu X, Makhanov H, et al. Quantum-enhanced support vector machine for large-scale multi-class stellar classification[C]//International Conference on Intelligent Computing. Singapore: Springer Nature Singapore, 2024: 155-168.

7. Chen K C, Ma W, Xu X. Consensus-based Distributed Quantum Kernel Learning for Speech Recognition[J]. arXiv preprint arXiv:2409.05770, 2024.

Chapter 2

Simulating Magnetic Fields Around Piezoelectric Devices

This chapter introduces a method for simulating coupled electromagnetic and mechanical vibrations on arbitrarily shaped piezoelectric structures. This method is based on weak forms and can be implemented in any finite-element-method (FEM) software allowing customizable access to their definitions. No quasi-static approximation is imposed, meaning that magnetic fields generated by displacement currents within piezoelectric materials are captured, enabling the flow of electromagnetic energy inside and around structures containing such material to be accurately simulated. The method is particularly relevant to the design of piezoelectric antennas, resonators and waveguides exploiting either bulk or surface-acoustic waves (SAWs).

The structure of this chapter is outlined as follows: the background for developing this method and a brief introduction to piezoelectricity are provided in Sec. 2.1. The underlying theory is shown in Sec. 2.2. Sec. 2.4 consists of detailed instructions for using our method to build a model where COMSOL is employed for illustration purposes. Finally, Sec. 2.5 presents and analyses the results obtained from our method, validating the precision and showcasing the capability of simulating complicated devices.

2.1 Introduction

Why a Piezoelectric Cavity?

As previously mentioned, this thesis aims to enhance the maser's amplification strength. One potential approach is redesigning the maser cavity and minimizing its volume. This is because the maser's performance is evaluated by the Purcell factor, as defined in Equation 1.13. While the magnetic volume is not directly equivalent to the overall cavity volume, they are approximately related to the modes we are interested in. Therefore, the primary objective is to reduce the overall volume, which poses a significant challenge. To ensure effective resonance within a maser cavity, its dimensions must closely match the wavelength of the resonant waves, particularly in the microwave spectrum. Consequently, typical radii of metal cavities are several centimetres for frequencies ranging from 1-10 GHz. The volume reduction can only be substantial when another type of wave resonates in the cavity, and acoustic waves are a viable option.

The primary reason is that acoustic waves with the same frequency as electromagnetic waves have much smaller wavelengths. Given that the typical speeds of electromagnetic and acoustic waves in a solid medium are in the orders of $\sim 10^8$ m/s and $\sim 10^3$ m/s, respectively, this results in a wavelength difference by a factor of 10^5. Consequently, the size of a piezoelectric cavity operating at the same frequency is much smaller. This difference suggests that the magnetic mode volume could potentially be reduced to 10^{-15} of the original volume. Such a reduction also improves the portability of masers and paves the way for their integration within compact systems or even microchips [33].

Nevertheless, a critical challenge arises from the maser gain material's intrinsic limitation in interacting solely with the magnetic field. This limitation suggests the necessity of a piezoelectric cavity for hosting resonant acoustic waves while transforming between mechanical and magnetic energies. Predicting the coefficient of this transformation is essential to assess the feasibility of this approach.

Piezoelectricity

Piezoelectric materials are anisotropic crystals that facilitate energy transfer between acoustic (*i.e.* elastomechanical) and electromagnetic fields. When mechanical pressure or stress is applied to a piezoelectric material, its internal crystal lattice deforms slightly, causing a separation of positive and negative charge centres, which generates an electric voltage [34]. This effect is reversible; an applied electric field can also induce mechanical deformation in the material. Consequently, hybrid vibrations involving both electromagnetic and acoustic components can be induced by periodically applying mechanical stress or subjecting the material to an alternating electric field, typically produced by a pair of electrodes.

One example of electromagnetic-acoustic (EMA) coupling is a surface acoustic wave (SAW) on a piezoelectric substrate. Here, the hybrid wave is localised on the substrate's surface. The acoustic and the electromagnetic parts of such a SAW propagate along the surface with the same frequency and wavenumber. Each part is uniform in the transverse direction. Devices exploiting piezoelectric SAWs encompass delay lines, filters and resonators; such SAWs also provide a way of coupling phonons to artificial atoms [35] in quantum systems.

Another example of EMA coupling is a piezoelectric antenna. To radiate efficiently, the length of a conventional antenna needs to approach the wavelength of the electromagnetic wave being emitted. As mentioned, a piezoelectric antenna working at the same frequency has a much smaller wavelength. If such an antenna could radiate at reasonable efficiency (electromagnetically), it would offer enormous potential for the further miniaturisation of telecom devices.

Widely used piezoelectric materials include Lithium Niobate ($LiNbO_3$), Lithium Tantalate ($LiTaO_3$), the family of lead zirconate titanate (PZT-4, PZT-5A, and PZT-5H, where the term following the hyphen refers to a specific subtype), Cadmium Sulfide (CdS), and Zinc Oxide (ZnO).

2.1.1 Proposed Design

The design of the piezoelectric maser cavity needs to meet the following criteria: (a) the maser gain material is placed where the magnetic field concentrates. This place must be outside of the piezoelectric material since two materials cannot occupy the same space at the same time; (b) there must be somewhere on the cavity for fixing; (c) there must be somewhere for integrated transducers.

Based on these criteria, the first piezoelectric maser cavity design was proposed by Mark Oxborrow in 2020. The structure is shown in Figure 2.1. By sending an RF wave with the maser-operating frequency into the integrated transducers (IDTs), an EMA wave is excited on the substrate and propagates along one of the axes. Then, the EMA wave is reflected on the other side, forming a standing wave with the oncoming wave. An electromagnetic field is emitted from the upper boundary and coupled with spins in the gain material, which can begin to amplify after the population inversion is built by a pump light source. For minimum damping effects, the space between the electrodes of IDTs and the length of the standing-wave area need to suit the EMA wavelength. The gain material is held slightly above the substrate so the SAW will not be disturbed. The substrate needs to be held by a holder, meaning some parts should remain still during mechanical vibrations. The EMA wave modes intended for exploration in this design are the Rayleigh and Bleustein-Gulyaev modes.

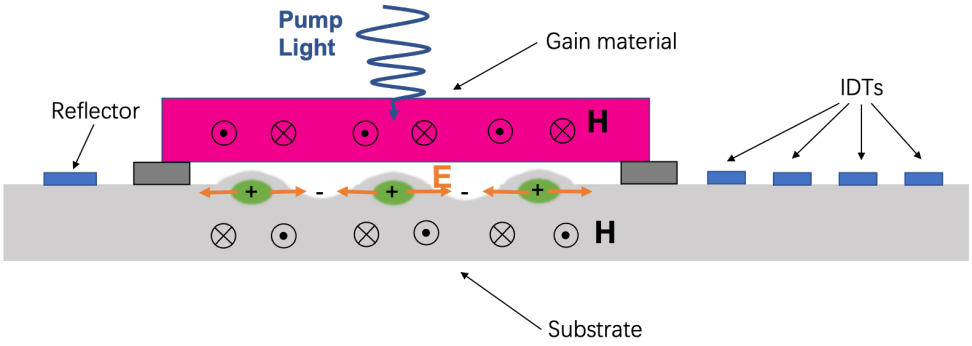


Figure 2.1: The illustration of the proposed piezoelectric maser resonator. The main parts are a piezoelectric substrate (grey rectangle) and a gain material (purple rectangle). The IDTs consist of two interlocking comb-shaped arrays of metallic electrodes connected to opposite voltages. They receive RF signals and periodically generate alternating electric fields during operation, which induce mechanical vibrations via piezoelectricity.

2.1.2 The Challenge

Owing to the anisotropy of the medium, the complete simulation of EMA coupling in piezoelectric devices can rarely be done analytically. The so-called quasi-static approximation is often applied to simplify the governing equations. Under this approximation, the magnetic field is neglected, and the electric field strength is represented as the negative gradient of the electric potential ϕ as $\underline{E} = -\nabla\phi$. In many piezoelectric applications, this approximation works well because the magnetic field stores far less energy than the electric field does [34]. However, in specific applications, such as antennas [36] or high magnetic-Purcell-factor resonators [37], knowledge of the magnetic field is crucial: one cannot calculate the devices' efficiency (radiation impedance) without it. The quasi-static approximation must be avoided.

Certain known analytical methods can precisely simulate the EMA coupling without invoking the quasi-static approximation. Examples include the superposition-of-partial-waves method [34] (introduced in Section 2.3.1), transverse-resonance method [38] (introduced in Section 2.3.2) and Kirchhoff-plate-theory method [39, 40] These methods are limited to particular spatial geometries and crystal classes (point group symmetry) –they cannot be extended to simulate arbitrary 3D structures or piezoelectric materials of a different class. Alas, many of the popular FEM-based simulation platforms, like COMSOL Multiphysics (both its Structural Mechanics and MEMs modules), implicitly invoke the quasi-static approximation, meaning that they cannot be used to simulate the complete electromagnetic behaviour of piezo-mechanical devices. A method for remedying this frustrating inadequacy is going to be introduced in this section. This method is applicable to any FEM simulation software where weak forms define the whole system of coupled partial differential equations. COMSOL is used here to provide explicit examples.

This work was published in the Journal of Applied Physics in 2022 [41]. Many contents (the figures, tables and text) in this chapter were reprinted with permission from [41] (Copyright 2024, AIP Publishing) and properly cited.

2.2 Theory

In this section, the number of underlines ("_") denotes the rank of a tensor. All rank 3 or 4 tensors are simplified using Voigt notation [42]. The correspondence can be found in Table 2.1.

I	ij
1	xx
2	yy
3	zz
4	yz, zy
5	xz, zx
6	xy, yx

Table 2.1: The Correspondence in Voigt notation.

2.2.1 Constitutive Relations

Piezoelectricity is the coupling between electric and mechanical fields, which is shown as generating electrical charge in response to applied mechanical stress and vice versa. This phenomenon exists in some anisotropic materials, such as quartz [43] and certain types of ceramics. The piezoelectric effect in these materials is quantified using a tensor known as the piezoelectric strain constants. This tensor is measured in [Coulomb/m^2] and represented as follows:

$$\underline{\underline{e}} = \begin{bmatrix} e_{11} & e_{12} & e_{13} & e_{14} & e_{15} & e_{16} \\ e_{21} & e_{22} & e_{23} & e_{24} & e_{25} & e_{26} \\ e_{31} & e_{32} & e_{33} & e_{34} & e_{35} & e_{36} \end{bmatrix} \tag{2.1}$$

Each element in this tensor is a real number and specifies the magnitude and direction of the charge generated when stress is applied in a particular direction and vice versa.

The coupling between electric and mechanical fields is described mathematically by two coupled equations known as the constitutive relations:

$$\underline{\underline{T}} = \underline{\underline{\underline{\underline{c}}}}^{E} : \underline{\underline{S}} - \underline{\underline{\underline{e}}}^{T} \cdot \underline{E} \tag{2.2}$$

$$\underline{D} = \underline{\underline{\underline{e}}} : \underline{\underline{S}} + \underline{\underline{\varepsilon}}^{S} \cdot \underline{E} \tag{2.3}$$

Here, the symbol ":" denotes the double dot product between two tensors. It is the summation of two pairs of subscripts (one pair in Voigt notation). Superscripts S and E have been added to $\underline{\underline{\varepsilon}}$ and $\underline{\underline{\underline{c}}}$ to show that these constants describe dielectric and elastic properties measured under conditions of constant strain and constant electric field, respectively [34]. In these relations, the acoustic field is characterised by strain $\underline{\underline{S}}$ and stress $\underline{\underline{T}}$. In contrast, the electric field is described by electric displacement $\underline{D}$ and electric field strength $\underline{E}$. $\underline{\underline{\underline{c}}}^E$ is a rank four tensor called the stiffness tensor, measured in [Newton/m^2(Pa)]. It is generally represented as:

$$\underline{\underline{\underline{c}}} = \begin{bmatrix} c_{11} & c_{12} & c_{13} & 0 & 0 & 0 \\ c_{12} & c_{22} & c_{23} & 0 & 0 & 0 \\ c_{13} & c_{23} & c_{33} & 0 & 0 & 0 \\ 0 & 0 & 0 & c_{44} & 0 & 0 \\ 0 & 0 & 0 & 0 & c_{55} & 0 \\ 0 & 0 & 0 & 0 & 0 & c_{66} \end{bmatrix} \tag{2.4}$$

The tensor $\underline{\underline{\varepsilon}}$ is the permittivity along three orthogonal directions, measured in $[Farad/m]$. They are symbolically written as:

$$\underline{\underline{\varepsilon}} = \begin{bmatrix} \varepsilon_{11} & 0 & 0 \\ 0 & \varepsilon_{22} & 0 \\ 0 & 0 & \varepsilon_{33} \end{bmatrix} \tag{2.5}$$

In the absence of piezoelectricity, Eqn.2.2 and 2.3 degrade to elastic and electric constitutive relations:

$$\underline{\underline{T}} = \underline{\underline{\underline{c}}}^E : \underline{\underline{S}} \tag{2.6}$$

$$\underline{D} = \underline{\underline{\varepsilon}}^S \cdot \underline{E} \tag{2.7}$$

2.2.2 Christoffel Equations

Modifying Eqn. 2.6 gives the equation of motion in elastic materials (without piezoelectricity). as [34]:

$$\nabla \cdot \underline{\underline{T}} = \rho \frac{\partial^2 \underline{u}}{\partial t^2} \tag{2.8}$$

where ρ is the mass density and $\underline{u}$ is the displacement. This equation is an analogue to Newton's third law of motion, and it enables the calculation of the second-order time derivative of the displacement (analogous to the acceleration) with the divergence of stress $\underline{\underline{T}}$ (analogous to the external force). This equation can further lead to the Christoffel equation, which is the essential equation in the calculation for vibration modes supported by elastic devices, and it is written as [34]:

$$\nabla \cdot \underline{\underline{\underline{c}}} : \nabla_s \underline{v} = \rho \frac{\partial^2 \underline{v}}{\partial t^2} \tag{2.9}$$

where $\underline{v}$ is the particle velocity, and it is the first-order time-derivative of the displacement. The Christoffel equation has two major limitations: (a) it can only be used in a uniform area, and (b) it doesn't consider the piezoelectricity. For (a), a non-uniform material can be divided into many small uniform areas. To address (b), it is necessary to take the piezoelectric constitutive relations 2.2 and 2.3 into consideration, from which a group of equations can be derived. These equations are known as the coupled Christoffel equations [44].

$$\nabla \cdot \underline{\underline{\underline{c}}}^E : \nabla_s \underline{v} - \rho \frac{\partial^2 \underline{v}}{\partial t^2} = \nabla \cdot \left(\underline{\underline{\underline{e}}}^T \cdot \frac{\partial \underline{E}}{\partial t} \right) \tag{2.10}$$

$$-\nabla \times \nabla \times \underline{E} - \mu_0 \underline{\underline{\epsilon}}^S \cdot \frac{\partial^2 \underline{E}}{\partial t^2} = \mu_0 \underline{\underline{\underline{e}}} : \nabla_s \frac{\partial \underline{v}}{\partial t} \tag{2.11}$$

The left-hand sides of these two equations are the Helmholtz equations, characterizing the vibrational behaviours of the displacement in the acoustic field and the electric field strength in the electric field. The right-hand sides contain the coupling terms that influence these fields, also known as the driving terms.

In these equations, the electric field is divided into two parts, rotational part $E^{(r)}$ and irrotational part $E^{(i)}$. As their name suggested, the rotational part has a non-zero curl, but the irrotational part doesn't, and the irrotational part is represented by the gradient of electric potential Φ, written as $E = \underline{E}^{(r)} - \nabla\Phi$. The reason for doing so is that, according to the Maxwell-Faraday Equation, only the electric field with a non-zero curl can generate the magnetic field, which is of our interest.

Notably, the symmetric gradient operator "$\nabla\cdot$" has the form of the matrix below, and "∇_s" is its transpose.

$$\nabla\cdot = \begin{bmatrix} \frac{\partial}{\partial x} & 0 & 0 & 0 & \frac{\partial}{\partial z} & \frac{\partial}{\partial y} \\ 0 & \frac{\partial}{\partial y} & 0 & \frac{\partial}{\partial z} & 0 & \frac{\partial}{\partial x} \\ 0 & 0 & \frac{\partial}{\partial z} & \frac{\partial}{\partial y} & \frac{\partial}{\partial x} & 0 \end{bmatrix} \tag{2.12}$$

When the wave function of rotational electric fields is obtained, the magnetic field is calculated according to the Maxwell-Faraday equation:

$$\nabla \times \underline{E}^{(r)} = -\frac{\partial \underline{B}}{\partial t} \tag{2.13}$$

The coupled Christoffel equations are then modified and implemented into the FEA software.

2.2.3 Rotation of Coordinates

Most piezoelectric materials exhibit anisotropy, meaning their piezoelectric constants vary when elastic-electromagnetic-acoustic (EMA) waves propagate along different directions relative to the crystallographic axes. This directional dependence complicates simulations when investigating multiple propagations and cutting directions, such as changing from "128° Y-cut" to "X-cut" in $LiNbO_3$. Rather than measuring the piezoelectric constants in every direction, coordinate rotation offers a more efficient approach. This approach can be achieved through the

application of two transformation matrices. They are written as:

$$\underline{A} = \begin{bmatrix} a_{xx} & a_{xy} & a_{xz} \\ a_{yx} & a_{yy} & a_{yz} \\ a_{zx} & a_{zy} & a_{zz} \end{bmatrix} \tag{2.14}$$

$$= \begin{bmatrix} \cos(\beta)\cos(\gamma) & \sin(\alpha)\sin(\beta)\cos(\gamma) - \cos(\alpha)\sin(\gamma) & \cos(\alpha)\sin(\beta)\cos(\gamma) + \sin(\alpha)\sin(\gamma) \\ \cos(\beta)\sin(\gamma) & \sin(\alpha)\sin(\beta)\sin(\gamma) + \cos(\alpha)\cos(\gamma) & \cos(\alpha)\sin(\beta)\sin(\gamma) - \sin(\alpha)\cos(\gamma) \\ -\sin(\beta) & \sin(\alpha)\cos(\beta) & \cos(\alpha)\cos(\beta) \end{bmatrix} \tag{2.15}$$

$$\underline{\underline{M}} = \begin{bmatrix} a_{xx}^2 & a_{xy}^2 & a_{xz}^2 & 2a_{xy}a_{xz} & 2a_{xx}a_{xz} & 2a_{xx}a_{xy} \\ a_{yx}^2 & a_{yy}^2 & a_{yz}^2 & 2a_{yy}a_{yz} & 2a_{yx}a_{yz} & 2a_{yx}a_{yy} \\ a_{zx}^2 & a_{zy}^2 & a_{zz}^2 & 2a_{zy}a_{zz} & 2a_{zx}a_{zz} & 2a_{zx}a_{zy} \\ a_{yx}a_{zx} & a_{yy}a_{zy} & a_{yz}a_{zz} & a_{yy}a_{zz} + a_{yz}a_{zy} & a_{yx}a_{zz} + a_{yz}a_{zx} & a_{yx}a_{zy} + a_{yy}a_{zx} \\ a_{zx}a_{xx} & a_{zy}a_{xy} & a_{zz}a_{xz} & a_{zy}a_{xz} + a_{zz}a_{xy} & a_{zz}a_{xx} + a_{zx}a_{xz} & a_{zx}a_{xy} + a_{xx}a_{zy} \\ a_{xx}a_{yx} & a_{xy}a_{yy} & a_{xz}a_{yz} & a_{xy}a_{yz} + a_{xz}a_{yy} & a_{xz}a_{yx} + a_{xx}a_{yz} & a_{xx}a_{yy} + a_{xy}a_{yx} \end{bmatrix} \tag{2.16}$$

where α, β, and γ are Euler angles about axes x, y, and z, respectively. The first matrix is the rotation matrix for one of the subscripts, whereas the second is the rotation matrix for a pair. With the help of these two transformation matrices, the piezoelectric constants transform according to the following rules:

$$\underline{\underline{c}}' = \underline{\underline{M}} : \underline{\underline{c}} : \underline{\underline{M}}^T \tag{2.17}$$

$$\underline{\underline{e}}' = \underline{A} \cdot \underline{\underline{e}} : \underline{\underline{M}}^T \tag{2.18}$$

$$\underline{\underline{\varepsilon}}' = \underline{A} \cdot \underline{\underline{\varepsilon}} \cdot \underline{A}^T \tag{2.19}$$

The elementwise expression of these equations is inserted into COMSOL as variables. The code is detailed in Section 2.4.3.

2.2.4 Solutions to the Christoffel Equations

The coupled Christoffel equations have a certain amount of solutions for each propagation direction. This direction is represented using a direction vector:

$$\vec{l} = l_x\hat{x} + l_y\hat{y} + l_z\hat{z} \tag{2.20}$$

where l_x, l_y, and l_z are the normalized components of the phase velocity in the x-, y-, and z-directions respectively and $l_x^2 + l_y^2 + l_z^2 = 1$. By using this direction vector, the differential operators in the coupled differential equations can be directly substituted as:

$$\nabla \rightarrow \begin{bmatrix} l_x \\ l_y \\ l_z \end{bmatrix}$$

$$\nabla\cdot \rightarrow \begin{bmatrix} l_x & 0 & 0 & 0 & l_z & l_y \\ 0 & l_y & 0 & l_z & 0 & l_x \\ 0 & 0 & l_z & l_y & l_x & 0 \end{bmatrix}$$

Certain values are assigned to l_x, l_y, and l_z for certain directions. For example, for wave propagating along the x direction, $[l_x, l_y, l_z] = [1, 0, 0]$. For waves propagating along a random direction in the XY-plane, $[l_x, l_y, l_z] = [\cos(\theta), \sin(\theta), 0]$, where θ is the angle between the propagating direction and the X-axis.

In most cases, the coupled Christoffel equations have 5 solutions, coming out of the following four categories: purely acoustic wave, purely electromagnetic wave, quasi-acoustic wave, and

quasi-electromagnetic wave. When the piezoelectricity disappears, the quasi-acoustic wave reduces to a purely acoustic wave and its velocity decreases, whereas the quasi-electromagnetic wave reduces to a purely electromagnetic wave and its velocity increases.

2.2.5 Quasi-static approximation

The rotational field usually contributes little to piezoelectric coupling but brings computational complexity. Therefore, people typically use the quasi-static approximation (QSA) to neglect the rotational field. With this approximation, the total electric field has zero curl and can be represented entirely as the gradient of the electric potential gradient. The Christoffel is reduced to a set of two equations:

$$\nabla \cdot \underline{\underline{\underline{c}}}^{E} : \nabla_s \underline{v} - \rho \frac{\partial^2 \underline{v}}{\partial t^2} = -\nabla \cdot \left(\underline{\underline{\underline{e}}} \cdot \frac{\partial \nabla \Phi}{\partial t} \right) \tag{2.21}$$

$$0 = -\mu_0 \nabla \cdot \left(\underline{\underline{\underline{\varepsilon}}}^{s} \cdot \frac{\partial^2 \nabla \Phi}{\partial t^2} \right) + \mu_0 \nabla \cdot \left(\underline{\underline{\underline{e}}} : \nabla_s \frac{\partial \underline{v}}{\partial t} \right) \tag{2.22}$$

The quasi-static approximation significantly simplifies the calculation with minor electric and acoustic field inaccuracies. However, this approach does not permit the magnetic field calculation and must be avoided in this chapter. To achieve that, the electric field strength should be represented using its three components $\{E_x, E_y, E_z\}$ in orthogonal directions, and use the complete coupled Christoffel equation, *i.e.* Equation 2.10 & 2.11.

2.2.6 Weak Forms

Both weak forms and differential equations effectively solve field problems in Physics. A primary difference between them is how conditions are satisfied: differential equations require the conditions to be satisfied pointwise, while weak forms only need conditions to be satisfied on average over a region. Thus, the constraint in weak forms is relatively weaker, which explains why they are termed weak. When compared, weak forms have several advantages over differential equations:

- **Easier computation**. Reducing the order of the differential equations in the derivation of weak forms makes the mathematical handling of the equations easier.
- **Less requirements on continuity**. Weak forms, naturally being mainly integral rather than differential, demand less continuity in the variables. This property is particularly beneficial in real-world scenarios where materials and geometries may exhibit discontinuities, such as cracks or joints, which weak forms can handle properly.
- **More Flexibility in boundary conditions**. Weak forms employ Lagrange multipliers to apply boundary conditions. This approach allows precise control over boundary behaviour, even when the boundary condition is complex.

These advantages make the weak forms particularly suitable for FEM simulations.

2.2.7 Derivation of Weak Forms

A transformation from differential equations to weak forms is often necessary. The transformation is typically as follows:

1 **Multiplication by a test function**. The original differential equation is multiplied by a test function, where the dependent variable is usually chosen and denoted with a tilde "˜". For example, the test function of displacement $\tilde{u}$ is usually used in acoustic fields.

2 **Integration over the domain**. The product of a differential equation and the corresponding test function are then integrated over the problem's domain.

3 **Intergration by parts**. This step reduces the order of differential equations and simplifies the following calculation.

The standard format after the derivation should be like:

$$-\int f(q)\ dq = 0 \tag{2.23}$$

where q is a generalized dependent variable and $f(q)$ is a function including q and its low-order derivatives.

This general derivation of weak forms can be a complex process that easily leads to mistakes. To simplify this process, a more straightforward empirical method is used and presented below. This method has not been strictly proven but is often valid based on our experience. Our analysis of the coupled EMA field in piezoelectric materials will be elucidated here as an example.

- **Determine the total energy of the field.** In this case, four kinds of energy are considered: kinetic energy, elastic energy, electric energy, and magnetic energy. Following the same order, the total energy U is written as:

$$2U = \underline{v} \cdot \underline{p} + \underline{\underline{S}} : \underline{\underline{T}} + \underline{E} \cdot \underline{D} + \underline{H} \cdot \underline{B}$$

  where 8 variables are used: velocity $\underline{v}$, momentum density $\underline{p}$, strain $\underline{\underline{S}}$, stress $\underline{\underline{T}}$, electric field strength $\underline{E}$, electric displacement $\underline{D}$, magnetic field strength $\underline{H}$ and magnetic flux density $\underline{B}$.

- **Replace with test functions**. Choose to replace one variable most similar to a dependent variable in each term. Given that the dependent variables in acoustic field and electromagnetic fields are displacement $\underline{u}$ and electric field strength $\underline{E}$, this leads to:

$$\tilde{\underline{v}} \cdot \underline{p} + \tilde{\underline{\underline{S}}} : \underline{\underline{T}} + \tilde{\underline{E}} \cdot \underline{D} + \tilde{\underline{H}} \cdot \underline{B}$$

  For instance, velocity is explicitly expressed as $\underline{v} = \frac{\partial \underline{u}}{\partial t}$, which is more similar to displacement $\underline{u}$ than momentum density $\underline{p} = \rho \frac{\partial \underline{u}}{\partial t}$, and then velocity is replaced.

- **Integrate and add a minus sign**. The final form of this derivation is:

$$-\int_V \left(\tilde{\underline{v}} \cdot \underline{p} + \tilde{\underline{\underline{S}}} : \underline{\underline{T}} + \tilde{\underline{E}} \cdot \underline{D} + \tilde{\underline{H}} \cdot \underline{B} \right) dV = 0 \tag{2.24}$$

Equations 2.2, 2.3, and 2.13 allow Equation 2.24 to be expressed using only three variables: the angular frequency ω, the displacement field $\underline{u}$, and the electric field strength $\underline{E}$. This form is implemented in the finite element method (FEM) software, as described in Section 2.4.5, where ω is then computed as the eigenfrequency.

2.2.8 Penalty Terms

Like Reference [45], a penalty term is used to regulate the electromagnetic field. This penalty term is modified from Gauss's Law. Since the charge density in the device is zero, the penalty term is written as

$$\nabla \cdot \underline{D} = 0 \tag{2.25}$$

2.2.9 Boundary Conditions

In COMSOL, each boundary requires a condition (or several consistent conditions) applied to it. An optimal choice of boundary condition can, furthermore, increase accuracy and reduce calculation time.

This section introduces all the choices explored thus far in the method, based on the various "nodes" available in COMSOL's *weak form PDE* interface.

Fixed Boundary Condition

The fixed boundary condition is a simple choice on boundaries that a kind of wave cannot (or barely) reach.

This boundary condition is realised using *Dirichlet Boundary Condition* node, with all three input boxes filled by zeros.

Periodic Boundary Condition

In the analysis of models such as an infinitely large substrate, the use of periodic boundary conditions becomes essential. These conditions limit the propagating region to an integer multiple of the wavelength, ensuring efficiency in computing resources. To achieve this, periodic boundary conditions should be applied specifically along the boundaries that are perpendicular to the direction of propagation. Furthermore, when the objective is to constrain the simulation to waves that remain uniform across a transverse direction, this uniformity can be achieved by implementing periodic boundary conditions along a thin region (smaller than the propagation wavelength) in the transverse direction of interest.

Periodic Condition node is provided by *weak form PDE* interface.

Free Boundary Condition and Continuity Boundary Condition

On the interface between a piezoelectric material and the environment, the propagation of an acoustic wave stops, but the propagation of an electromagnetic wave does not. Thus, the free boundary condition should be applied here for acoustic waves and the continuous boundary condition for the electromagnetic field.

The continuous boundary condition comes from Electrodynamics. For electromagnetic fields on both sides, the tangential part of $\underline{E}$ and the normal part (relative to an interface) of $\underline{D}$ are the same.

$$(\underline{E}_1 - \underline{E}_2)\times\hat{n} = 0 \tag{2.26a}$$

$$(\underline{D}_1 - \underline{D}_2)\cdot\hat{n} = 0 \tag{2.26b}$$

The free boundary condition can be realised using the default *Zero Flux* node. The continuity boundary condition can be realised using the *Pointwise Constraint* node, and its configuration

can be found in Sec.2.4.5.

Electric-Wall Boundary Condition

In certain models, the piezoelectric device is placed within a cavity surrounded by highly conductive walls. These walls reflect electromagnetic waves, minimizing energy loss by reducing the radiation that would otherwise escape. The electric-wall boundary condition can accurately represent such metal walls while avoiding introducing a specific material and analysing an additional domain. This condition constrains the tangential part of the electric field strength to be zero.

$$\underline{E} \times \hat{n} = 0 \tag{2.27}$$

The electric-wall boundary condition is applied using three *Pointwise Constraint* nodes.

Absorbing Boundary Condition

The Absorbing boundary condition (ABC) is applied to truncate the calculation domain to a reasonable size. Without the ABC, the radiating electromagnetic wave will reflect off the truncating surfaces and disturb (interfere with) wave patterns in other domains. The ABC is in the form of a constraint and does not need the introduction of an extra cladding domain. The explicit form of the first-order ABC is [46]:

$$\hat{r} \times \nabla \times \underline{E} = jk\underline{E}_t - (s-1)\nabla_t E_r \tag{2.28}$$

where $\hat{r}$ is the spherical radius, j is the imaginary unit, k is the wavenumber, and s is a factor. It was reported in Reference [46] that $s = 0.5$ gives the minimum reflection.

In COMSOL, (2.28) is separated into three components and put into three *Pointwise Constraint*

nodes. Its configuration is detailed in Sec.2.4.5.

2.2.10 M-field Method

As mentioned, the components of electric field strength $\{E_x, E_y, E_z\}$ are usually chosen as the dependent variables for the electromagnetic field. The subsequent derivation of the magnetic field strength, however, requires division by the angular frequency ω (of the simulated mode), which is *a priori* unknown. This paradoxical situation can be circumvented by using derived variables $\{M_x, M_y, M_z\}$ as the dependent variables. These variables are defined as

$$M_x = \frac{E_x}{\omega},\ M_y = \frac{E_y}{\omega},\ M_z = \frac{E_z}{\omega} \tag{2.29}$$

2.2.11 Magnetic Coupling Coefficient

The performance of a piezoelectric structure as a magnetic-field generator can be quantified by its magnetic coupling coefficient η, defined as

$$\eta = \frac{E_{\text{mag}}^{\text{ext}}}{E_{\text{kin}}^{\text{int}} + E_{\text{ela}}^{\text{int}} + E_{\text{elec}}^{\text{int}} + E_{\text{mag}}^{\text{int}} + E_{\text{elec}}^{\text{ext}} + E_{\text{mag}}^{\text{ext}}} \tag{2.30}$$

where E_{kin}, E_{ela}, E_{elec} and E_{mag} denote kinetic energy, elastic energy, electric energy and magnetic energy, respectively. The superscripts "int" and "ext" denote the internal field (within the piezoelectric substrate) and external field (in the surrounding environment). Each energy is calculated using an integration of corresponding energy density throughout its area.

The coupling coefficient represents the amount of energy that must be injected into the system to generate a unit of magnetic energy. A lower coefficient implies that more energy needs to be injected. A magnetic coupling coefficient higher than 10^{-2} is desirable for practical applications and energy efficiency.

2.3 Historical Methods

Various attempts were made to simulate the full electromagnetic field generated by piezoelectric devices, but they all lack generality: they are only solvable with certain materials on certain geometries. Two methods are introduced here since they were used to calculate the reference velocities in Table 2.14.

2.3.1 Superposition of Partial Waves

The Superposition of Partial Waves (SPW) method can provide analytical wave functions of SAWs at the planar boundaries of infinitely large waveguides or substrates. This approach is grounded in the principle that a field within a structure can be expressed as a superposition of all the modes that the structure supports [34]. These modes are referred to as partial waves, representing waves propagating in specific directions within an infinitely large piezoelectric space. They are solutions to the coupled Christoffel equations (Eqn. 2.10 and 2.11). The SPW method also requires high symmetry in materials, like the uni-axial symmetry in PZT-5H.

The SPW method is a classical and fundamental approach for analyzing acoustic waves at planar boundaries. However, it has several limitations. Specifically, it requires (a) the boundary to be planar and infinitely large, and (b) the piezoelectric material possesses symmetry that exists on the sagittal plane (the plane characterised by the propagating direction and the norm of the boundary). These constraints restrict the applicability of the SPW method, making it unsuitable for complex boundary geometries or materials without the specified symmetry characteristics.

The idea of this method is applied for the analytical calculation of partial waves in Sec.2.5.1.

2.3.2 Transverse Resonance Method

The transverse resonance method (abbreviated to TRM) is another method. When using this method, the wave functions are defined based on the unique properties of particular waves. For

example, Rayleigh waves oscillate sinusoidally along the axis of a waveguide or a resonator and decay exponentially along the depth. Therefore, the general wave function of a Rayleigh wave is defined as

$$A\exp\left(\underline{\Omega}\cdot\underline{x_2}\right)\exp\left[i(\underline{k}\cdot\underline{x_1}-\omega t)\right] \tag{2.31}$$

where $\underline{x_1}$ and $\underline{x_2}$ are two vectors along the axis and depth, respectively. $\underline{\Omega}$ is a decay constant, and $\underline{k}$ is the wave vector.

Compared to the SPW method, the TRM method is relatively more versatile, as it can, in principle, be applied to substrates made of anisotropic piezoelectric materials. However, full anisotropy significantly increases the complexity of solving an intermediate equation, making it nearly impractical. As a result, uniaxial materials are still preferred. But this symmetry doesn't need to exist on the sagittal plane. Besides, the TRM method also requires the boundaries to be planar and infinitely large (unless the wave patterns on a curved boundary are already known). Additionally, it also involves numerically finding solutions of an equation using the bisection method, which typically takes about 10 minutes to achieve a relative error of 10^{-10}.

Notably, this method doesn't involve any approximation, and accuracy is only impacted by the bisection method. This method is applied for finding reference velocity in Table 2.14.

2.4 How to Build a Model

This section presents detailed instructions for applying our method. Although this approach is applicable to any FEM software that supports a weak-form solver, COMSOL Multiphysics (hereafter referred to as COMSOL) is used as an example. In this section, `Monospaced font` denotes the inputs or the code, and *Italic font* denotes terminology used in COMSOL. Supporting information can be found in this GitHub repository.

2.4.1 Selecting Physics

Initially, an empty model needs to be created. Upon launching the software, click on *Model Wizard* to begin. Our method uses *3D* spatial dimension as well as three instances of *Weak Form PDE* Physics—(w), (w2), and (w3)—located under *Mathematics, PDE Interfaces*. Their units will be modified later. The names of the *Dependent Variables* are modified according to the following table:

Field #1:	`u`	`v`	`w`
Field #2:	`M1x`	`M1y`	`M1z`
Field #3:	`M2x`	`M2y`	`M2z`

Afterwards, the *Eigenfrequency* study is selected, and *Done* is clicked to proceed. Then, the main panel of COMSOL will appear automatically. Users can now rename the three *Physics* to "Acoustic Field(w1)", "Internal EM Field(w2)" and "External EM Field(w3)".

2.4.2 Defining global parameters and variables.

Both global parameters and variables are symbols accessible across all models within a COMSOL file, but they are different. Parameters are user-defined constants that remain unchanged during simulation, whereas variables are expressions dependent on other variables and the model's dependent variables.

The global parameters and variables are defined within the *Global Definitions* node. As detailed in the following sections, values can be inserted either by importing from `.txt` files (found in the GitHub repository) or inputting manually. Parameters or variables from the same table should be placed in the same node.

Certain global variables may depend on local variables, such as local independent variables of a model or maximum operator `maxop`. In such cases, a prefix helps access local variables within certain models. For example, prefix `comp1.` corresponds to variables in model number 1.

Global Parameters

Table 2.2 shows the list of parameters. The first parameter here is the rotation angle of material coordinates (see Auld's book [34], page 60). The second one is a unit transformation. Note that there is a "0" in the brackets. It is used to adjust the initial orientation. For example, when "0" is replaced by "90" for a rotation about the x-axis, the orientation of the substrate changes from Z-cut to Y-cut. The third and fourth parameters give the estimated angular frequency the *Absorbing Boundary Condition* requires. This frequency needs to be inputted manually (initial guess), calculated and corrected until stable (*i.e.* self-consistent).

name	expression
degree	0
q	(degree-0)/180*pi[rad]
freq_t	20.38E3
omega_t	freq_t*2*pi[rad/s]

Table 2.2: Global parameters. In this table, `q` is a converter for global rotation from degrees into radians, `degree` is the angle of global rotation, `freq_t` is the estimated frequency in absorbing boundary condition, and `omega_t` is a converter for estimated frequency from Hz into rad/s.

Global Variables - Maximum

The global variables in Table 2.3 are used to find global maximum values. These values help normalise each field and avoid discontinuity of plots on boundaries. More details will be given in Section 2.4.6.

Global Variables - Acoustic Field

The global variables in Table 2.4 are used to support weak forms in an acoustic field. The dependant variables in the acoustic field are $\{\mathtt{u}, \mathtt{v}, \mathtt{w}\}$. They represent displacements along the directions of the $x-$, $y-$ and $z-$ axis, respectively. Expressions like "`ab`" denote the partial derivative of variable `a` to variable `b`. For example, `ux` is the partial derivative of distance `u` in the $x-$ direction. `cE` and `eES` are components of the stiffness tensor and the piezoelectric coupling tensor at zero or constant electric field strength, respectively.

name	expression
mE	max(comp1.maxop1(sqrt(realdot(E1x,E1x)+realdot(E1y,E1y) +realdot(E1z,E1z))),comp1.maxop2(sqrt(realdot(E2x,E2x) +realdot(E2y,E2y)+realdot(E2z,E2z))))
mEx	max(comp1.maxop1(real(E1x)),comp1.maxop2(real(E2x)))
mEy	max(comp1.maxop1(real(E1y)),comp1.maxop2(real(E2y)))
mEz	max(comp1.maxop1(real(E1z)),comp1.maxop2(real(E2z)))
mDx	max(comp1.maxop1(real(D1x)),comp1.maxop2(real(D2x)))
mDy	max(comp1.maxop1(real(D1y)),comp1.maxop2(real(D2y)))
mDz	max(comp1.maxop1(real(D1z)),comp1.maxop2(real(D2z)))
mH	max(comp1.maxop1(sqrt(realdot(H1x,H1x)+realdot(H1y,H1y) +realdot(H1z,H1z))),comp1.maxop2(sqrt(realdot(H2x,H2x) +realdot(H2y,H2y)+realdot(H2z,H2z))))
mHx	max(comp1.maxop1(real(H1x)),comp1.maxop2(real(H2x)))
mHy	max(comp1.maxop1(real(H1y)),comp1.maxop2(real(H2y)))
mHz	max(comp1.maxop1(real(H1z)),comp1.maxop2(real(H2z)))

Table 2.3: Global variables for finding the global maximum values. In this table, `m` denotes the maximum, `E`, `D`, and `H` are the electric field strength, electric displacement field and magnetic field strength, respectively.

name	expression	description
omega	2*pi*lambda [rad/s]	angular frequency
S1	comp1.ux	strain
S2	comp1.vy	strain
S3	comp1.wz	strain
S4	comp1.wz	strain
S5	comp1.uz+comp1.wx	strain
S6	comp1.uy+comp1.vx	strain
T1	cE11*S1+cE12*S2+cE13*S3+cE14*S4+cE15*S5+cE16*S6	stress
T2	cE21*S1+cE22*S2+cE23*S3+cE24*S4+cE25*S5+cE26*S6	stress
T3	cE31*S1+cE32*S2+cE33*S3+cE34*S4+cE35*S5+cE36*S6	stress
T4	cE41*S1+cE42*S2+cE43*S3+cE44*S4+cE45*S5+cE46*S6	stress
T5	cE51*S1+cE52*S2+cE53*S3+cE54*S4+cE55*S5+cE56*S6	stress
T6	cE61*S1+cE62*S2+cE63*S3+cE64*S4+cE65*S5+cE66*S6	stress
eSx	eES11*S1+eES12*S2+eES13*S3+eES14*S4+eES15*S5+eES16*S6	$\underline{\underline{e}} : \underline{\underline{S}}$
eSy	eES21*S1+eES22*S2+eES23*S3+eES24*S4+eES25*S5+eES26*S6	$\underline{\underline{e}} : \underline{\underline{S}}$
eSz	eES31*S1+eES32*S2+eES33*S3+eES34*S4+eES35*S5+eES36*S6	$\underline{\underline{e}} : \underline{\underline{S}}$

Table 2.4: Global variables used in an acoustic field.

Global Variables - Internal & External Electromagnetic Fields

Two lists of the variables used in internal and external fields are shown in Table 2.5 and 2.6, respectively. The dependant variables in two electromagnetic fields are {`M1x`, `M1y`, `M1z`} and {`M2x`, `M2y`, `M2z`}. The symbol `epsilon` is the vacuum permittivity, and `eE` is an intermediate quantity of the coupling energy.

If the external field is unnecessary, only the first table should be inputted into COMSOL and

all index "1' 's need to be discarded.

name	expression	description
E1x	comp1.M1x*omega	electric field strength
E1y	comp1.M1y*omega	electric field strength
E1y	comp1.M1y*omega	electric field strength
curlM1x	comp1.M1zy-comp1.M1yz	curl of the M-field
curlM1y	comp1.M1xz-comp1.M1zx	curl of the M-field
curlM1z	comp1.M1yx-comp1.M1xy	curl of the M-field
H1x	curlM1x/(-i*mu0_const)	magnetic field strength
H1y	curlM1y/(-i*mu0_const)	magnetic field strength
H1z	curlM1z/(-i*mu0_const)	magnetic field strength
eE1	eES11*E1x+eES21*E1y+eES31*E1z	$\underline{\underline{e}}^T \cdot \underline{E}$
eE2	eES12*E1x+eES22*E1y+eES32*E1z	$\underline{\underline{e}}^T \cdot \underline{E}$
eE3	eES13*E1x+eES23*E1y+eES33*E1z	$\underline{\underline{e}}^T \cdot \underline{E}$
eE4	eES14*E1x+eES24*E1y+eES34*E1z	$\underline{\underline{e}}^T \cdot \underline{E}$
eE5	eES15*E1x+eES25*E1y+eES35*E1z	$\underline{\underline{e}}^T \cdot \underline{E}$
eE6	eES16*E1x+eES26*E1y+eES36*E1z	$\underline{\underline{e}}^T \cdot \underline{E}$
D1x	epsilon_xx*E1x+epsilon_xy*E1y+epsilon_xz*E1z+eSx	electric displacement
D1y	epsilon_yx*E1x+epsilon_yy*E1y+epsilon_yz*E1z+eSy	electric displacement
D1z	epsilon_zx*E1x+epsilon_zy*E1y+epsilon_zz*E1z+eSz	electric displacement
D1n	D1x*comp1.w3.nx+D1y*comp1.w3.ny+D1z*comp1.w3.nz	electric displacement
tM1x	comp1.M1x-(comp1.w2.nx*comp1.M1x+comp1.w2.ny* comp1.M1y+comp1.w2.nz*comp1.M1z)*comp1.w2.nx	tangential M-field
tM1y	comp1.M1y-(comp1.w2.nx*comp1.M1x+comp1.w2.ny* comp1.M1y+comp1.w2.nz*comp1.M1z)*comp1.w2.ny	tangential M-field
tM1z	comp1.M1z-(comp1.w2.nx*comp1.M1x+comp1.w2.ny* comp1.M1y+comp1.w2.nz*comp1.M1z)*comp1.w2.nz	tangential M-field

Table 2.5: Global variables used in an internal electromagnetic field.

name	expression	description
E2x	comp1.M2x*omega	electric field strength
E2y	comp1.M2y*omega	electric field strength
E2y	comp1.M2y*omega	electric field strength
curlM2x	comp1.M2zy-comp1.M2yz	curl of the M-field
curlM2y	comp1.M2xz-comp1.M2zx	curl of the M-field
curlM2z	comp1.M2yx-comp1.M2xy	curl of the M-field
H2x	curlM2x/(-i*mu0_const)	magnetic field strength
H2y	curlM2y/(-i*mu0_const)	magnetic field strength
H2z	curlM2z/(-i*mu0_const)	magnetic field strength
D2x	epsilon_xx*E2x+epsilon_xy*E2y+epsilon_xz*E2z	electric displacement field
D2y	epsilon_yx*E2x+epsilon_yy*E2y+epsilon_yz*E2z	electric displacement field
D2z	epsilon_zx*E2x+epsilon_zy*E2y+epsilon_zz*E2z	electric displacement field
D2n	D2x*comp1.w3.nx+D2y*comp1.w3.ny+D2z*comp1.w3.nz	electric displacement field
tM2x	comp1.M2x-(comp1.w2.nx*comp1.M2x+comp1.w2.ny* comp1.M2y+comp1.w2.nz*comp1.M2z)*comp1.w2.nx	tangential M-field
tM2y	comp1.M2y-(comp1.w2.nx*comp1.M2x+comp1.w2.ny* comp1.M2y+comp1.w2.nz*comp1.M2z)*comp1.w2.ny	tangential M-field
tM2z	comp1.M2z-(comp1.w2.nx*comp1.M2x+comp1.w2.ny* comp1.M2y+comp1.w2.nz*comp1.M2z)*comp1.w2.nz	tangential M-field

Table 2.6: Global variables used in an external electromagnetic field.

Global Variables - Absorbing Boundary Condition

These variables are required when the absorbing boundary condition (ABC) is used (shown in Table 2.7). The "sphere" refers to the surface that truncates the calculating domain, which is also the surface of the external electromagnetic field. `k` is an estimated wave number. Its value is determined by `omega_t`, which is defined in Table 2.2. `c_const` is the velocity of light in a vacuum. In principle, the ABC is only applied in the external field. That is why {`M2x`, `M2y`, `M2z`} is used here.

name	expression	
k	omega_t/c_const	estimated wave number
rx	x/sqrt(x^2+y^2+z^2)	normal on the sphere
ry	y/sqrt(x^2+y^2+z^2)	normal on the sphere
rz	z/sqrt(x^2+y^2+z^2)	normal on the sphere
rcurlMx	ry*curlM2z-rz*curlM2y	$\underline{r} \times \nabla \cdot \underline{M}$
rcurlMy	rz*curlM2x-rx*curlM2z	$\underline{r} \times \nabla \cdot \underline{M}$
rcurlMz	rx*curlM2y-ry*curlM2x	$\underline{r} \times \nabla \cdot \underline{M}$
Mtx	comp1.M2x-(comp1.M2x*rx+comp1.M2y*ry+comp1.M2z*rz)*rx	projection of M on the norm
Mty	comp1.M2y-(comp1.M2x*rx+comp1.M2y*ry+comp1.M2z*rz)*ry	projection of M on the norm
Mtz	comp1.M2z-(comp1.M2x*rx+comp1.M2y*ry+comp1.M2z*rz)*rz	projection of M on the norm

Table 2.7: Global variables required in the application of Absorbing Boundary Conditions.

2.4.3 Rotating material coordinates

In COMSOL, material coordinates are predetermined and static. For waves propagating along various directions relative to the materials, users have two main approaches to handling them. The first approach is to construct the models facing different directions. A more straightforward approach involves rotating the material coordinates by implementing a set of variables representing the rotated stiffness tensor, piezoelectric coupling tensor, and permittivity matrix. They are calculated following the rotating relations shown in Equation 2.17, 2.18, and 2.19. The corresponding tables are truncated and put in Table 2.8, 2.9 and 2.10.

It is important to clarify that such rotation only works with one of the three axes. Users can specify this axis by activating the corresponding node in the software and deactivating the others.

Name	Expression
c11	root.material.StressCharge.cE11
c12	root.material.StressCharge.cE12
c13	root.material.StressCharge.cE13
c14	root.material.StressCharge.cE14
c15	root.material.StressCharge.cE15
c16	root.material.StressCharge.cE16
c21	root.material.StressCharge.cE21
c22	root.material.StressCharge.cE22
c23	root.material.StressCharge.cE23
c24	root.material.StressCharge.cE24
c25	root.material.StressCharge.cE25
c26	root.material.StressCharge.cE26
c31	root.material.StressCharge.cE31
c32	root.material.StressCharge.cE32
c33	root.material.StressCharge.cE33
c34	root.material.StressCharge.cE34
c35	root.material.StressCharge.cE35
c36	root.material.StressCharge.cE36
c41	root.material.StressCharge.cE41
c42	root.material.StressCharge.cE42
c43	root.material.StressCharge.cE43
c44	root.material.StressCharge.cE44
c45	root.material.StressCharge.cE45
c46	root.material.StressCharge.cE46
c51	root.material.StressCharge.cE51
c52	root.material.StressCharge.cE52
c53	root.material.StressCharge.cE53
c54	root.material.StressCharge.cE54
c55	root.material.StressCharge.cE55
c56	root.material.StressCharge.cE56
c61	root.material.StressCharge.cE61
c62	root.material.StressCharge.cE62
c63	root.material.StressCharge.cE63
c64	root.material.StressCharge.cE64
c65	root.material.StressCharge.cE65
c66	root.material.StressCharge.cE66

Table 2.8: Global parameters representing the reduced form of the stiffness tensor.

2.4.4 Building models

Geometric models can be built by selecting primitives such as *Block* or *Cylinder* from the context menu of *Geometry 1*. The dimensions—*Width*, *Depth*, and *Height*—are then manually entered in the settings for each primitive. Additionally, the unit of measurement can be adjusted in the settings of *Geometry 1*.

Booleans operations (*Union*, *Intersection* and *Difference*) are especially usefully for complex structures. These operations can be found under *Booleans and Partitions* in the context menu of *Geometry 1*.

Name	Expression
e11	root.material.StressCharge.eES11
e12	root.material.StressCharge.eES12
e13	root.material.StressCharge.eES13
e14	root.material.StressCharge.eES14
e15	root.material.StressCharge.eES15
e16	root.material.StressCharge.eES16
e21	root.material.StressCharge.eES21
e22	root.material.StressCharge.eES22
e23	root.material.StressCharge.eES23
e24	root.material.StressCharge.eES24
e25	root.material.StressCharge.eES25
e26	root.material.StressCharge.eES26
e31	root.material.StressCharge.eES31
e32	root.material.StressCharge.eES32
e33	root.material.StressCharge.eES33
e34	root.material.StressCharge.eES34
e35	root.material.StressCharge.eES35
e36	root.material.StressCharge.eES36

Table 2.9: Global parameters representing the reduced form of the coupling tensor.

Name	Expression
epsilon11	root.material.def.epsilonr11 * epsilon0_const
epsilon12	root.material.def.epsilonr12 * epsilon0_const
epsilon13	root.material.def.epsilonr13 * epsilon0_const
epsilon21	root.material.def.epsilonr21 * epsilon0_const
epsilon22	root.material.def.epsilonr22 * epsilon0_const
epsilon23	root.material.def.epsilonr23 * epsilon0_const
epsilon31	root.material.def.epsilonr31 * epsilon0_const
epsilon32	root.material.def.epsilonr32 * epsilon0_const
epsilon33	root.material.def.epsilonr33 * epsilon0_const

Table 2.10: Global parameters representing the reduced form of the permittivity matrix.

2.4.5 Configuring Weak Forms

The following code blocks are placed into three fields to configure weak forms. For each field, the user should navigate to the corresponding *Physics* section, access the context menu with a right-click, and choose *Weak Contribution* to add a new node. It is recommended that lines of code with different indexes be placed into separate input boxes within the same node.

Once the code is entered, the user must manually specify the domains where these weak forms work. This is done in the settings panel of each node. It is important to note that coupling

terms of the electromagnetic field exclusively exist within the piezoelectric material, referred to as the internal EM field.

In the Acoustic Field(w1):

```
-(test(S1)*T1+test(S2)*T2+test(S3)*T3+test(S4)*T4+test(S5)*T5+test(S6)*T6)
rho*(omega)^2*(test(u)*u+test(v)*v+test(w)*w)
(test(S1)*eE1+test(S2)*eE2+test(S3)*eE3+test(S4)*eE4+test(S5)*eE5+test(S6)*eE6)
```

In the Internal EM field(w2):

```
-(D1x*test(E1x)+D1y*test(E1y)+D1z*test(E1z))
(curlM1x*test(curlM1x)+curlM1y*test(curlM1y)+curlM1z*test(curlM1z)) / mu0_const
```

In the External EM field(w3):

```
-(D2x*test(E2x)+D2y*test(E2y)+D1z*test(E2z))
(curlM2x*test(curlM2x)+curlM2y*test(curlM2y)+curlM2z*test(curlM2z)) / mu0_const
```

The penalty terms:

```
d(D1x,x)+d(D1y,y)+d(D1z,z)
```

Weak forms of boundary conditions are also listed here. Their theory is detailed in Sec.2.2.9.

Continuity boundary condition is applied to the internal and external electromagnetic field interfaces. It is input into three *Pointwise Constraint* nodes in each field.

```
tM1x-tM2x
tM1y-tM2y
tM1z-tM2z
D1n - D2n
```

The ABC is divided into three components, which are input into three separate *Weak Constraint* nodes.

```
rcurlMx - i*k*Mtx
rcurlMy - i*k*Mty
rcurlMz - i*k*Mtz
```

2.4.6 Analysing Methods

Visualisation

Since the electromagnetic fields in different materials are simulated individually in different physics nodes, multiple colour bars will automatically appear with different ranges. This can cause fields to appear discontinuous when, in fact, they are not. This can be straightforwardly solved by rescaling in post-processing ("*Results Analysis*"): the global maximum values of the electric field strength and the magnetic field strength, `mE` and `mH`, are found using *Maximum Operator*s. Each electric or magnetic field strength is then divided by `mE` or `mH`, respectively. The range of the colour bar is then set manually as $[0, 1]$. A similar method can be applied to the three components of electric field strength, electric displacement and magnetic field strength.

For a better inspection of the electromagnetic field inside objects, *Multislide* is used for visualisation of field strength and *Arrow Volume* is used for visualisation of the field line. *Volume* and *Deformation* are used to visualize the acoustic field's displacement.

Calculating Velocities

In the study of *Eigenfrequency* analysis using COMSOL, the primary output is the vibration frequencies in Hertz. These frequencies are model-dependent, meaning they vary with the model's size, making direct comparisons with other experimental results challenging. On the opposite, the propagating phase velocity is the property of the materials and doesn't depend on models. In waveguide simulations, the wave propagation velocities can be derived from the obtained frequencies using the following equation:

$$v = df \tag{2.32}$$

Where v represents the wave propagation velocity along the waveguide, d is the length of the

waveguide in the direction of propagation, and f is the calculated frequency.

Calculating Magnetic Coupling Coefficient

The magnetic coupling coefficient was defined in Equation 2.30. The total energy of a particular type (electric, magnetic, elastic and kinetic) within a particular domain can be evaluated using the two *Volume Integration* nodes (can be found under *Derived Values*), where the relevant energy densities (for different domains) are defined. One node selects the domain (or domains) containing the piezoelectric material whose corresponding energy densities are shown in Table 2.11.

Expression	Unit	Description
realdot(S1,T1)+realdot(S2,T2)+realdot(S3,T3) +realdot(S4,T4)+realdot(S5,T5)+realdot(S6,T6)	J	E_ela_int
rho*omega^2*(realdot(u,u)+realdot(v,v)+realdot(w,w))	J	E_kin_int
realdot(D1xE,E1x)+realdot(D1yE,E1y)+realdot(D1zE,E1z)	J	E_elec_int
mu0_const*(realdot(H1x,H1x)+realdot(H1y,H1y)+realdot(H1z,H1z))	J	E_mag_int

Table 2.11: Energy densities in the internal fields.

The other node selects the domain (or domains) of space surrounding the piezoelectric material, whose energy densities are shown in Table 2.12.

Expression	Unit	Description
(realdot(D2x,E2x)+realdot(D2y,E2y)+realdot(D2z,E2z))	J	E_elec_ext
mu0_const*(realdot(H2x,H2x)+realdot(H2y,H2y)+realdot(H2z,H2z))	J	E_mag_ext

Table 2.12: Energy densities in the external fields.

The value of each global integration will be printed in the *Table* window. The Equation 2.30 is needed before getting the final coupling coefficient. This division cannot be directly calculated in COMSOL, so please use other software.

2.5 Results

Test cases are illustrated below to verify the accuracy and capability of our method.

2.5.1 Partial waves

Partial waves are the most essential modes in a piezoelectric material, as they form the basis from which all other wave modes can be derived through superposition. This example is provided to show that the reported method gives high accuracy for these most fundamental modes, while the built-in *Solid Mechanics* and *AC/DC* modules in COMSOL do not, even though previous studies have reported their effectiveness. In this case, both COMSOL modules fail to simulate some partial waves, which suggests they are not able to produce accurate results for more complex wave modes. These are plain bulk waves traveling in an infinite and uniform piezoelectric material. The analytical computation of partial waves is achieved by assuming a uniform material with no boundaries and solving the coupled Christoffel equations on it (Eqn.2.10 and 2.11). The analytical results, derived and solved without approximation, are considered the most accurate and serve as the reference. This reference provides a robust framework for validating our simulation methods' accuracy by comparing wave propagation velocities (calculated by Equation 2.32) and the presence of specific vibration patterns between the analytical computations and those obtained using COMSOL simulations with our method (hereafter referred to as our results in this section). This section will simulate partial waves propagating along the X-axis on PZT-5H ceramic. Although up to five partial wave modes may exist in a given scenario [34], the focus is placed on three partial waves where acoustic energy dominates. These waves are primarily composed of the fundamental vibration modes of piezoelectric devices.

The stiffness, piezoelectric coupling, and relative dielectric constants are detailed in the Appendix, under Chapter A. Initially, analytical calculations are employed to determine the properties of these three partial waves, as presented in Table 2.13.

Velocity	polarization of displacement	property	E-field exist?	H-field exist?
1769.1504 m/s	along Y-axis	purely acoustic	no	no
2372.5287 m/s	along Z-axis	stiffened	yes	no
4118.3329 m/s	along X-axis	quasi-acoustic	yes	yes

Table 2.13: The properties of three partial wave modes propagating along the X-axis on PZT-5H ceramic, the acoustic energy dominates.

The same model is then built in COMSOL, where a cuboid is used as the geometry. The

dimensions of the cuboid are 100 μm $\times$ 20 μm $\times$ 30 μm (Width $\times$ Depth $\times$ Height). These three different sizes distinguish partial waves propagating along different axes. Periodic boundary conditions are applied on three pairs of opposite faces to simulate an infinite substrate. Figure 2.2 illustrates the obtained velocities and vibration patterns.

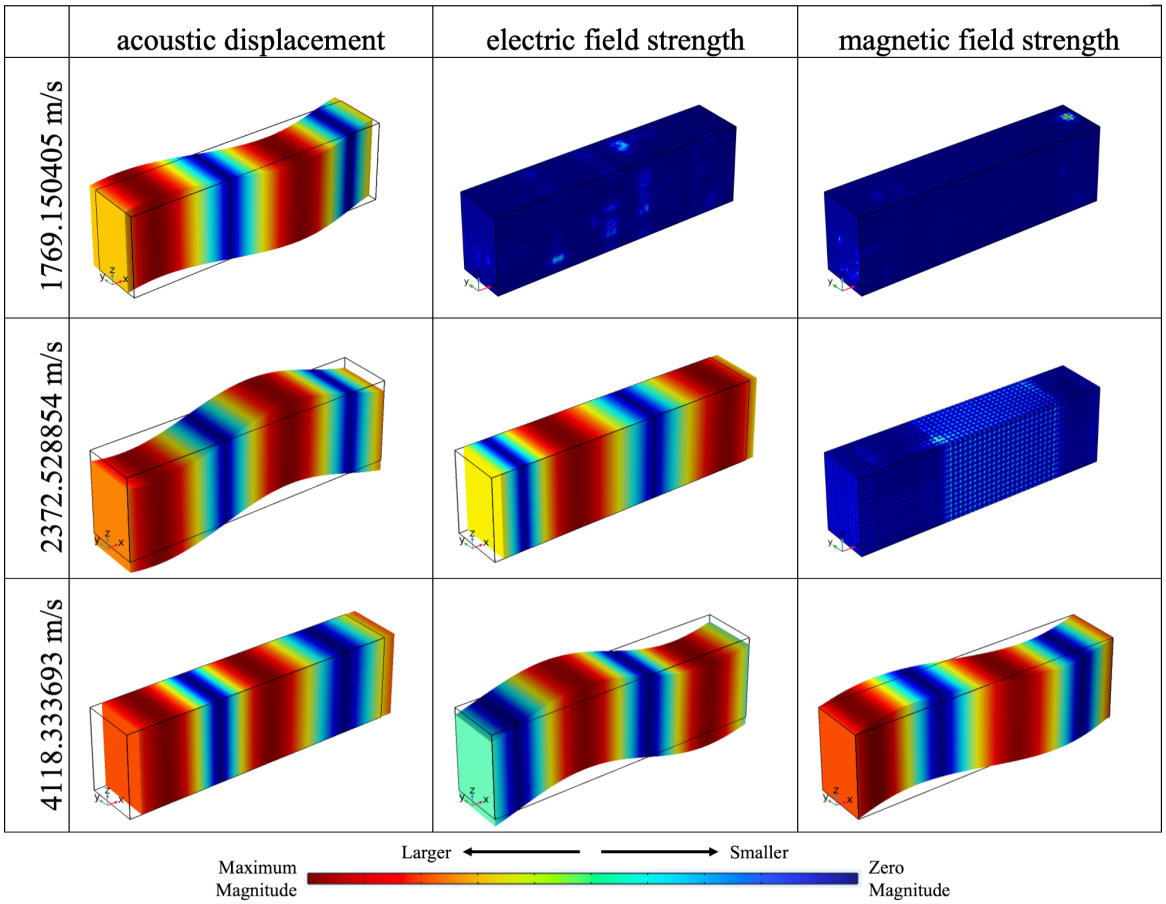


Figure 2.2: The illustration for properties of three partial waves, including their velocities and vibrations in the acoustic, electric, and magnetic fields. The colour bar indicates the amplitude of the vibrations. Our method, combined with COMSOL, is used to obtain these results.

These velocities differ only by up to 0.0007 m/s from analytical results, and the vibration patterns match perfectly. These results show that our method is highly accurate and capable.

On the contrary, results obtained from COMSOL with built-in *Solid Mechanics* and *AC/DC* modules are not satisfactory. This method (hereafter referred to as the built-in method) was widely regarded as an effective method of simulating fields generated by piezoelectric devices. The same model is used, and the results are shown in Figure 2.3.

The results show that the built-in method fails to simulate the electric field of the partial wave

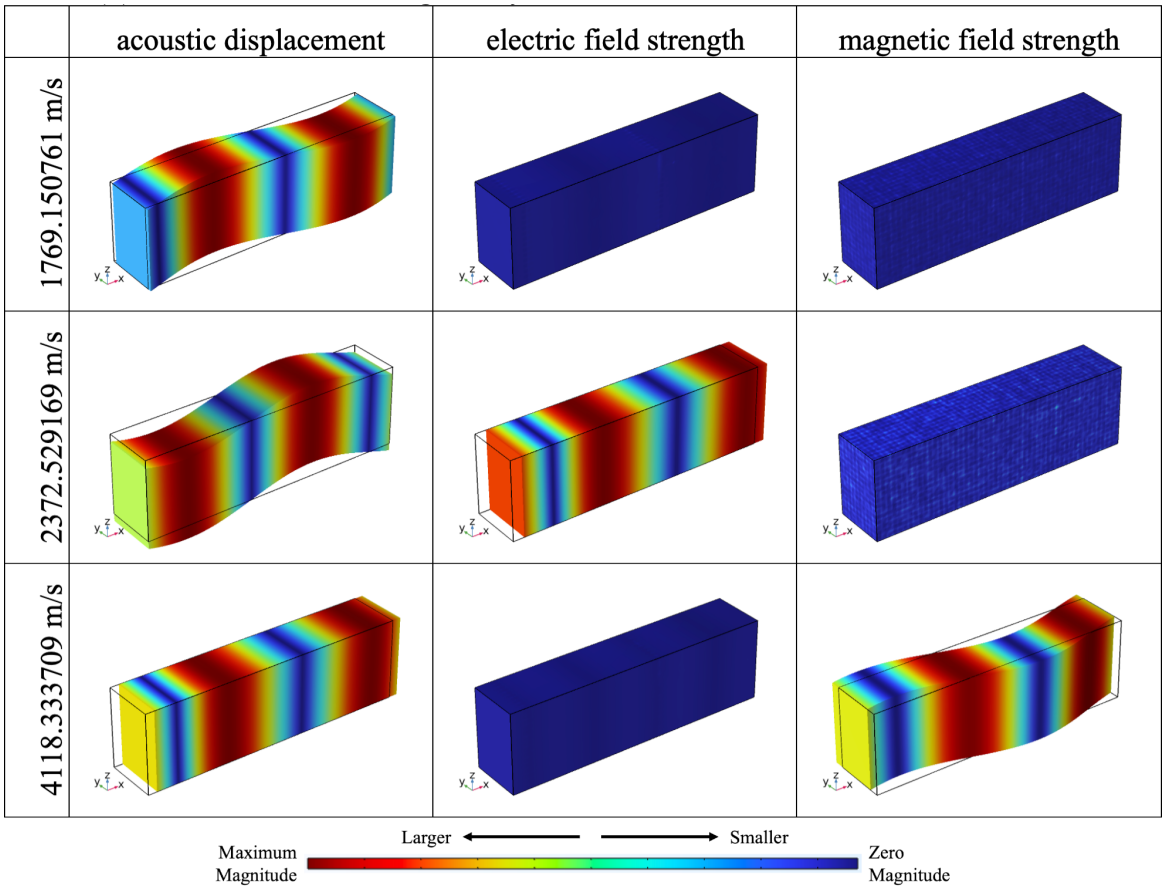


Figure 2.3: A similar illustration for details of three partial waves. The COMSOL with built-in *Solid Mechanics* and *AC/DC* packages are used. The blue in the electric field of the third partial wave shows the absence of the result, suggesting an inadequacy in the simulation method.

travelling at approximately 4118 m/s. Furthermore, each velocity exhibits greater inaccuracy compared to our method. These results show the built-in method's inadequacy for simulating fields around piezoelectric devices, both in terms of accuracy and reliability.

2.5.2 Rayleigh Mode on an Infinitely Large Substrate

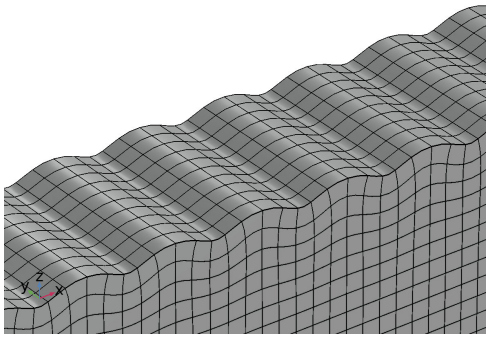


Figure 2.4: A sketch of the Rayleigh mode being modelled in this paper.

The focus here is solely on how the SAW propagates -as opposed to how it is generated and detected using interdigital transducers (IDTs). The domain analysed can be divided into two cuboids: one contains the piezoelectric substrate, and the other includes the surrounding environment. The surface of the substrate separates these two cuboids. Spatial coordinate axes are chosen such that x is oriented along the direction of propagation, y lies along the surface and is perpendicular to x, while z is outward normal to the surface. When no rotation is applied, the material coordinates (or crystal axes used by Auld [34]) align with the spatial coordinates.

A Rayleigh mode generally generates a relatively strong and analytically calculable magnetic field. The verification of our method thus focuses on its simulation. Figure 2.4 shows a schematic diagram of the Rayleigh mode. Boundary conditions suitable for this mode are applied: A periodic boundary condition is applied on the propagating direction (surfaces ① & ② and their opposites in Figure 2.5(a)). The distance between these two surfaces is set as 100 μm, which will become the Rayleigh mode's wavelength. Another periodic boundary condition is applied in the y direction (surfaces ④ & ⑤ and their opposites in Figure 2.5(a)). Since the Rayleigh mode is uniform in this direction, the distance between the two surfaces does not influence the form of the solution. This distance is set as 10 μm. The fixed constraint is applied in z direction (surface ③ and its opposite in Figure 2.5(a)). The Rayleigh mode is evanescent in this direction so that 300 μm, which is three times as long as the wavelength, is set as the distance from the surface to the fixed constraint. The electromagnetic continuity boundary condition is applied on surface ⑥, whereas this boundary is set as a free boundary for the acoustic field. For some metallised surfaces, an electric-wall boundary condition needs to be applied on surface ⑥. In this simulation, $z < 0$ (Area **A** in Figure 2.5(a)) is filled with piezoelectric material and $z > 0$ (Area **B** in Figure 2.5(a)) is chosen to be air. $z = 0$ is the surface of the substrate. COMSOL's built-in material properties are used.

The acoustic displacement field, electric field and magnetic field of the X-propagating Rayleigh mode on Z-cut $LiNbO_3$ are illustrated in Figure 2.5 (b), (c) and (d), respectively; the fields shown have been normalised. Comparison among experimental results, analytical results and our FEM method results of SAW velocities is shown in Table 2.14. Velocities of different materials and different modes with different boundaries are included, and they are calculated

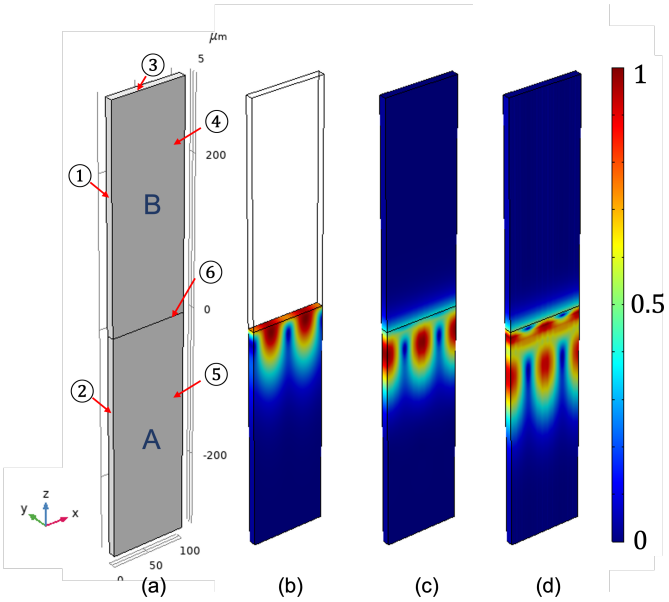


Figure 2.5: (a) Geometry of the infinitely large substrate model. "A" and "B" symbolise the areas of the piezoelectric substrate and air, respectively. The simulation results of normalised (b) acoustic wave, (c) electric wave and (d) magnetic wave patterns for the Rayleigh mode on X-prop Z-cut $LiNbO_3$ are shown. Fields with larger magnitudes have warmer colours. Note that these three waves already decayed significantly before reaching $LiNbO_3$-air interface. Relative to the buried magnetic field in the substrate, the accessible magnetic field in the head space above is thus substantially weaker.

Table 2.14: Comparison between velocities obtained from methods.

Material	Mode	Boundary	Direction	Experimental Results (m/s)	Analytical Results (m/s)	Our Results (m/s)	Relative Error (%)
CdS	Rayleigh	Free	X-prop Y-cut	1730[47]	1731.0007	1731.2782	0.016031
ZnO	Rayleigh	Free	X-prop Y-cut	2690[48]	2695.4553	2695.4558	0.000019
PZT-4	Rayleigh	Free	X-prop Y-cut	2120[49]	2241.8391	2241.8401	0.000045
PZT-5H	Rayleigh	Free	X-prop Y-cut	-	2038.4889	2038.4892	0.000015
PZT-5A	Rayleigh	Free	X-prop Y-cut	-	1977.6175	1977.6186	0.000056
$LiTaO_3$	Rayleigh	Free	X-prop 36°Y-cut	3124[50]	-	3114.0920	-
$LiTaO_3$	Rayleigh	Metallised	X-prop 36°Y-cut	3122[50]	-	3114.0791	-
$LiTaO_3$	Leaky	Metallised	X-prop 36°Y-cut	4099[50]	-	4075.4072	-

according to Equation 2.32. The relative errors of our results compared with analytical results are defined as:

$$\text{relative error} = \frac{v - v_A}{v_A} \tag{2.33}$$

where v denotes our results and v_A denotes the analytical results. The analytical results are calculated using the method introduced by Tseng [48]. All results of our method were calculated using 1.7 μm Element Size. Note that the built-in densities of CdS and ZnO are different from standard values, so the standard values should be input manually. Furthermore, the slowness surface of 128° Y-cut $LiNbO_3$ is simulated and plotted (Figure 2.6). Experimental results from

the literature[3] are also included for comparison. The FEM-simulation results are found to lie very close in value to the analytically calculated ones. Both lie reasonably close to what is measured experimentally. These proximities strongly suggest that our method is correct and accurate. The small residual differences stem from experimental measurement errors, the choice of tolerance in the bi-section method used to solve the analytical equation, and the fineness of the mesh used in our FEM method.

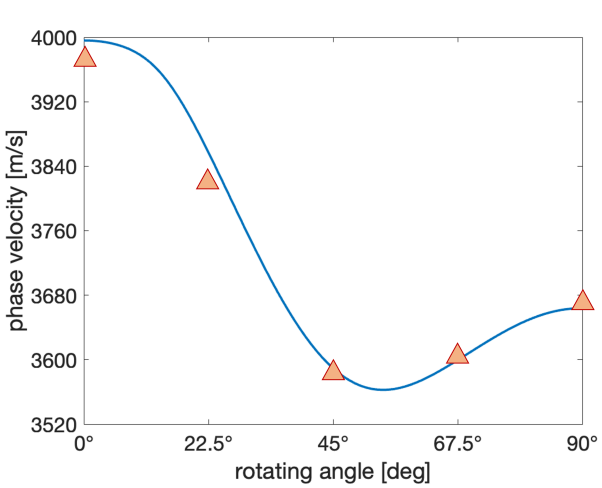


Figure 2.6: Comparison of simulated (blue line) and measured [3] (amber triangles) Rayleigh velocities corresponding to different propagating directions on 128° Y-cut $LiNbO_3$. In the simulation, the propagating direction is initially along the X-axis and then rotates anti-clockwise.

After confirming the accuracy of this model, it is then used to calculate the magnetic coupling coefficients. The calculating method is detailed in Section 2.4.6. The frequency of each calculation is set to 106.5 MHz, which is the transition frequency between T_x and T_z in Pc:PTP. The results are shown in Table 2.15, with materials and directions specified. This table tells that the coupling coefficients of Rayleigh mode are too low for building a maser cavity when the materials in this table are used.

2.5.3 Torsional Mode of a Cylinder Antenna

The example of a T_{00} torsional mode is presented because it generates a strong magnetic field, which can be used as the basis for designing an electromagnetic antenna. In addition, unlike the Rayleigh mode, the complexity of this torsional mode exceeds the limits of analytical methods,

Materials	Directions	Coupling Coefficents
ZnO	X-prop Z-cut	1.76E-14
ZnO	X-prop Y-cut	4.37E-14
PZT-5H	X-prop Z-cut	7.23E-13
PZT-5H	X-prop Y-cut	3.13E-12
LiNbO3	X-prop Z-cut	5.01E-12
LiNbO3	X-prop Y-cut	1.26E-13
LiNbO3	X-prop 128 Y-cut	4.59E-12
LiTaO3	X-prop Z-cut	4.98E-13
LiTaO3	X-prop Y-cut	2.96E-14
CdS	X-prop Z-cut	3.64E-15
CdS	X-prop Y-cut	4.98E-15
PZT-5A	X-prop Z-cut	2.06E-12
PZT-5A	X-prop Y-cut	3.08E-12
PZT-4	X-prop Z-cut	2.21E-13
PZT-4	X-prop Y-cut	3.08E-12

Table 2.15: The coupling coefficients for Rayleigh mode with different materials.

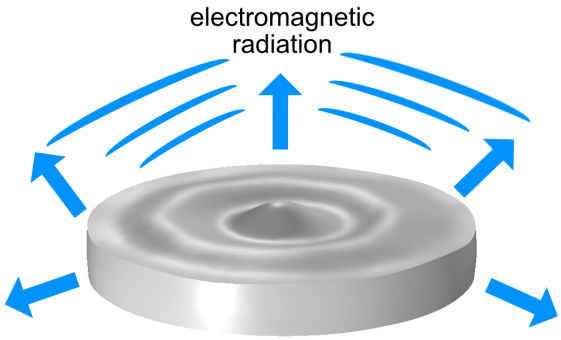


Figure 2.7: A sketch of the cylinder antenna being modelled in this paper. An axially symmetric normal mode is shown.

which showcases the capability of our method. The material is precisely on the equatorial plane, and the z-axis is motionless. Beyond this nodal plane and axis, the material rotates around the z-axis, the amplitude of displacement increasing with distance from the origin (shown in Figure 2.8(1)). In uni-axial materials like PZT-5H, this mode is significant. A cylinder made with other material, like $LiNbO_3$, will show a torsional mode only when the aspect ratio (defined as the ratio of height to the radius h/r) is substantial. [There is no hard cut-off, but a recommendation would be $h/r > 5$] If the aspect ratio is small, the frequency of the torsional mode is very high, with many other competing modes close to it (in frequency).

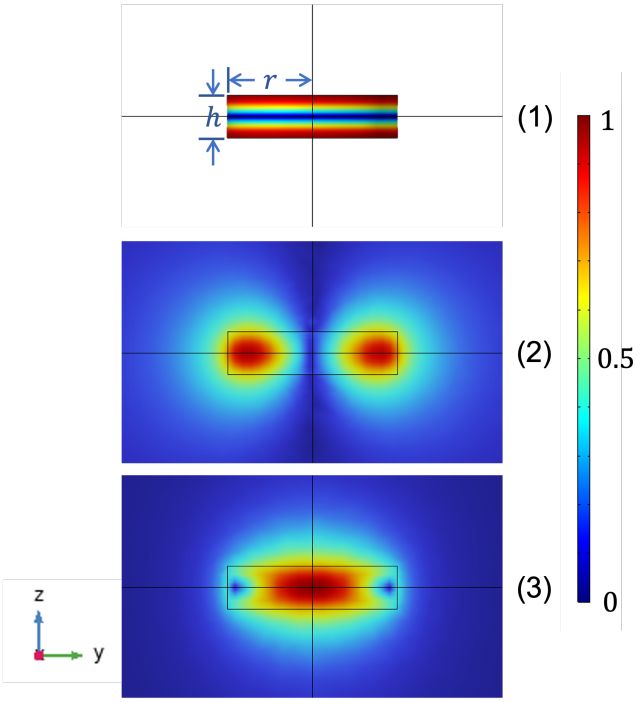


Figure 2.8: Normalised (1) acoustic displacement field, (2) electric field, and (3) magnetic field on the YZ section of a PZT-5H cylinder. Regions with larger magnitudes have warmer colours. The height and radius of this cylinder are 5 mm and 10 mm, respectively. The frequency of this mode is 175.12 kHz. Rotation directions on different sides are opposite from each other. The torsion generates a rotational electric field concentrated at the arc-shaped surface of the cylinder. This solenoid-like electric field then induces a magnetic field concentrated at the centre.

Simulations were conducted on a series of PZT-5H cylinders, varying in height from 1 to 5 mm, all with a fixed radius of 10 mm. In each simulation, the cylinder resides at the centre of a sphere, representing the surrounding environment. A continuous boundary condition is applied to the cylinder's surfaces, while an absorbing boundary condition is applied to the sphere's outer surface. As an example, the acoustic displacement, electric, and magnetic fields on the central YZ cross-section are shown in Figure 2.8. It is found that when the aspect ratio decreases, both the magnetic coupling coefficient and frequency will increase. Figure 2.9 shows the relation among those three quantities. The highest coupling coefficient in this model is 2.6×10^{-7} for a cylinder with a small aspect ratio of $(h/r = 0.1)$. In reality, the torsional mode is unlikely to appear on a disk with a very small aspect ratio, so the magnetic coupling coefficient should not be very high in this system. By changing the radius and thus the frequencies, we found that the coupling coefficients mainly depend on the aspect ratio, as

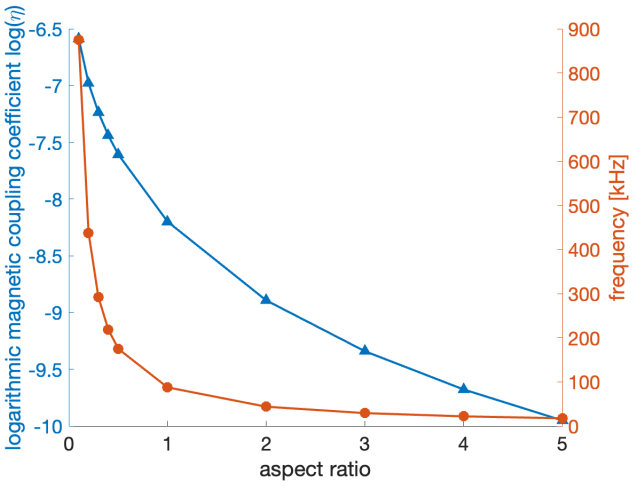


Figure 2.9: How frequency (orange circles) and magnetic coupling coefficient (blue triangles) vary with aspect ratio for the T_{00} torsional mode of a PZT-5H cylinder with a 10 mm radius. By connecting solid orange and blue lines, respectively. The sphere's radius containing the analysed air space surrounding the cylinder is 300 mm. When the aspect ratio decreases (*i.e.* the cylinder becomes squatter), both the frequency and the magnetic coupling coefficient increase. The magnetic coupling coefficient can reach 2.6×10^{-7} when the aspect ratio is 0.1. This value is extremely small, although it is the largest coupling coefficient ever observed. Given the difficulty in generating the T_{00} torsional mode on a very thin device, simulating a cylinder with an even smaller aspect ratio is considered unnecessary. Note that the coupling coefficient mainly depends on the aspect ratio rather than the frequency. Changing the size, and thus the frequency, does not affect the coupling coefficient.

they change very little with frequency.

Verification of the accuracy of our model was performed on fundamental modes. Shaw [4] measured the frequency of axial symmetric normal modes on barium titanate disks with different aspect ratios. The same modes were simulated using our method, and the corresponding resonant frequencies and acoustic displacement fields were compared with Shaw's results. A barium titanate cylinder was used in the simulation, whose height was set as 5 mm and radius changed from 2.5 mm to 17.5 mm. Barium titanate ceramic's properties (elasticity matrix, coupling matrix, and relative permittivity) were obtained from Dent [51]. Figure 2.10 plots the simulated and measured frequencies. The simulated acoustic displacement fields at the upper surface of the disk with two different aspect ratios are plotted and compared in Figure 2.11. These proximities suggest that our method is correct and accurate. The discrepancies stem from experimental measurement errors, the fineness of the mesh used in our method, and the accuracy of the properties of barium titanate. Note that an inverse aspect ratio of $2r/h$ was

used in Shaw's paper. To maintain consistency, the same quantity is used as the independent variable.

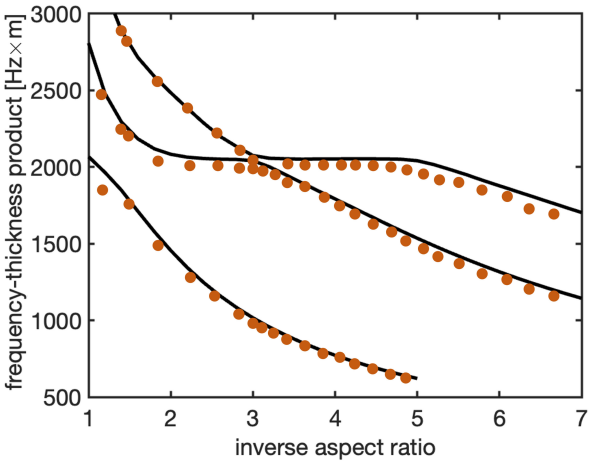


Figure 2.10: The stimulated frequencies-thickness product of three axial symmetric normal modes versus inverse aspect ratio (black curves). Simulations were performed in a barium titanate cylinder whose height was fixed (5 mm). Results are compared with experimental results (brown circles) measured by Shaw [4].

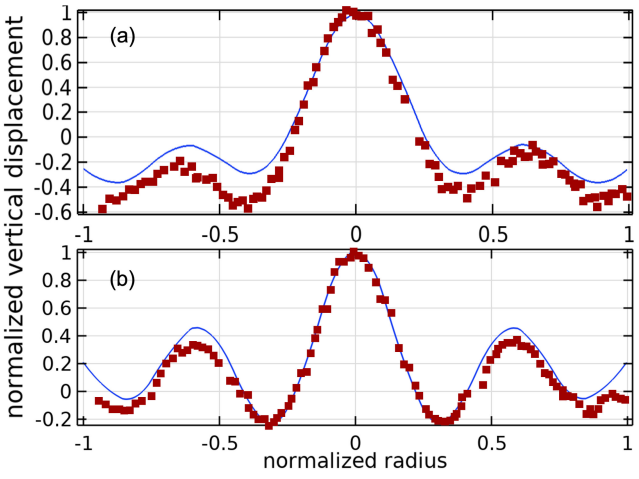


Figure 2.11: Normalised acoustic displacement fields of two axial symmetric normal modes versus normalised radius on the upper surface of a barium titanate cylinder. The results were obtained from our method (blue curves) and Shaw's experiments[4] (maroon squares). The height of the cylinder was set as 5 mm, and the inverse aspect ratio was set as $2r/h = 3.86$. The two modes were found at the frequency-thickness product (a) 2685 Hz×m and (b) 2885 Hz×m.

2.5.4 Relation between mesh size and error

The mesh size controls the accuracy of a COMSOL simulation. The smaller the mesh size is, the more accurate the results are. The relation between the relative error of our method and the mesh size is studied on the model introduced in Section 2.5.2 and illustrated in Figure 2.12. The results are compared with those provided by the built-in *Piezoelectric Effect* interface. The relative error is defined as:

$$relative\ error = \frac{v - v_s}{v_s} \tag{2.34}$$

where v is the velocity calculated by our FEM method and v_s is the standard velocity calculated using the analytical method [38], whose error is less than 10^{-11} m/s. From those two figures, one can find that the results of our FEM method converge to the analytical results when the mesh size decreases. This study suggests that our method is of high accuracy. In addition, although the built-in *Piezoelectric Effect* interface can generate results with similar accuracy, it is still less accurate than our method.

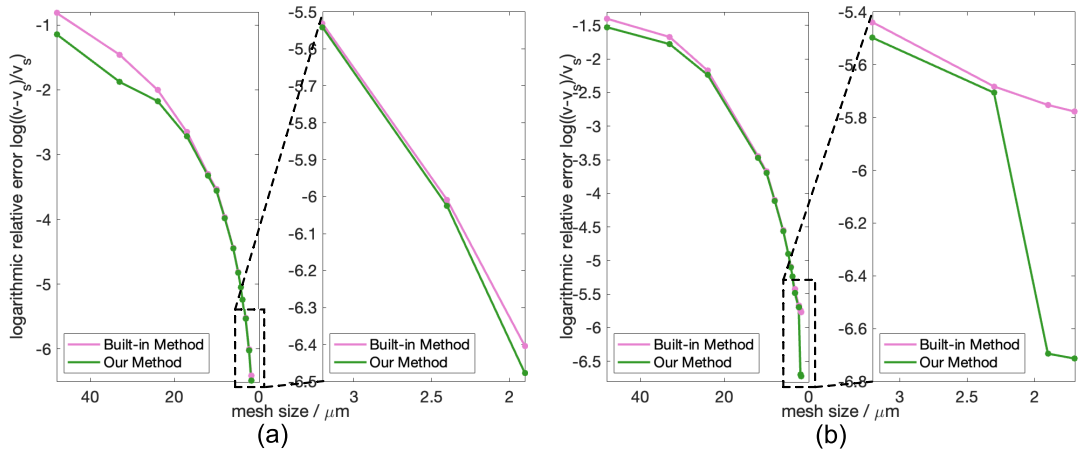


Figure 2.12: The plot of logarithmic relative error versus mesh size on (a) PZT-5H and (b) ZnO. The results of our method (green) and built-in *Piezoelectric Effect* interface (pink) are included. The left subplot in each figure illustrates all results, and the right one only focuses on results with smaller mesh sizes.

Now, we discuss the accuracy of the analytical method and our method. The analytical method is introduced in Tseng's work[38]. In this method, no approximation is used, and thus, high accuracy is guaranteed. However, errors still stem from the discrepancies between the real and input properties of piezoelectric materials (elasticity matrix, coupling matrix, and relative

permittivity) and the bisectional method applied. Corresponding errors should be in the same order as the choice of tolerance in the bi-section method. In our method, there are two main components: the weak forms and the FEM method used to solve them. As weak forms are the default representation of differential equations in COMSOL, it is reasonable to believe that our weak forms don't introduce errors. As in other FEM methods, discretization errors arise from the creation of the mesh. This is also the reason why accuracy will increase when one chooses a smaller mesh size. The same errors from the discrepancies of the properties still exist. Therefore, when the same group of properties is used, the convergence of our results to the analytical results as mesh size decreases indicates the accuracy of our method.

2.5.5 Relation between mesh size and calculation time

The growth of calculation time with decreasing mesh size is studied in the same model introduced in Section 2.5.2. PZT-5H and ZnO are used. The results are obtained from our method as well as a built-in method configured with the *Piezoelectric Effect* interface. In this study, all settings remained unchanged except the mesh size. There were 6 eigenfrequencies found in each run. This study is conducted on a MacBook Pro with an M1 Pro CPU and 16 GB of RAM. Note that although this CPU has 10 cores, only 4 of them are allowed to be used by COMSOL, which we have found to be the ideal setting for the parallel computing performance of COMSOL.

Figure 2.13 shows that the calculation time increases dramatically as the mesh size decreases. However, in our method, the relative error (as defined in Eqn.2.34) is already smaller than 10^{-5} when the simulation takes less than 20 s. In this study, at this level of error, the built-in method is approximately twice as fast as our method.

Note that this statement is not always true. For example, when calculating the partial waves, the built-in method took 1 hour 23 minutes 52 seconds (5032 seconds), while our method only took 17 minutes 32 seconds (1052 seconds). We, therefore, believe our method is of reasonable computational efficiency compared to the built-in method.

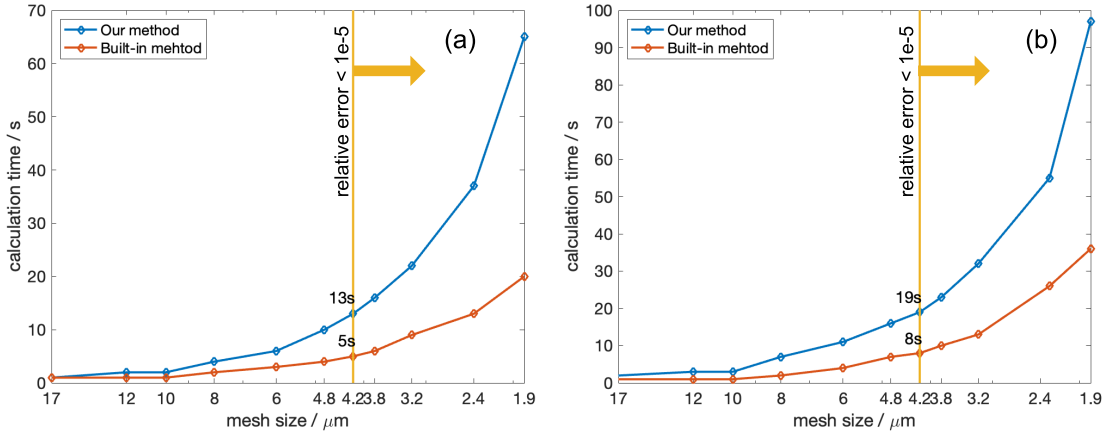


Figure 2.13: The plot of calculation time versus the maximum mesh size on (a) PZT-5H and (b) ZnO. The results of our method (blue) and built-in *Piezoelectric Effect & Magnetic Field* interfaces (orange) are included.

2.6 Conclusion

This research fills a fundamental "blind spot" in the electromagnetic simulation of devices involving piezoelectric crystals/substrates: mechanical motion in piezoelectric materials generates magnetic fields, which need to be precisely quantified. A lack of such simulation leads to numerous limitations, such as the inability to calculate the Poynting vector, which is the radiation energy flow of an antenna. An efficient and cost/resource-effective simulation method has been developed to address the problem, as described in this section. This method is generic, based on so-called "weak forms", and can be implemented in any finite-element-method simulation software. Due to its fundamental scope and connections to various areas in applied device physics, this practical method is expected to be useful in the simulation of numerous fields, including SAW-based resonators, piezoelectric antennas, and magnetically sensitive quantum devices involving spins.

Table 2.15 and Figure 2.9 present the calculated magnetic coupling coefficients. For T_{00} torsional modes on piezoelectric disk antennas, the coefficients are typically below 10^{-6}, whereas for Rayleigh modes on waveguides, they are below 10^{-12}. These low values preclude the construction of effective maser cavities, as generating a sufficiently strong magnetic field to interact with maser gain materials would demand an impractically large amount of electric or mechanical energy. Consequently, the current configurations are unsuitable for practical applications.

Nonetheless, these results imply that modifying the geometry could substantially increase the magnetic coupling coefficients. Future research should prioritize identifying specific geometries that produce coupling coefficients large enough for practical applications. One example is the standing wave mode, which corresponds to the mode proposed in Section 2.1.1. This mode differs from the propagating Rayleigh mode discussed in Section 2.5.2 as a wave reflector, which can be simplified as a Dirichlet boundary condition, is placed at one end. Preliminary results indicate that the coupling coefficients for this mode may reach the order of 10^{-3}. If this mode is exploited, the support of the gain material can be placed on the wave node, between the reflector and the IDTs.

There are several directions for future research. In this work, the "eigenvalue" study in COMSOL is used. By introducing time derivatives into the weak form equations, a time-dependent study can be performed. This allows investigation of (a) how waves propagate along the waveguide and (b) how modes respond to an input signal, including detuning. In addition, the simulation can be made more realistic by incorporating further details. For example, IDTs can be included to represent practical systems better. Furthermore, material losses, which are neglected in the current study, can be accounted for by introducing imaginary components into the material property values. This research will become a powerful tool for full simulations of piezoelectric devices, especially when the magnetic fields are significant.

Chapter 3

Zero-field Time-resolved EPR Spectroscopy

3.1 Introduction

In addition to developing novel maser cavity designs, another approach to achieving a continuous-wave maser is to identify new maser gain materials. Time-resolved electron paramagnetic resonance (ZF-trEPR, or EPR in the following sections) spectroscopy is a crucial characterization method that provides insights into the dynamic mechanisms of short-lived paramagnetic species generated by photoexcitation [52]. For instance, it can reveal the encounter of photoexcited triplet states and radicals [53, 54], as well as triplet dynamics, which is a key focus of this project. EPR offers a quick and straightforward method for characterizing new maser materials. It examines relaxation processes and depopulation mechanisms, and the corresponding rates can be extracted from the EPR data by fitting a bi-exponential function. These rates are essential for simulating maser dynamics (Chapter 4), calculating the maser threshold, and estimating the quantum memory lifetime [55]. Moreover, the EPR cavity is relatively easy to construct, and its resonant frequency can vary over a wide range, which aids in identifying the transition frequencies of maser gain materials. Furthermore, if no significant EPR signals are observed at a particular transition, it suggests that building a maser based on that transition

is unlikely. This property makes EPR a valuable tool for predicting the performance of new masers.

This chapter is organized into four sections. Section 3.2 delves into the theoretical framework of ZF-trEPR spectroscopy. Section 3.3 introduces the structure and functions of our EPR spectrometer. Section 3.4 offers a step-by-step guide to conducting EPR experiments. Finally, Section 3.5 discusses the results obtained from these experiments.

3.2 Theory

Following each laser pulse, the population inversion is established in the triplet state T_1 and subsequently reduced through spin-lattice relaxation and depopulation. EPR spectroscopy is employed to observe the effects of these two mechanisms by monitoring the time evolution of the population densities. To achieve this, critical coupling is utilized. Initially, the cavity is critically coupled with the transmission line, ensuring that the impedances of both components are matched. Consequently, the cavity absorbs all input microwave energy, resulting in no reflection. However, when transitions occur between the triplet-state sublevels, the impedance of the cavity changes, causing the microwave to be reflected. This reflected microwave carries valuable information about the population densities. Notably, the stimulated emission is disregarded because the input signal is weak, and the stimulated emission rate is significantly lower compared to the spin-lattice relaxation and depopulation rates.

3.2.1 Relaxation

Relaxation refers to the processes that restore the spins to thermal equilibrium following their polarization. These processes are categorized into two types: spin-lattice relaxation and spin-spin relaxation.

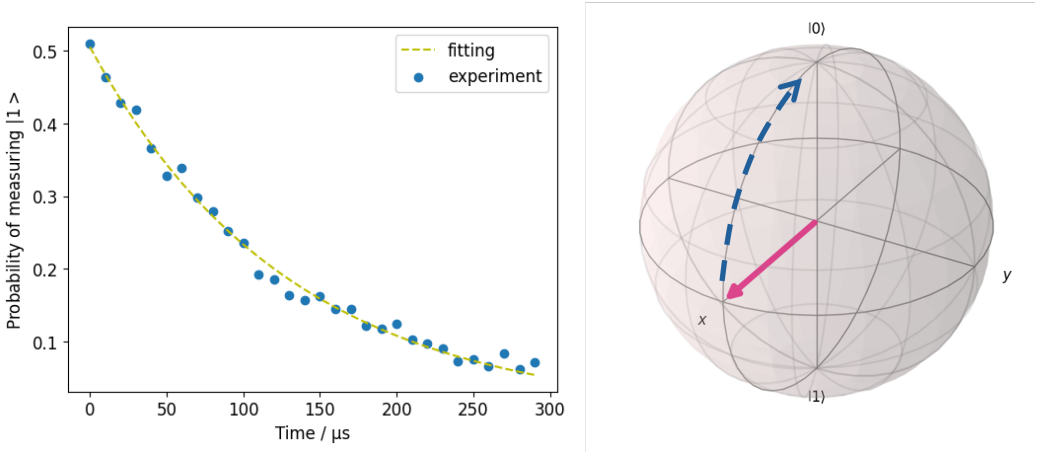
Spin-lattice Relaxation

As its name suggests, spin-lattice relaxation involves the transfer of energy from spins to their surrounding lattice. This energy transfer causes an exponential decay of spins from their excited states to the ground states in three sublevels. Spin-lattice relaxation can also be described in two ways: (a) the exponential decrease of the diagonal elements of the spins' density matrix and (b) the exponential return of the longitudinal component of the magnetic moment vector from the excited state to its equilibrium state, aligned with the external magnetic field. Consequently, spin-lattice relaxation is also known as longitudinal relaxation. It is characterized by the relaxation time constant, $\mathcal{T}_1$, which represents the time required for the excited state to decay to $1/e$ of its initial value. A longer $\mathcal{T}_1$ indicates greater stability of the excited spins, enabling more quantum operations.

Consider an isolated two-level system. Several methods exist for measuring $\mathcal{T}_1$ in this simplified model. One example is illustrated in Figure 3.1. In this experiment, 30 spins are initialized in the superposition state $|0\rangle + |1\rangle$. For each spin, the probability of finding it in the $|1\rangle$ state is measured after a specified delay, with delays ranging evenly from 0 to 300 µs. The resulting probabilities for the 30 spins are plotted in Figure 3.1, and an exponential fit is applied using the function $y = a \cdot \exp(-bx)$. The relaxation time $\mathcal{T}_1$ is then determined from the fit, with $\mathcal{T}_1 = 1/b$.

In maser gain materials, spin-lattice relaxation occurs among triplet state sublevels, which are crucial in determining the co-opertivity (Equation 1.13) and quantum memory lifetime [56]. As shown in Equation 1.13, having a longer spin-lattice relaxation time, and thus increasing the cooperativity, helps improve the chances that the maser will work. The transition rate from the i-th level to the j-th level is denoted as w_{ij}. At thermal equilibrium, the number of particles that transit upward and downward must be identical to maintain a static population ($\dot{n_x} = \dot{n_y} = \dot{n_z} = 0$). Hence, the transition rates have an inverse Boltzmann relation as Equation 1.1 [57]:

$$\frac{w_{ij}}{w_{ji}} = \frac{n_i}{n_j} = \exp\left(-\frac{E_i - E_j}{k_B T}\right) \tag{3.1}$$



(a) (b)

Figure 3.1: (a) The figure illustrates the measurement of relaxation time $\mathcal{T}_1$. The x-axis represents the delay time, while the y-axis shows the probabilities of finding the state $|1\rangle$. The blue points correspond to the measurement results of 30 qubits, and the green dashed line represents the fitted curve. The fitting process determines that $\mathcal{T}_1 = 129.75$ µs. This data is derived from a simulation conducted on FakeLagosV2 using Qiskit (Qiskit, 2024). (b) The figure visualises the spin-relaxation process corresponding to this measurement. Initially, the state vector points along the x-axis and gradually transitions towards the z-axis, demonstrating the relaxation dynamics.

When the temperature is high enough, the exponential function on the right-hand side approaches 1, then w_{ij} and w_{ji} are approximately equal. At room temperature (298 K), this approximation is valid. For example, when substituting the energy difference of pentacene at three sublevels of T_1 triplet state, the ratios of transition rates are $\omega_{zx} : \omega_{xz} = 0.99977$, $\omega_{zy} : \omega_{yz} = 0.99978$, and $\omega_{yx} : \omega_{xy} = 0.99998$.

Spin-spin Relaxation

Spin-spin relaxation occurs in a group of spins, where the transverse components (those perpendicular to the external magnetic field) rotate at different rates. This leads to a gradual loss of phase coherence, as illustrated in Figure 3.2. This process is also referred to as spin dephasing or spin decoherence.

The mechanism of spin-spin relaxation arises from interactions among the spins, making discussions at the level of a single spin somewhat trivial. It can be characterized as the exponential decay of the off-diagonal elements in the density matrix of the spins. The relaxation time $\mathcal{T}_2$

represents the duration required for the transverse magnetization to decay to $1/e$ of its initial value. In most systems, $\mathcal{T}_2$ is shorter than $\mathcal{T}_1$, indicating that transverse relaxation occurs more rapidly than longitudinal relaxation.

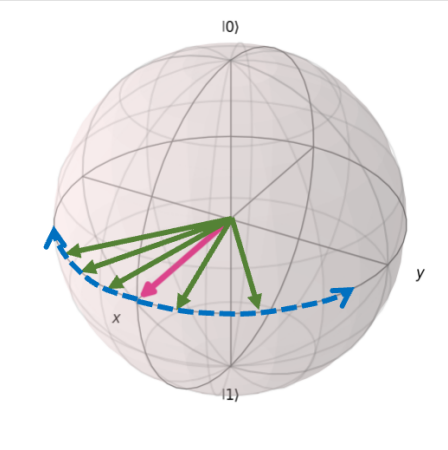


Figure 3.2: An illustration of the spin-spin relaxation mechanism. Initially, multiple spins are aligned along the x-axis (represented by the red vector). Over time, due to interactions between spins, they begin to spread out, eventually reaching the positions indicated by the green vectors. This dispersion of spins leads to the gradual loss of the initial spin coherence.

Dynamical decoupling is a widely used technique for suppressing spin decoherence effects [58]. It operates on a principle similar to that of the spin echo method [59], wherein a specific sequence of pulses is applied to restore quantum coherence. The details of this approach are illustrated in Figure 3.3.

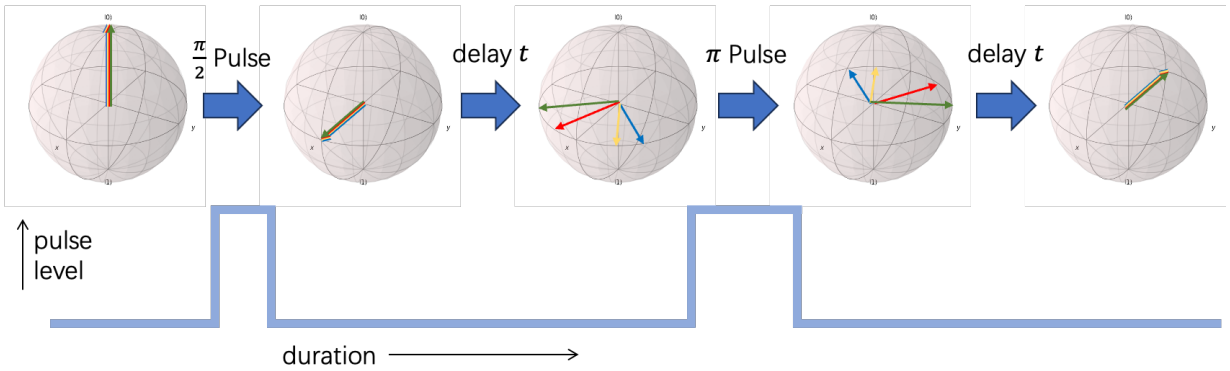


Figure 3.3: The details of applying dynamic decoupling. Assume there is only the spin-spin relaxation. The process is visualised on a Bloch sphere in the first line, with the corresponding pulse sequence shown in the second line. A $\pi/2$ pulse is initially applied to rotate the spins from the z-axis to the x-axis. Subsequently, spin-spin relaxation causes the spins to rotate at different rates. After a delay of t seconds, a π pulse is applied, which inverts the spins. Following another delay of t seconds, the spins reunite along the negative x-axis, signifying the reconstruction of quantum coherence.

In addition to spin-spin relaxation, other factors, such as magnetic field inhomogeneities and instrumental imperfections, can further differentiate the rotating speeds of spins. The combined effect of these factors is characterised by the ensemble dephasing time, denoted as $\mathcal{T}_2^*$. Note that $\mathcal{T}_2^*$ is always shorter than $\mathcal{T}_2$ because it incorporates additional dephasing effects.

Although the spin-spin relaxation rate can also be measured by EPR spectroscopy, it is not involved in this thesis.

3.2.2 Rate Equations of the Triplet State

The rate equations describe how the population densities of the T_1 sublevels change over time. These equations are based on 12 mechanisms, including pumping, spin-lattice relaxation, and depopulation, as shown in Figure 3.4.

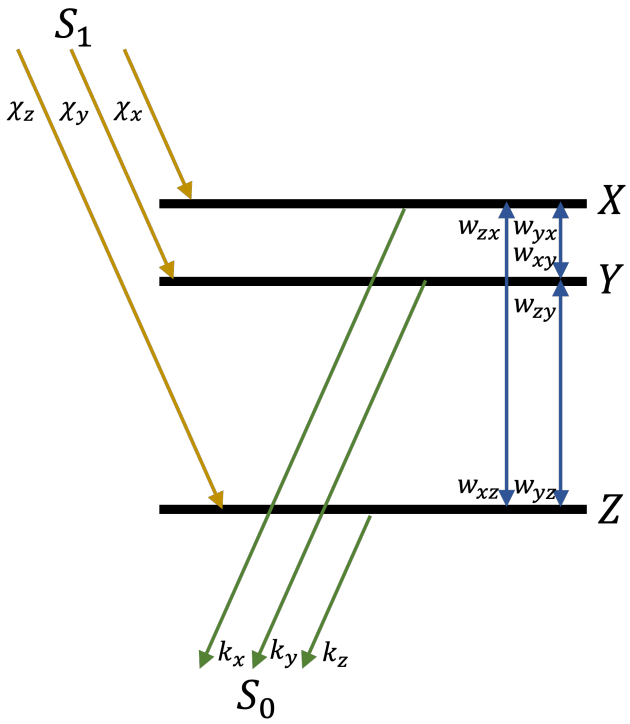


Figure 3.4: Illustration of the rates affecting the population densities of the triplet state T_1. Blue arrows represent transitions among the triplet sublevels, yellow arrows the ISC from the excited singlet state S_1, and green arrows show the decay processes from the triplet state to the ground state S_0.

The pumping procedure refers to the intersystem crossing (ISC), which transfers excited electrons to three sublevels at rates denoted as χ_x, χ_y, and χ_z. In EPR studies, the ISC starts

with the laser pulse and lasts about 5 nanoseconds. Since the duration of ISC is significantly shorter than the timescale of EPR signals, which typically last for at least several milliseconds, it is treated as an instantaneous process. Therefore, an initial population inversion is assumed without explicitly modeling the pumping process.

Once this initial population inversion is established, the total number of spins is considered constant. From this point, only two processes influence the spin population densities of the three sublevels: depopulation and spin-lattice relaxation. Assuming identical rates for upward and downward spin-lattice transitions, the system can be described using a total of six free parameters. The time evolution of the spin population densities is governed by a set of coupled differential equations, commonly known as the rate equations.

$$\dot{n_x} = -(k_x + w_{xy} + w_{xz})n_x + w_{yx}n_y + w_{zx}n_z \tag{3.2}$$

$$\dot{n_y} = -(k_y + w_{yx} + w_{yz})n_y + w_{xy}n_x + w_{zy}n_z \tag{3.3}$$

$$\dot{n_z} = -(k_x + w_{zx} + w_{zy})n_z + w_{xz}n_x + w_{yx}n_y \tag{3.4}$$

or in the matrix-multiplication form:

$$\begin{bmatrix} \dot{n_x} \\ \dot{n_y} \\ \dot{n_z} \end{bmatrix} = \begin{bmatrix} -(k_x + w_{xy} + w_{xz}) & w_{yx} & w_{zx} \\ w_{xy} & -(k_y + w_{yx} + w_{yz}) & w_{zy} \\ w_{xz} & w_{yx} & -(k_x + w_{zx} + w_{zy}) \end{bmatrix} \begin{bmatrix} n_x \\ n_y \\ n_z \end{bmatrix} \tag{3.5}$$

where n_x, n_y, and n_z denote the time-dependent population densities on three triplet sublevels. k_i is the depopulation rate from the i-th state to the ground state S_0, and w_{ij} is the spin-lattice relaxation rate from the i-th state to the j-state. By fitting the EPR results to the rate equations, both types of rates—six values in total—can be determined. As will be demonstrated in Section 3.5, fitting the results corresponding to each transition yields two relationships among

the rates. This indicates that all six rates can be fully revealed only by analysing the results of all three transitions.

3.2.3 Detection

As aforementioned, when transitions happen in EPR experiments, the microwave will be reflected and carry the desired information. Some oscilloscopes cannot directly capture and analyze this signal because of its high frequency. The oscilloscope used in this thesis, RIGOL DS1104 Zplus, has a bandwidth limitation of 100 MHz, which means a signal with a frequency higher than 100 MHz will be distorted when shown on this oscilloscope. Besides, the sampling rate of 1 GSa/s is also not high enough. This parameter means this oscilloscope captures 1 G sample points from an incoming signal, and according to the Nyquist theorem, the sampling rate must be at least twice the highest frequency component of the signal to represent a signal accurately without aliasing [60].

In this experiment, we use I-Q homodyne detection to address this problem. This technique converts a microwave signal down to its baseband and amplifies the signal's amplitude, effectively boosting the signal-to-noise ratio. The principle of the I-Q homodyne detection is presented below.

At first, the supplied microwave is decomposed into two branches: the local oscillator (LO) branch with an amplitude of A_1 and a phase of ϕ_1, and the radio frequency (RF) branch with an amplitude of A_2 and a phase of ϕ_2. The RF branch signal is the modulated carrier signal that carries the information of population densities in the triplet state. The combination of the signals from these two branches with a mixer gives:

$$V_1 = A_1 \cos(\omega t + \phi_1) \cdot A_2 \cos(\omega t + \phi_2) \tag{3.6}$$

$$= \frac{1}{2} A_1 A_2 [\cos(2\omega t + \phi_1 + \phi_2) + \cos(\phi_1 - \phi_2)] \tag{3.7}$$

If, in the meantime, the two signals are combined on another mixer with an extra 90° on ϕ_2, which changes one of the wave functions from cos to sin. The new combination is:

$$V_2 = A_1 \cos(\omega t + \phi_1) \cdot A_2 \sin(\omega t + \phi_2) \tag{3.8}$$

$$= \frac{1}{2} A_1 A_2 [\sin(2\omega t + \phi_1 + \phi_2) - \sin(\phi_1 - \phi_2)] \tag{3.9}$$

Each V_1 and V_2 has two parts: a high-frequency part at 2ω and a baseband part at 0. Two DC blockers filter out the high-frequency components, leaving only the baseband signals. The oscilloscope captures these signals on separate channels. The voltages shown on the oscilloscope are:

$$V_1 = \frac{1}{2} A_1 A_2 \cos(\phi_1 - \phi_2) \tag{3.10}$$

$$V_2 = -\frac{1}{2} A_1 A_2 \sin(\phi_1 - \phi_2) \tag{3.11}$$

$\phi_1 - \phi_2$ is the relative phase between two microwave signals. These two signals are 90° out of phase. The signals V_1 and V_2 are called the in-phase (I) and the quadrature (Q) signals, respectively. By adjusting the phase on one branch, the product of two amplitudes can be put on one channel. For example, when $\phi_1 - \phi_2 = 0$,

$$V_1 = \frac{1}{2} A_1 A_2 \tag{3.12}$$

$$V_2 = 0 \tag{3.13}$$

In this way, the amplitude of a microwave signal, whose waveform cannot be captured directly by oscilloscopes, is transformed into its baseband and amplified by a factor of A_2, shown on channel 1. This result is extracted from the oscilloscope and printed using PyVisa code (shown in Appendix D).

3.3 Instrumentation

This section elaborates on the construction of this spectrometer.

The resonant frequency observed in the experiment falls into two possible ranges: 10 MHz to 1 GHz (lower range) and 1 GHz to 2 GHz (middle range). The instrumentation and procedures employed differ slightly between these ranges. This section primarily focuses on the setup for the middle range, with the setup for the lower range being introduced by highlighting the differences.

3.3.1 Middle Frequency Range

The components will be introduced in the order of the microwave flow. The numbers in brackets, for example (#1), indicate the serial numbers and labels on Figure 3.5. They are connected using coaxial cables with SMA, BNC, or N-type connectors.

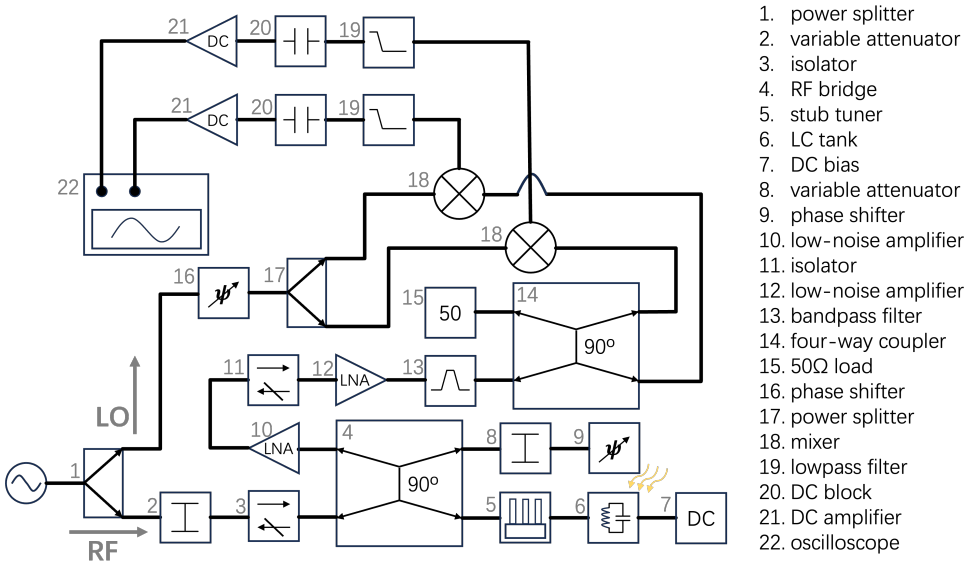


Figure 3.5: The internal structure of the EPR spectrometer.

A signal generator continuously supplies the microwave excitation, divided into the LO and RF branches by a power splitter (#1). The RF branch interacts with the maser gain material and carries the EPR signals, while the LO branch remains unchanged for reference purposes. Note that an isolator is placed right after the signal generator to protect it from back reflections.

The microwave signal in the RF branch transmits through a variable attenuator (#2) (ARRA Inc.) and an isolator (#3) before entering an RF bridge (#4). This RF bridge is a four-way coupler with a 90° phase shift between two ports. It is used to balance the circuit, *i.e.*, impedance matching [61]. This balance is highly sensitive to changes in the cavity's Q factor. The cavity (#6) is connected to the RF bridge via a stub tuner (#5), which helps with impedance matching. The other part of the contribution is found on the balancing arm, which consists of a variable attenuator (#8) and a phase shifter (#9). The output port collects the reflected signals, which are then directly connected to a low-noise amplifier (#10), followed by an isolator (#11) and another low-noise amplifier (#12). According to the Friis formula [62], positioning the amplifier with the lower noise figure closer to the RF bridge is essential. Subsequently, a bandpass filter (#13), covering the resonant frequency, attenuates any frequency not near the resonant frequency. The filtered signals are then split into two paths by a power splitter. This power splitter is a four-way coupler (#14) with one port connected to a 50 Ω resistance (#15). The splitter's two output ports deliver equal power signals but with a 90° phase difference.

The microwave on the LO branch transmits through a phase shifter (#16) (Narda Microline model 3752) before entering a power splitter (#17) without any phase difference.

The outputs from the two splitters (#14 and #17) are combined in pairs by two mixers (#18). These two pairs of combined signals have identical power and signal characteristics but differ in phase. The pair with a 90° phase difference becomes the Q (quadrature) branch, while the other pair becomes the I (in-phase) branch. Each output from the two mixers is then passed through a low-pass filter (#19), a DC block (#20) (which blocks all frequencies except the DC component), and a DC amplifier (#21), individually. Finally, these processed signals are displayed on two channels of an oscilloscope (#22) in the form of voltage.

In this experiment, an optical parametric oscillator (OPO) (Litron Aurora II Integra) is utilised as the source of optical pump light. The operating frequency of the OPO can be adjusted via its control panel. The beam is focused using two convex lenses onto the samples for irradiation, as illustrated in Figure 3.6. An optical filter is placed in this path to attenuate the power, which is measured by a laser power meter (Thorlabs PM100D). We adjusted the power based

on the thermal stability of the samples, and 0.6 mJ was used on Pc:PTP. The scattered light is captured by a photodiode, which triggers the oscilloscope measurement (Rigol DS1104 Z-Plus).

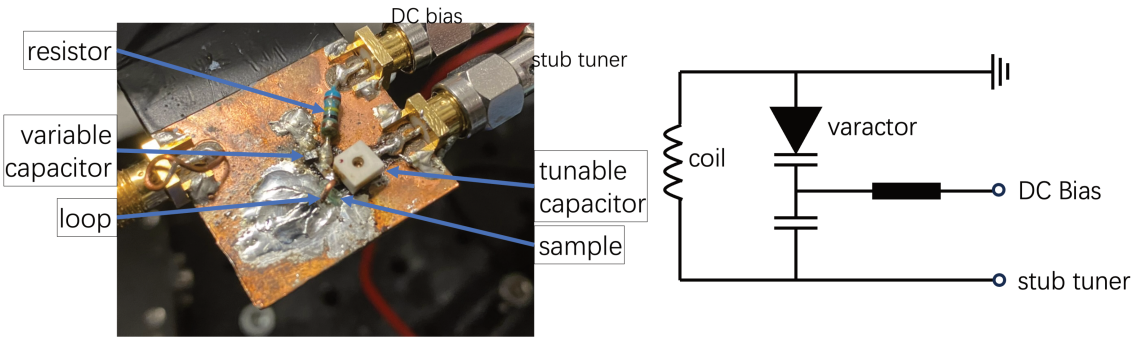


Figure 3.6: A photo of the LC resonator with labelled main components and its abstract circuit. The image also indicates the connections to the DC bias and stub tuner.

The resonator is an LC circuit comprising a tunable capacitor (ranging from 3 to 9 pF), a varactor diode (model BB833) acting as a controllable capacitor, a resistor (100 kΩ), a capacitor (220 nF), and a coil functioning as an inductor. The sample is placed at the centre of the coil. A DC bias (#7) is applied to the variable capacitor through the resistor to control its capacitance. The coil is a short (approximately 50 mm) bare copper wire that was shaped by being wrapped around a screwdriver. One end of the coil is connected to the copper substrate, while the other is connected to the tunable capacitor and the 220 nF capacitor. A multimeter is used to check connectivity. When one probe of the multimeter is placed on the copper board, and the other is placed at the centre of the tunable capacitor, the multimeter should indicate good continuity. The Q factor of this cavity is not necessarily large (20 - 30 in this project) because a high-Q resonator leads to a narrow bandwidth, which is not ideal for capturing the full range of the EPR signal.

A newly fabricated resonator must be tested using a vector network analyser (VNA). The circuit is connected to the DC bias and one port of the VNA through the stub tuner. The following two points are crucial:

- **The DC bias and stub tuner effectively control the resonant frequency.** Significant movement of the peaks on the VNA should be observed when adjusting these two components.

- **The correct mode is tuned to the resonant frequency of the sample.** A resonator typically exhibits multiple modes, but not all can effectively interact with samples. By inserting a metal wire into the coil, the peak around the microwave mode of the resonator should shift, confirming that it is the correct mode.

3.3.2 Lower Frequency Range

Most components have a specific operating frequency range that must be checked when switching to a lower frequency range. Among them, power splitters, circulators, and isolators have relatively narrow operating frequency ranges and require more attention.

Additionally, phase shifters do not work effectively at lower frequencies. The phase shifter's capability (measured in [degrees / GHz]) is proportional to the frequency. In such cases, an extra phase shifter is needed. An additional cable can sometimes help shift the phase to the desired position. However, since this phase shift is constant, cables of different lengths may need to be tested to achieve the correct phase.

A new coil is required. The equation determining the frequency of an LC circuit is:

$$f_{LC} = \frac{1}{2\pi\sqrt{LC}}$$

where C denotes the capacitance of the capacitor and L denotes the inductance of the coil. A higher inductance is necessary to achieve a lower frequency, which in turn requires a coil with a larger area. Typically, a multi-turn coil is employed for this purpose.

3.4 EPR Procedure

This section provides a detailed guide for operating the EPR spectrometer. The general steps are as follows: First, determine the microwave power and attenuation settings. Next, balance the spectrometer to achieve maximum sensitivity. After balancing, proceed with measuring the

signals. Finally, verify the measured signals to ensure accurate and reliable results.

3.4.1 Preparation

The signal generator is turned on to supply a constant microwave signal. At this stage, the frequency is set to the resonant frequency, and the power is determined.

The mixers require a minimum microwave power of 7 dBm at their LO port. A spectrum analyser (Signal Hound SA44B) is connected before the LO port to check. The power of the signal generator is increased until it reaches the requirement.

Next, the attenuator on the RF branch is adjusted to control the microwave power entering the resonator, referred to as the input power. A spectrum analyser is connected between the isolator and the RF bridge to measure this power. In an experiment, different input powers are used to find the saturation power, such that a microwave power below saturation could be used. Too low an input power may result in a weak signal, while too high an input power can distort signals. This issue will be further discussed in Section 3.4.4.

The power supplies for the low-noise amplifiers (LNAs) are turned on at this stage.

3.4.2 Balancing

At the beginning of this step, the bandpass filter is disconnected from the mixer and connected to a spectrum analyser (as shown in blue in Figure 3.7). The spectrum analyser measures the reflected power from the cavity, which should be minimised to achieve balance. The attenuator and phase shifter on the balancing arm, the stub tuner, and the DC bias are adjusted to balance. Typically, the reflected microwave signal power at balance is around -35 dBm.

Balancing the spectrometer is required each time the resonant frequency changes, and the reflected microwave signal should remain consistent throughout the experiment.

Note that while ultra-low reflected microwave power may be achievable at certain frequencies,

it may not be at others. Therefore, it is better to compromise for consistency by balancing to a low enough power that all frequencies can reach.

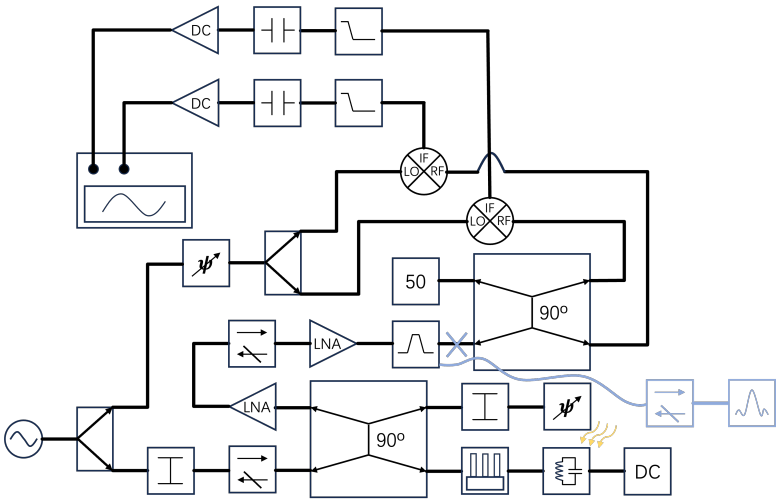


Figure 3.7: The internal structure of the EPR spectrometer when the spectrum analyser is connected. The cable linking the bandpass filter and the power splitter is disconnected (indicated by a blue cross). Instead, the spectrum analyser is connected to the bandpass filter via an isolator (both in blue).

3.4.3 Measurement

After balancing, return to the circuit configuration in Figure 3.5. Care must be taken not to disturb the spectrometer, as this could undo the balance physically.

Next, turn on the laser and start measuring. If no signal is visible, it is recommended to try slightly moving the sample, adjusting the phase shifter, and rebalancing the spectrometer. If the signal is still not visible, it may not exist at this frequency, and other frequencies should be tested. If no signals are detected within the possible frequency range, a new coil may be needed, or ultimately, the sample may not be able to emit an EPR signal.

When a signal is detected, it may appear on either oscilloscope channel. Adjusting the phase shifter can shift the signal entirely to one channel. At this point, the signal's amplitude (defined as the extremum value of the voltage) will be at its maximum on that channel, while the other channel should display a line close to zero voltage. Alternatively, the area under the curve on the other channel should be zero if noise is present. A detected signal is shown in Figure 3.8

as an example.



Figure 3.8: An example of a detected signal. The signal is present on channel 2 (in blue). Its characteristic feature is a sudden increase or decrease in voltage at $t = 0$ (indicated by the yellow arrow labelled "T"), followed by a gradual decay to the baseline. Channel 3 (in magenta) shows no signal and is close to zero voltage. An average of 32 times was used in this measurement.

Averaging is a critical technique for measuring signals with thermal noise. During the signal search stage, the oscilloscope should respond rapidly; thus, a smaller number of averages, typically 4, is used. However, more averages are required for capturing and storing signals accurately, with 64 averages being commonly applied. The criterion for determining sufficient averaging during the storing stage is that the signal displays minimal or no change as the number of averages increases. The same number of averages may not be sufficient for weaker signals to reveal their presence. Therefore, 32 averages at the searching stage and 512 averages at the storing stage are commonly used.

When measuring an EPR signal, a frequency range is scanned, including the frequency with the largest amplitude, along with at least three adjacent higher and three adjacent lower frequencies. Including these adjacent frequencies ensures that the largest amplitude is the global maximum instead of a local maximum. Due to the low Q-factors of our LC resonator, a scanning step size of 5 MHz is commonly used. A Gaussian fit is applied to the distribution of these seven amplitudes to determine a more accurate central frequency, which is then considered the transition frequency. Figure 3.9 shows an example of this process.

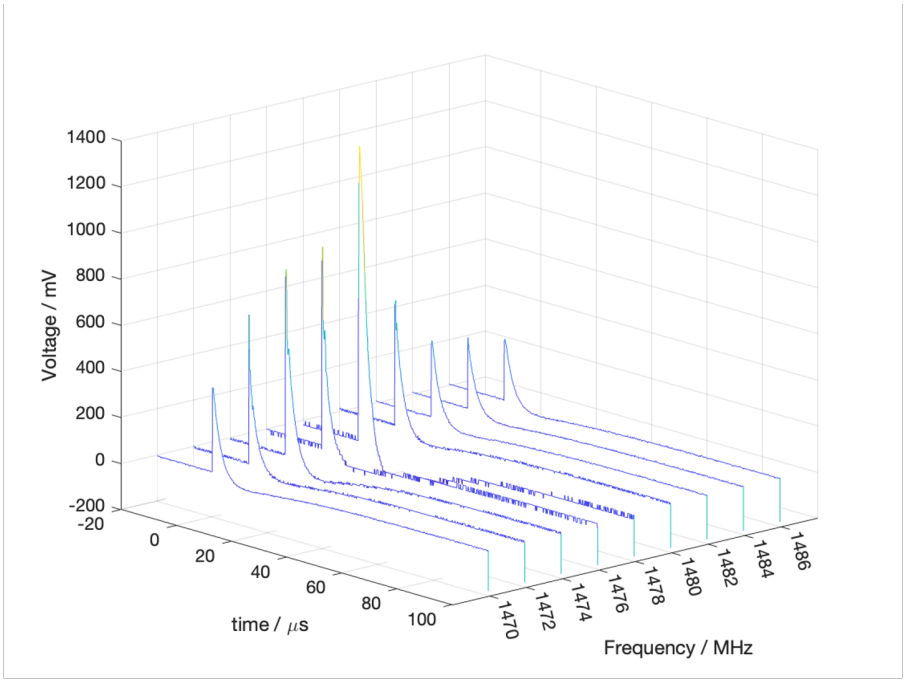


Figure 3.9: A waterfall plot of a group of signals. The colour and y-axis denote the voltage. The signal at 1478 MHz has the largest amplitude. Four adjacent signals at higher frequencies and four at lower frequencies are measured. A step size of 2 MHz is used because the signals are relatively strong with narrow bandwidth. This group of signals was measured on DAP:PTP.

3.4.4 Verification

Occasionally, noise that resembles the shape of EPR signals may be captured. This reproducible noise can originate from the power supply, the laser beam interacting with components in the LC resonator, vibrations of the samples, etc. Since this noise is not random, it cannot be suppressed by averaging. Two common methods for verifying the authenticity of EPR signals are:

- **Placing a magnet near the samples**: When a magnet is present, the Zeeman energy shift expressed in Equation 1.2 is added onto the zero-field splitting. In this scenario, the transition frequency no longer matches the resonance frequency, and the signal will disappear. This method provides a quick check but may not always be effective. Sometimes, the signal may partially disappear, distort, or even become stronger.

- **Removing the samples from the cavity**: This is the definitive method. If the signal disappears when the samples are removed, it can be confirmed as a real EPR signal.

For EPR signals mixed with reproducible noise, a baseline measuring technique is employed to cancel the noise. This technique measures the mixed signals first, then eliminates the signals using either of the methods above (preferably the second method) and measures the pure noise. The difference between these two measurement results will yield pure EPR signals.

Sometimes, the signals are mixed with a constant offset, which could be a voltage bias or very low-frequency noise. Adjusting the oscilloscope can cancel this bias.

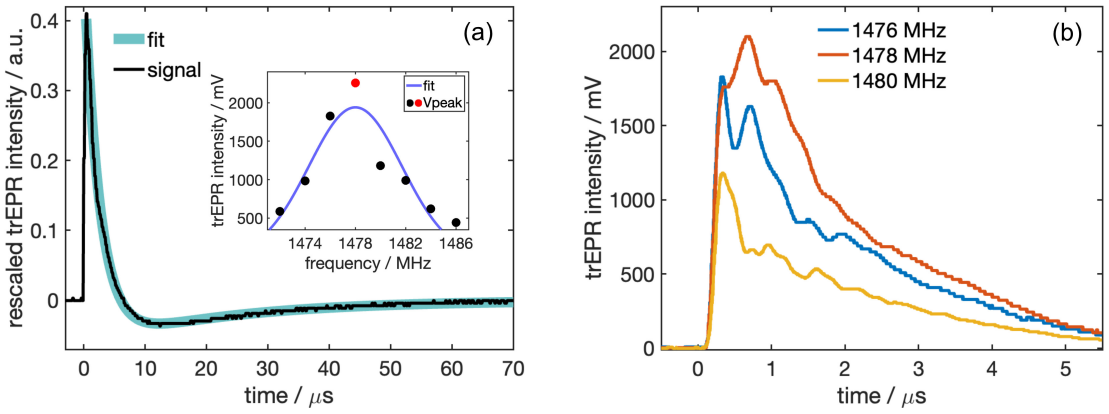
Power saturation should also be avoided. This phenomenon occurs when the input microwave power exceeds the spin system's amplification capacity. In this situation, the spin system cannot effectively absorb additional energy, and increasing the applied microwave power does not lead to a proportional increase in signal intensity. For example, in Figure 3.11, power saturation begins from -20 dBm, as indicated by the corresponding points deviating from the black line.

3.5 Results

3.5.1 DAP:PTP

Previous literature had investigated the electronic structures and spin dynamics of various molecular alternatives to Pc:PTP as masers [5]. A particularly promising candidate was 6,13-diazapentacene doped in para-terphenyl (DAP:PTP), which was postulated to mase through a population inversion between its photoexcited triplet sublevels, T_x and T_z [5]. The EPR experiment was conducted on DAP:PTP for the first time [6]. A small 0.01% DAP:PTP cylindrical crystal ($3 \times 1 \times 1$ mm dimensions) was excited at 620 nm with a pulse length of 10 ns and a repetition rate of 10 Hz.

The strongest ZF-trEPR signal was found at 1478 MHz (Figure 3.10(a)), where the signal was initially emissive for 7 μs before shifting to being absorptive for another 30 μs. The shape of the resonant signal at a shorter time is shown in Figure 3.10(b) while comparing it to two signals at adjacent frequencies. Since the experiments were conducted with a 2 MHz step size, the frequency of $T_x - T_z$ transition was determined to be $f_{T_x - T_z} = 1478 \pm 2$ MHz. Some oscillations



(a) (b)

Figure 3.10: (a) The EPR signal of DAP:PTP measured at 1478 MHz (black curve). This signal is rescaled with the peak voltage equal to the maximum population difference between T_z and T_x (0.41[5]). A bi-exponential fitting (green curve) was plotted to estimate the spin dynamics. Other measured peak voltages are plotted in the inset figure and fitted with a Gaussian curve. (b) A closer look at the peaks of the signal at 1478 MHz and its two adjacent signals. Reprinted from [6] under the terms of the Creative Commons CC-BY 4.0 license. Copyright 2023, John Wiley & Sons, Ltd.

can be seen for the resonant signal in Figure 3.10(b) between 0 and 1 μs. The oscillations are likely due to noise since they persist even at low microwave powers and do not change the frequency with microwave power.

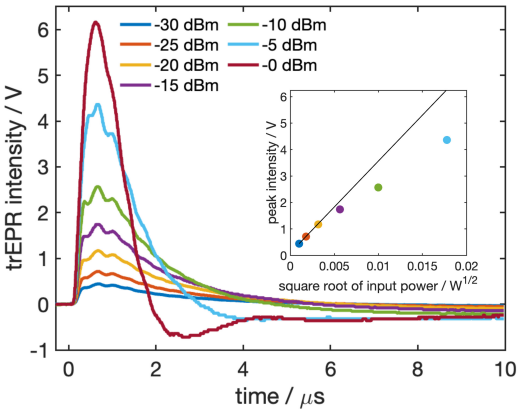


Figure 3.11: ZF-trEPR signals of DAP:PTP collected under the same experimental conditions as in Figure 3.10, but with different input microwave powers. Oscillations occur at all microwave powers. The inset plot illustrates the relation between peak trEPR voltage and the square root of the input microwave power (in watts). The proportional relation is violated when the input power is higher than -20 dBm, which indicates the onset of power saturation. Reprinted from [6] under the terms of the Creative Commons CC-BY 4.0 license. Copyright 2023, John Wiley & Sons, Ltd.

The triplet spin dynamics can be elucidated by simulating the observed ZF-trEPR signals,

which are related to the populations of the triplet sublevels. Since the frequency of the laser pump corresponds to the transition between T_x and T_z, the third sublevel T_y, is assumed to be negligible. This assumption is verified to be accurate in Section 4.4.1. The voltages of the ZF-trEPR signals are then proportional to the population difference between T_x and T_z, denoted as $N_x(t) - N_z(t)$. The time evolution of N_x and N_z can be represented by a group of differential equations:

$$\begin{bmatrix} \dot{N}_x(t) \\ \dot{N}_z(t) \end{bmatrix} = \begin{bmatrix} -w_{xz} - k_x & w_{xz} \\ w_{xz} & -w_{xz} - k_z \end{bmatrix} \begin{bmatrix} N_x(t) \\ N_z(t) \end{bmatrix} \tag{3.14}$$

where w_{xz} is the spin-lattice relaxation rate between T_x and T_z, k_x and k_z are the depopulation rates of these two sublevels [57]. The upward and downward spin-lattice relaxation rates are assumed to be the same at room temperature since they are related by the Boltzmann factor [17], as discussed in Section 3.2.1.

The signal at 1478 MHz was rescaled such that the maximum amplitude was 0.41 (Figure 3.10(a)), corresponding to the maximum population difference (*i.e.* $N_x(0) - N_z(0) = 0.41$ with $N_x(0) + N_y(0) + N_z(0) = 1$) between those two sublevels [5]. A bi-exponential fitting was then applied to the signal as in Equation 3.15, to find the relaxation rates:

$$N_x(t) - N_z(t) = A\exp(\alpha_- t) + B\exp(\alpha_+ t) \tag{3.15}$$

$$\alpha_\pm = -(w_{xz} + k_{avg}) \pm \sqrt{w_{xz}^2 + (\Delta k)^2} \tag{3.16}$$

where α_- and α_+ are two eigenvalues of the coefficient matrix in Equation 3.14. $k_{avg} = (k_x + k_z)/2$ and $\Delta k = (k_x - k_z)/2$. The simulated curve is shown as the green curve in Figure 3.10(a), with the fitted parameters being $A = 0.547 \pm 0.003$, $B = -0.066 \pm 0.005$, $\alpha_- = (-3.93 \pm 0.06) \times 10^5\ s^{-1}$ and $\alpha_+ = (-0.459 \pm 0.017) \times 10^5\ s^{-1}$.

According to Equation 3.16, the combination of two depopulation rates gives

$$-\frac{1}{2}(\alpha_- + \alpha_+) = w_{xz} + \frac{k_x + k_z}{2} \tag{3.17}$$

which corresponds to a decay rate of $0.2 \times 10^6\ s^{-1}$ (decay time 4.6 μs). This gives an upper limit on the decay time of the spins, as it is impossible to separate the spin-lattice relaxation and depopulating rates from this simulation without knowing them independently.

3.5.2 DAT, TrAT1 and TrAT2 doped 1-TNB

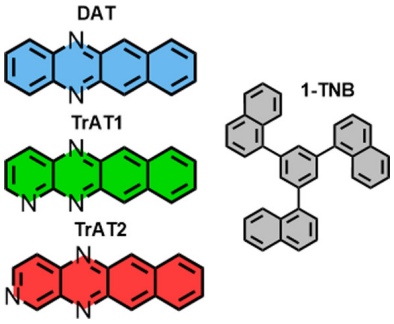


Figure 3.12: Structures of 1,3,5-Tri(1-naphthyl)benzene (1TNB) Host Molecule and N-Substituted Tetracene Derivatives. Reprinted from [7] under the terms of the Creative Commons CC-BY 4.0 license. Copyright 2023, American Chemical Society.

Three nitrogen-substituted tetracene derivatives, 5,12-triazatetracene (DAT) and its nitrogen-substituted variants, 1,5,12-triazatetracene (TrAT1) and 2,5,12-triazatetracene (TrAT2), were synthesized [7]. DAT is a known spin-polarized molecule. By introducing additional nitrogen atoms at specific positions, TrAT1 and TrAT2 were created. These substitutions modulate the optical band gap and triplet formation dynamics, both of which affect the efficiency of triplet state generation upon photoexcitation. This allowed us to explore how the number and position of nitrogen atoms influence key properties such as triplet sublevel populations, spin-lattice relaxation rates, decay rates, and zero-field splitting. These parameters determine how effectively each molecule can serve as a maser gain medium [7]. Their molecular structures are depicted in Figure 3.12. ZF-trEPR experiments were performed to investigate the transitions between triplet sublevels $T_x - T_z$, $T_y - T_z$, and $T_x - T_y$ in these materials. Although simulations had been previously carried out on these materials, this marked the first application of time-resolved EPR on them. These experiments utilised an LC resonator, specifically designed to resonate within each molecule's transition frequency band. To identify the frequency that yielded the most intense signal, the measurements were performed incrementally in steps of 5 MHz, closely surrounding the predicted transition frequencies.

The strongest $T_x - T_z$ signals were observed at 1765 MHz for DAT:1-TNB, and at 1755 MHz for both TrAT1:1-TNB and TrAT2:1-TNB. These transitions exhibited relatively broad line widths, with full-width half-maximum values exceeding 40 MHz.

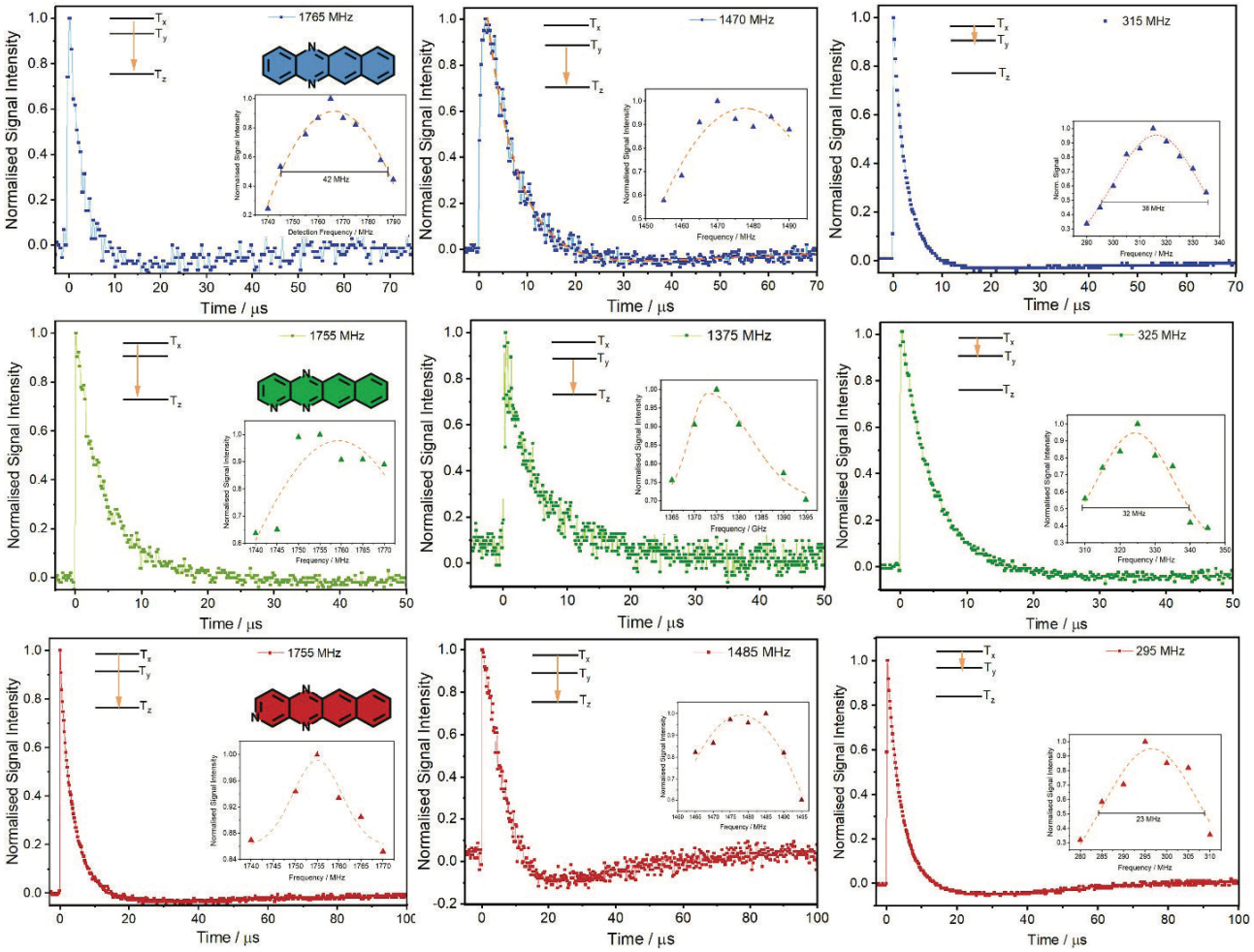


Figure 3.13: The captured most intense ZF-trEPR signals for DAT:1-TNB (blue), TrAT1:1-TNB (green) and TrAT2:1-TNB (red). Other measured peak voltages are shown in the insert figure. Reprinted from [7] under the terms of the Creative Commons CC-BY 4.0 license. Copyright 2023, American Chemical Society.

Figure 3.13 lists the most intense signals for all transitions and materials. These signals are used to calculate the spintronic parameters by being fitted into the following rate equations.

$$\begin{bmatrix} \dot{N}_x(t) \\ \dot{N}_y(t) \\ \dot{N}_z(t) \end{bmatrix} = \begin{bmatrix} -w_{xy} - w_{xz} - k_x & w_{xy} & w_{xz} \\ w_{yx} & -w_{yx} - w_{yz} - k_y & w_{yz} \\ w_{zx} & w_{zy} & -w_{zx} - w_{zy} - k_z \end{bmatrix} \begin{bmatrix} N_x(t) \\ N_y(t) \\ N_z(t) \end{bmatrix} \tag{3.18}$$

where N_i is the initial population on the i-th energy level, k_i is the decay rate from the i-th

energy level to the singlet ground state S_0, and $w_{ij} = w_{ji}$ are the spin-lattice relaxation rates between the i-th and j-th energy levels. The results are listed in Table 3.1. Fitted values correspond to R-squared values of >0.96, indicating good fitting results [7].

name	k_x	k_y	k_z	w_{xz}	w_{yz}	w_{xy}
DAT:1-TNB	7.43 ± 0.74	1.4 ± 0.04	0.74 ± 0.30	5.45 ± 2.0	16.9 ± 6.2	16.3 ± 2.9
TrAT1:1-TNB	1.23 ± 0.23	0.83 ± 0.21	1.11 ± 0.25	7.02 ± 0.24	13.4 ± 0.77	5.39 ± 0.32
TrAT2:1-TNB	4.17 ± 0.85	2.37 ± 0.61	1.04 ± 0.37	4.69 ± 2.03	8.62 ± 3.42	12.9 ± 4.56

Table 3.1: Spintronic parameters on DAT:1-TNB, TrAT1:1-TNB, and TrAT2:1-TNB. These parameters were derived by fitting each transition's most intense ZF-trEPR signals to the rate equations.

TrAT1:1-TNB showed relatively smaller ω_{xz} and ω_{xy} values, indicating slower redistribution of the T_x population. This slower redistribution may help retain the population in the upper spin level (T_x) for a longer time, which can support CW maser operation. In comparison, TrAT2:1-TNB exhibited intermediate relaxation behavior, with a relatively small ω_{xz} but a large ω_{xy}. DAT:1-TNB showed the highest values for spin-lattice relaxation, suggesting faster population exchange.

Regarding triplet decay rates, TrAT1:1-TNB had the lowest κ_x ($\approx 1.2 \times 10^4 s^{-1}$), suggesting a longer lifetime of the T_x population, which is favorable for maintaining population inversion—a key condition for CW masing. TrAT2:1-TNB showed a moderate κ_x, while DAT:1-TNB exhibited the highest decay rate.

3.6 Conclusion

In this chapter, zero-field time-resolved electron paramagnetic resonance spectroscopy was introduced and applied as a powerful method to characterize photoexcited triplet states in potential maser gain materials. Theoretical principles, such as spin-lattice and spin-spin relaxation, were outlined, followed by a detailed discussion on the rate equations used to describe the population dynamics within the triplet sublevels. The instrumentation section provided a step-by-step guide of the EPR spectrometer design, with an emphasis on achieving impedance matching and

signal detection through I-Q homodyne detection. The workflow covered the preparation, balancing, measurement, and verification stages essential for reliable data acquisition.

Experimental results were presented for DAP:PTP, DAT:1-TNB, TrAT1:1-TNB, and TrAT2:1-TNB. For each material, EPR signals corresponding to transitions between triplet sublevels were observed and analyzed. By fitting these signals to the rate equations, key parameters such as spin-lattice relaxation and depopulation rates were extracted. These rates are central to evaluating maser performance, particularly for estimating maser threshold and coherence times.

In summary, ZF-trEPR spectroscopy proves to be a practical and informative tool in identifying and characterizing maser gain materials. Its ability to quantify dynamic parameters from quick experiments makes it a valuable technique in the broader context of maser development. The insights gained here directly support the modeling and optimization of maser operation, which will be further explored in the following chapters.

Chapter 4

Simulation of Maser Dynamics

4.1 Introduction

Alongside maser experiments, corresponding simulations are commonly conducted [24, 6, 9, 63], where time-dependent partial differential equations are solved to simulate the maser behaviours and outputs (hereafter generally referred to as maser dynamics). Except for providing a more comprehensive understanding of the theory behind masers, these simulations help predict the performance of a new maser and reveal quantum quantities that are not directly measurable, such as spin-spin coherence and spin-photon coherence [24]. The parameters used in the simulations are obtained from other characterisation experiments [23]. For example, zero-field time-resolved electron paramagnetic resonance (ZF-trEPR) spectroscopy, introduced in Chapter 3, provides the spin-lattice relaxation rates and depopulation rates.

This chapter starts with the theory describing the maser system in Section.4.2, and then introduces the classical simulation methods. These methods are inefficient and inadequate for models more complicated than the two-level maser model, so the quantum-cumulant method is needed. Then an exploration of the Quantum-Cumulant method is presented in Section.4.3, which utilises the scientific programming language *Julia* and its quantum optics analysis package *QuantumCumulant.jl*. The outcomes of these simulations are presented in Section 4.4 to demonstrate the capabilities and advantages of using the Julia method. The *Julia* code was

initially built by Wu et al. [9]. I debugged and enhanced the code and extended its application to more cases.

4.2 Collective Effect: Tavis-Cummings Model

The Tavis-Cummings model [64] plays a crucial role in quantum optics as it provides a theoretical framework for describing an ensemble of identical spin-$\frac{1}{2}$ particles interacting with a quantized electromagnetic field. When combined with the master equation with Lindblad form, the Tavis-Cummings model enables a merely complete description of maser systems. This section begins by introducing the Jaynes-Cummings Hamiltonian and the Tavis-Cummings Hamiltonian.

4.2.1 Hamiltonian

The Jaynes-Tavis model describes a much simpler scenario: the interaction between a single photon and a single spin [65]. The Hamiltonian of this system is written as:

$$H_{\mathrm{JC}} = \hbar\omega_c a^\dagger a + \frac{1}{2}\hbar\omega_s\sigma_z + \hbar g_e(\sigma_+ a + \sigma_- a^\dagger) \tag{4.1}$$

where "JC" are the initials of "Jaynes-Cummings", and

- $\hbar\omega_c a^\dagger a$ is the photon energy term, with ω_c being the frequency of the cavity mode, and $a^\dagger$, a being the creation and annihilation operators of the photon, respectively,
- $\frac{1}{2}\hbar\omega_s\sigma_z$ is the spin energy term, with ω_s being the its transition frequency, and σ_z being the Pauli Z operator,
- $\hbar g_e(a^\dagger\sigma_- + a\sigma_+)$ describes the interaction energy between the photon and the spin, with g_e denoting the coupling strength, σ_- and σ_+ being the spin lowering and raising operators, respectively.

In the Jaynes-Cummings model, the spin requires a 2-dimensional Hilbert space. The status of photons is described using the Fock states, whose Hilbert space is, in principle, infinitely large. However, for practical calculation, the Hilbert space is often truncated to two dimensions, *i.e.*, $|0\rangle$ (the vacuum state) and $|1\rangle$ (the single-photon state) [66]. Therefore, a 4-dimensional Hilbert space is used for the entire system, corresponding to a 4-by-4 density matrix. The diagonal terms in this density matrix provide information on (a) the probability of finding one photon in the cavity or no photons and (b) the probabilities of the spin being in either the excited or ground state. The off-diagonal terms provide information on their coherence. In the Jaynes-Cummings model, these probabilities evolve over time, as demonstrated in Figure 4.1. Since the system is isolated from external influences, there is no damping effect; hence, the sum of the two probabilities shown in the figure remains constant at 1. This behaviour reflects the conservation of the total number of excitations within the system.

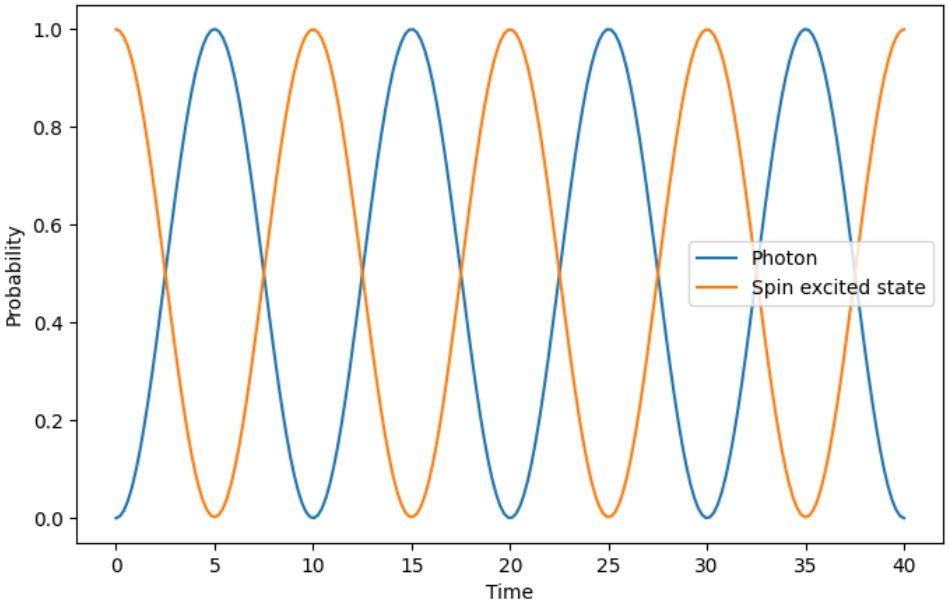


Figure 4.1: The time evolution of two quantum quantities: the probabilities of a photon existing in the cavity (blue) and the spin being in an excited state (orange). These two quantities oscillate with time but always add up to 1. These results were calculated using Equation 4.1 and a Python package named QuTiP [8]. This method is going to be introduced in Section 4.2.3.

When scaling up the system to include N identical spins interacting with N photons, the Jaynes-Cummings Hamiltonian is generalized to its collective form. This involves scaling the spin energy term and the coupling energy term linearly with N, as elaborated further below.

Due to the nature of the Fock state, increasing the number of photons adds more dimensions to the system, rather than simply taking the tensor product of individual states. It is important to note that this modification is valid under the mean-field approximation, where the separation between spins is much smaller than the wavelength of the cavity mode. This ensures that all spins experience a uniformly distributed light field and have the same coupling strength, *i.e.*, $g_e^1 = g_e^2 = ... = g_e$. This collective form of the Jaynes-Cummings Hamiltonian, *i.e.*, the Tavis-Cummings Hamiltonian, is written as:

$$H_{\mathrm{TC}} = \sum_j^N H_{\mathrm{JC}}^j = \hbar\omega_C a^\dagger a + \frac{1}{2}\hbar\omega_S \sum_j^N \sigma_z^j + \hbar g_e \sum_j^N (\sigma_+^j a + \sigma_-^j a^\dagger) \tag{4.2}$$

where operators σ_z^j, σ_+^j, and σ_-^j are simplified notation of Pauli operators specifically acting on the j-th spin, but in a abbreviated format. For example, considering the Pauli Z operator acting on the j-th spin, the complete notation is:

$$\mathbb{I}_1 \otimes \mathbb{I}_2 \otimes ... \otimes \sigma_z^j \otimes ... \otimes \mathbb{I}_N \otimes \mathbb{I}_L \tag{4.3}$$

Where $\mathbb{I}_i$ denotes the identity operator acting on the i-th spins and $\mathbb{I}_L$ is the identity operator acting on the light field. Similarly, the annihilation and creation operators, a and $a^\dagger$, are often expressed without explicitly showing the identity operators acting on the spins. For instance, the fully expanded form of the annihilation operator a is:

$$\mathbb{I}_1 \otimes \mathbb{I}_2 \otimes ... \otimes \mathbb{I}_N \otimes a \tag{4.4}$$

In the Tavis-Cummings model, each spin occupies a 2-dimensional Hilbert space. The combined Hilbert space for N spins is the tensor product of their individual spaces, resulting in a space of dimension 2^N. However, this rule does not apply when considering photons. Similar to the approach in the Jaynes-Cummings model, the Fock state space can be truncated to include only photon number states ranging from 0 to N. This truncation yields a Hilbert space of $N+1$ dimensions. The total Hilbert space of the system is then the tensor product of the spin Hilbert space and the truncated Fock state space, resulting in a combined space of dimension

$(N+1) \times 2^N$. The corresponding density matrix has the same dimensions. Without damping mechanisms, the system's time evolution exhibits dynamics similar to those depicted in Figure 4.1, with peak values approaching N.

For simplification, the collective spin operators acting on the collective spin states are defined as follows:

$$S_z = \sum_j^N \sigma_z^j \tag{4.5}$$

$$S_+ = \frac{1}{\sqrt{N}} \sum_j^N \sigma_+^j \tag{4.6}$$

$$S_- = \frac{1}{\sqrt{N}} \sum_j^N \sigma_-^j \tag{4.7}$$

Substituting them into the Tavis-Cummings Hamiltonian gives:

$$H_{\mathrm{TC}} = \hbar\omega_C a^\dagger a + \frac{1}{2}\hbar\omega_S S_z + \hbar g_N (S_+ a + S_- a^\dagger) \tag{4.8}$$

where $g_N = \sqrt{N} g_E$ represents the enhanced collective coupling strength between the N spins and N photons.

4.2.2 The Master Equation with Lindblad Form

In quantum mechanics, the Schrödinger equation is commonly employed to analyze the time evolution of a system. However, this method is not adequate for a maser system. The reason is that the Tavis-Cummings Hamiltonian is time-independent, so the Schrödinger equation with this Hamiltonian only captures unitary evolution [67], where the total number of excitations remains constant. This constraint does not accurately represent the behavior of a maser system, where damping procedures are involved. Therefore, the master equation with Lindblad form (hereafter referred to as the master equation) is used as an essential tool for evolving the density

matrix of a maser system. The equation is shown as follows [68]:

$$\dot{\rho} = (i\hbar)^{-1}[H, \rho] + \mathcal{L}[\rho] \tag{4.9}$$

Here $[A, B]$ is the commutator of operators A and B. The term $\mathcal{L}[\cdot]$ represents all Liouvillian superoperators, a kind of operators acting on quantum operators. These superoperators provide non-unitary operations on the density matrix, and each damping procedure has a corresponding superoperator.

For the simulation of our room-temperature solid-state maser, the following three dissipative processes need to be considered:

- **Cavity loss** refers to the loss of photons within a maser cavity, mainly due to two processes: absorption by the cavity walls and leakage of photons from the cavity. This loss is quantitatively described by the cavity photon decay rate, symbolised as $\kappa_c = \omega_c/Q$, where ω_c is the cavity's resonant frequency and Q is the quality factor of the cavity, indicating the efficiency of the cavity in retaining its photons.

- **Spin-lattice relaxation** is a form of noise arising from interactions between the spins in maser material and phonons in the surrounding lattice, as described by Siegman [10]. This interaction enables transitions between spin states. Within a simplified two-level system, these transitions are modelled using the raising operator (σ^+) and the lowering operator (σ^-). The rate at which spin-lattice relaxation occurs is denoted by γ.

- **Spin dephasing** refers to the loss of coherent phase alignment among spins in a quantum system. This dephasing leads to several detrimental effects: diminished amplification efficiency, reduced output power, a broader frequency spectrum, and a decreased signal-to-noise ratio. The spin dephasing rate is quantified as the inverse of the decoherence time, as $\kappa_s = 2/\mathcal{T}_2^*$.

The Liouvillian term in Equation 4.9 consists of the superoperators corresponding to these

three damping procedures. The explicit form of these superoperators is:

$$\mathcal{L}_{\text{cavity}}[\rho] = \frac{\kappa_c}{2}\mathcal{D}[a]\rho \tag{4.10}$$

$$\mathcal{L}_{\text{spin-lattice}}[\rho] = \frac{\gamma}{2}\sum_{j=1}^{N}\left(\mathcal{D}[\sigma_j^-]\rho + \mathcal{D}[\sigma_j^+]\rho\right) \tag{4.11}$$

$$\mathcal{L}_{\text{dephasing}}[\rho] = \frac{\kappa_s}{2}\sum_{j=1}^{N}\mathcal{D}[\sigma_j^z]\rho \tag{4.12}$$

where $\mathcal{D}[\mathcal{O}]\rho = 2\mathcal{O}\rho\mathcal{O}^\dagger - \mathcal{O}^\dagger\mathcal{O}\rho - \rho\mathcal{O}^\dagger\mathcal{O}$ is the Lindblad superoperator applied on a general quantum operator $\mathcal{O}$ and a density matrix ρ.

4.2.3 Solving the Master Equations

Before the *QuantumCumulants.jl* package came out, there are two methods widely used to solve the master equation and simulate the maser dynamics.

The direct method writes down the explicit form of every operator and superoperator, treats the master equation as a differential equation governing the density matrix, and evolves it over time using the Runge-Kutta method. The QuTiP package in Python applies this method [8], and it was also employed to simulate the time evolutions shown in Figure 4.1. However, the direct method proves impractical for solving maser dynamics, as constructing a complete density matrix dimension is not feasible. Recall that the number of rows or columns in the density matrix is $(N+1)\times 2^N$, where N is the number of spins at initial population inversion. In our maser system, N is typically in the order of 10^{14}. Creating a density matrix of this scale exceeds the capabilities of even the most advanced RAM on the market today.

One approach to simplification assumes that all two-level systems evolve simultaneously. During the system's evolution, tracking the state of each spin is unnecessary; instead, the focus should be placed on the collective state of the entire ensemble. Therefore, it is a reasonable approximation to assume that all spins are in identical status at all times. In this way, the tensor product of N density matrices, each of size 2×2, in the Tavis-Cummings model can

be reduced to a single 2×2 matrix, scaled by a factor of N. This approximation significantly reduces the number of dimensions in the density matrix.

However, in the case of a maser, the density matrix of the light field cannot be simplified using this technique because the Fock state of the entire light field is not represented as a tensor product of density matrices for individual photons. Even after applying this approximation, a density matrix with $N \times 2$ dimensions is required, which is still impractical to define. Therefore, further simplification is needed.

It was then realised that tracking the time evolution of every element in the density matrix is also unnecessary. Instead, focusing on the expected values of specific quantum quantities can be a more efficient and effective way. These expected values are fundamentally weighted sums of several matrix elements. The Heisenberg equation of motion helps apply this approach, expressed as:

$$\frac{\partial \langle \mathcal{O} \rangle}{\partial t} = \text{Trace}\left(\mathcal{O}\frac{\partial \rho}{\partial t}\right) \tag{4.13}$$

where $\mathcal{O}$ denotes a general quantum operator. This equation provides a general expression for the time derivative of any expected value, relating it to the time derivative of the density matrix. The time derivative of the density matrix is given by Equation 4.9, with the simplified Tavis-Cummings Hamiltonian described in Equation 4.8.

The quantum operator $\mathcal{O}$ must be chosen carefully. This operator should not commute with the Tavis-Cummings Hamiltonian; otherwise, the time derivative of the operator becomes zero, and equation 4.13 becomes trivial. In this simulation, the chosen operators are:

- Number of spins $a^\dagger a$: It refers to the average number of photons present in the microwave cavity mode of the maser.
- Spin-Photon Correlation $a^\dagger S_-$: It quantifies how the presence or excitation of a spin affects the number of photons, and vice versa. This correlation is essential for describing coherent coupling between collective spins and the electromagnetic field.

- Spin-spin correlation S_+S_-: It measures how different spins in the system are entangled with each other in terms of their quantum states. This quantity is maximal when spin population inversion is zero [24].

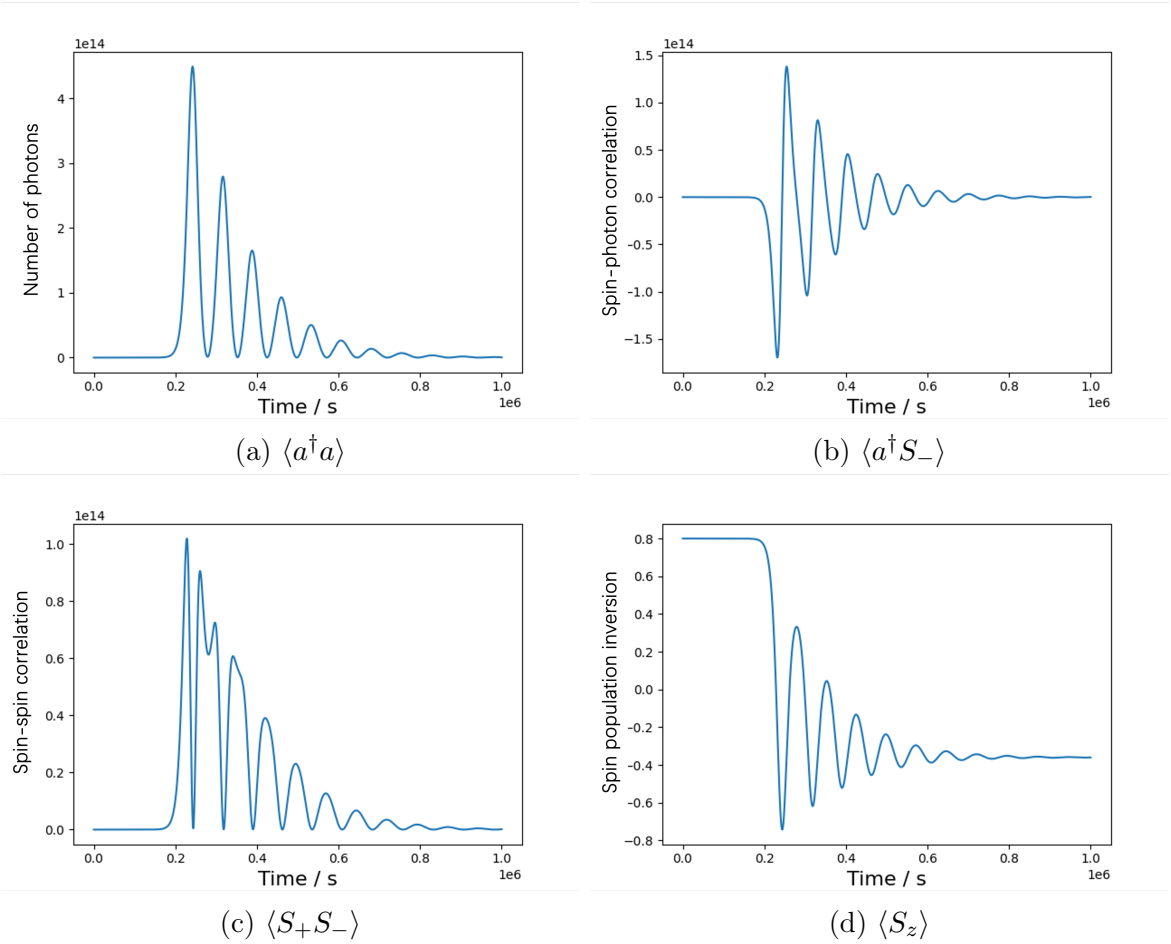
- Spin population inversion S_z: The difference in populations of the excited and ground states. When the population on T_x and T_z is denoted as N_x and N_z, the value of this operator is expressed as $N_x - N_z$.

These four operators transform the Lindblad equation into four coupled differential equations, listed below [24]:

$$\begin{aligned}
\frac{d}{dt}\langle a^\dagger a\rangle &= -\kappa_c\langle a^\dagger a\rangle + ig_e(\langle S_+a\rangle + \langle S_-a^\dagger\rangle)\\
\frac{d}{dt}\langle S_-a^\dagger\rangle &= -(\frac{\kappa_c}{2} + 2\kappa_s)\langle S_-a^\dagger\rangle + ig_e\cdot(\frac{\langle S_z\rangle + N}{2} + (1-\frac{1}{N})\langle S_+S_-\rangle + \langle a^\dagger a\rangle\langle S_z\rangle)\\
\frac{d}{dt}\langle S_+S_-\rangle &= -\kappa_s\cdot\langle S_+S_-\rangle + ig_e\langle S_z\rangle(\langle S_+a\rangle + \langle S_-a^\dagger\rangle)\\
\frac{d}{dt}\langle S_z\rangle &= -2ig_e(\langle S_+a\rangle + \langle S_-a^\dagger\rangle) + ig_e\langle S_z\rangle(\langle S_+a\rangle - \langle S_-a^\dagger\rangle)
\end{aligned} \tag{4.14}$$

With the initial expected values, this set of differential equations is solved using the Runge-Kutta method. The results, obtained from the function `solve_ivp` in the `scipy` library, are shown in Figure 4.2. The detailed derivation is elaborated in the works of Breeze et al.[24], Xu et al.[69], and Carmichael[32].

This method is commonly referred to as the coupled-differential-equation method. However, as shown in [69], this method requires term-by-term derivation, which is computationally time-consuming. This is particularly impractical for maser systems with more than 3 sublevels, additional damping processes, or fewer simplifications.



(a) $\langle a^\dagger a \rangle$ (b) $\langle a^\dagger S_- \rangle$

(c) $\langle S_+ S_- \rangle$ (d) $\langle S_z \rangle$

Figure 4.2: The time evolution of (a) the number of photons, (b) the spin-photon correlation, (c) the spin-spin correlation, and (d) the spin population inversion. These results were obtained using the `solve_ivp` function combined with the RK45 method. The initial values are $\langle a^\dagger a \rangle = 4300$, $\langle S_+ S_- \rangle = 0$, $\langle S_+ S_- \rangle = 0$, and $\langle S_z \rangle = 0.8$.

4.3 Quantum-Cumulant Method

4.3.1 Introduction

As discussed in the last section, the direct method is inadequate for simulating maser dynamics, and the coupled-differential-equation method lacks efficiency. In this section, the Quantum-Cumulant method is introduced, utilising the programming language *Julia* and the package *QuantumCumulants*.

Julia is a modern programming language focusing on scientific computing [70]. Its key features include:

- **High Performance**: *Julia* is designed for high speed and is often compared to C. It supports just-in-time (JIT) compilation, which compiles functions to native machine code at runtime and significantly improves the efficiency.

- **Ease of Use**: *Julia* supports dynamic typing, allowing variable types to change over time. It also allows the use of Greek letters as variable names, which is particularly useful in scientific contexts. Greek letters can be typed by entering the backslashed LaTeX symbol name, followed by pressing the `tab` key.

Similar to Python, *Julia* programs also have a structure of a main program and additional packages with a filename extension as ".ji". *QuantumCumulants.ji* is one of them, specifically developed for analyzing large systems in quantum optics [71]. This package utilises the cumulant expansion method to derive the coupled differential equations (similar to 4.14 and truncates these equations at a predetermined accuracy level before solving them. This capability makes *QuantumCumulants.jl* highly effective in handling complex systems.

The cumulant expansion method is a mathematical method commonly used in statistical mechanics [72]. This method expands the expected values of higher-order operator products in terms of products of lower-order expectation values, mathematically expressed as [71]:

$$\langle X_1 X_2 \dots X_n \rangle_c = \sum_{p \in P(I)} (|p|-1)!(-1)^{|p|-1} \prod_{B \in p} \langle \prod_{i \in B} X_i \rangle \tag{4.15}$$

This formula represents the cumulant expression of the product of n quantum operators $X_1, X_2, \dots, X_n$, where $P(I)$ denotes the set of all partitions of the set I, and $|p|$ is the number of blocks in the partition p. Each block B within the partition p contains a subset of the operators, and $\langle \prod_{i \in B} X_i \rangle$ represents the expectation value of the product of operators within block B.

4.3.2 Workflow

In this section, a general workflow for building models of masers using the quantum-cumulant method is presented, which includes defining the model, constructing the equations, and solving

the equations. In these models, it is assumed that the masers work in pulses and the population inversion is built instantly at the beginning. The symbols "`<description-of-code>`" denote the corresponding code that follows each description text. Note that "type" is a fundamental construct in Julia. Like "class" in Python, "type" defines the structure, behaviour, and operations that can be performed on data.

Defining the Model

Before diving into computations, it is essential to specify the involved Hilbert spaces. In a maser, the light field is represented by a Fock state, and the collection of spins is represented by the tensor product of N two-level systems. Given the capabilities of the *QuantumCumulants.jl* package on handling complex systems, the multiple sublevels in the maser gain material are no longer simplified as a two-level system. Instead, the exact number of sublevels is specified using the type `NLevelSpace`. The code for defining the Hamiltonian of the entire system is:

Listing 4.1: Defining Hilbert spaces

```
hc = FockSpace(:cavity)
ha = NLevelSpace(:atom, <number-of-levels>)
h = hc⊗ha
```

Where the symbol ⊗ (\otimes) denotes the tensor product of two Hilbert spaces.

Next, classical constants for spintronic parameters are defined, often denoted by Greek letters to align with conventional representations in other papers. The corresponding code is:

Listing 4.2: Defining classical constants

```
@cnumbers <spintronic-parameters>
```

Next, the quantum operators are defined. Two kinds of operators are used in this simulation: (a) creation and annihilation operators for the light field, and (b) Pauli operators for spins. In the *QuantumCumulants.jl* package, the annihilation operator is defined as the type `Destroy`, and the creation operator is represented as its Hermitian transpose. The type `Transition` represents

the Pauli operators, and it is defined using syntax `Transition(h, :σ, α, β)`. It defines an operator σ on the Hilbert space h that facilitates the transition from energy level α to level β. Especially, when $\alpha = \beta = j$, this operator measures the population on the j-th energy level. The type `IndexedOperator` indicates that this Pauli operator will act on the i-th spin. The code is:

Listing 4.3: Defining quantum operators

```
@qnumbers a::Destroy(h)
σ(α, β, i) = IndexedOperator(Transition(h, :σ, α, β), i)
```

Given that the model includes N spins, indexing is crucial. The code `i = Index(h, :i, N, h_a)` is used to define an index. This code assigns a label i to the index within the Hilbert space h, sets its upper bound to N, and links it to the specified Hilbert space h_a. Here is a code example of defining 4 indexes:

Listing 4.4: Defining the indexes

```
i = Index(h, :i, N, ha)
j = Index(h, :j, N, ha)
k = Index(h, :k, N, ha)
l = Index(h, :l, N, ha)
```

In the Tavis-Cummings model, the Hamiltonian is defined as a collection of spins and photons. The syntax `∑((<function-with-index>), <index>)` indicates a summation of the function over the specified index. Note that Pauli-z operators are represented as $\sigma_{ii} - \sigma_{jj}$, where i and j are the indices of the two energy levels in a spin. In addition, the package does not provide a direct representation for σ_{11}; instead, σ_{11} is represented as $\mathbb{I} - \sigma_{22} - \sigma_{33} - ... - \sigma_{mm}$, where m is the total number of energy levels.

Listing 4.5: Defining Tavis-Cummings Hamiltonian

```
H = <cavity-frequency>*a'*a
    + 0.5*<transition-frequency>*∑((<Pauli-z-operator>),<index>)
    + gs*∑((<coupling-operators>), <index>)
```

Note that the photonic and spin energy terms can be neglected. This is because the total excitation is conserved, and these two terms sum up to a constant, which does not influence the dynamics.

In the *QuantumCumulants.jl* package, the term "jumps" refers to the damping procedures discussed in Section 4.2.2. A vector `J` is used to store the jump operators (the quantum operators that Lindblad superoperators act on), and a vector `rates` is used to store the corresponding decay rates. For example, to represent the cavity loss mechanism in Equation 4.10, the jump operator should be the annihilation operator a, and the corresponding rate is $\kappa_c/2$.

Listing 4.6: Defining jump operators and their rates

```
J = [<decay-operators>]
rates = [<decay-rates>]
```

Constructing the Equations

To construct the equations for the system, the following processes are performed.

The function `meanfield` derives a set of coupled-differential equations according to the Hamiltonian H, involving only the operators specified in the vector `ops`. Based on the author's experience, only the photon-number operator $a^\dagger a$ and all σ_{ii} operators, excluding $i = 1$, are needed in `ops`.

The function `cumulant_expansion` applies the cumulant-expansion method to each term in the equations, up to a predetermined `order=<truncation-level>`. The function `complete` finds the operators not included in `ops` and completes the coupled differential equations with these operators. This step usually increases the number of equations. The function `scale` applies the mean-field approximation discussed in Section.4.2.3. After these procedures, the number of equations equals the number of variables to be solved.

Listing 4.7: Constructing differential equations

```
ops = [a'*a, <all-σ_ii-excluding-11>]
eqs = meanfield(ops,H,J;rates=rates,order=<truncation-level>)
```

```
eqs_e = cumulant_expansion(eqs,<truncation-level>)
eqs_ec = complete(eqs_e)
eqs_esc = scale(eqs_ec)
```

After that, the constants involved in the equations need to be evaluated. Two vectors, `ps` and `p0`, are used to store the names of the constants and their corresponding values, respectively. By setting these vectors, all necessary constants are ensured to be evaluated and prepared for use in solving the equations. The code of this step is:

Listing 4.8: Evaluating constants

```
ps = [<names-of-the-constants>]
p0 = [<values-of-the-constants>]
```

4.3.3 Solving the Equations

Defining the initial conditions is an essential step in solving differential equations. In this context, the initial values of the variables are specified in a vector called `u0`, which contains as many elements as the number of equations. Most of these elements are zeros, but some variables, such as the initial number of photons (calculated by Planck's law) and initial population, should be properly assigned.

Listing 4.9: Defining initial conditions

```
u0 = zeros(ComplexF64, length(eqs_esc))
u0[<variable-number>] = <initial-value>
```

Next, specify the time step and the solving algorithm. In this step, "`RK4`" stands for the canonical Runge-Kutta Order 4 method. The equations, initial values, time steps, and parameters are wrapped into an `ODEProblem` and then solved.

Listing 4.10: Solving the equations

```
dt = <time-step>
alg = RK4()
prob = ODEProblem(sys,u0,(0.0,<end-time>),ps.=>p0)
```

```
sol = solve(prob, alg)
```

Finally, the expected values of quantum operators at every time step are retrieved from the solution by using the following code:

Listing 4.11: Retriving expected values

```
<expected-value-of-quantum-operator> = sol[<quantum-operator>]
```

4.4 Discussion

4.4.1 Maser Dynamics of Two-level and Three-level Pc:PTP Maser

The coupled-differential-equation method has demonstrated satisfactory accuracy in simulating the dynamics of the Pc:PTP maser [24]. The same simulation is conducted using the quantum-cumulant method. Recall that the third sublevel in the triplet state, T_y, has been previously ignored for simplification. To examine the effectiveness of this simplification, the maser dynamics are simulated both with (two-level maser) and without (three-level maser) the sublevel T_y in this section.

In these simulations, the initial population inversion is built at $t = 0$ as $P_1 : P_2 : P_3 = 0.76 : 0.16 : 0.08$ [23]. Only the populations of the triplet state sublevels T_x, T_y, and T_z are considered. The parameters are shown in Table B.1 in the Appendix. The details are shown below.

In a two-level maser, the sublevels T_z and T_x are denoted as 1 and 2, respectively. The following processes are considered:

- Cavity loss (a).
- Spin-lattice relaxation between T_x and T_y (σ_{12} and σ_{21}).
- Spin dephasing (σ_{22}).

In a three-level maser, the sublevels T_z, T_y, and T_x are denoted as 1, 2, and 3, respectively, and more processes must be considered:

- Cavity loss (a).
- Spin-lattice relaxation among T_x, T_y, and T_z (σ_{12}, σ_{21}, σ_{13}, σ_{31}, σ_{23}, and σ_{32}).
- Spin dephasing (σ_{33} and σ_{22}).

The maser dynamics can be analyzed regarding the number of photons, spin-photon correlation, spin-spin correlation, and inversion. The corresponding relations for these quantities are provided below:

Listing 4.12: Quantum operators

```
real.(sol[a'*a]) # number of photons
imag.(sol[a'*σ(1,2,1)])/1e7 # spin-photon correlation
real.(sol[σ(1,2,1)*σ(2,1,2)]) # spin-spin correlation
(real.(sol[σ(2,2,1)]).-0.5)*2 # inversion
```

The two results show a strong agreement when considering the number of photons and the population inversion. However, for the other two quantum quantities, while both results have the same frequency, they differ in amplitude. The two-level maser model (represented by the blue curves) consistently exhibits larger amplitudes. Despite these differences, it is important to note that the number of photons is the only measurable quantity. In this regard, both results are identical.

4.4.2 Error of Rotating-wave Approximation

The Rotating-Wave Approximation (RWA) is a simplification commonly used in quantum optics to analyze interacting quantum systems. It selectively omits the highly oscillatory terms $\sigma_+ a^\dagger$ (also the energy nonconserving terms) and $\sigma_- a$, retaining only $\sigma_+ a + \sigma_- a^\dagger$ in the coupling term

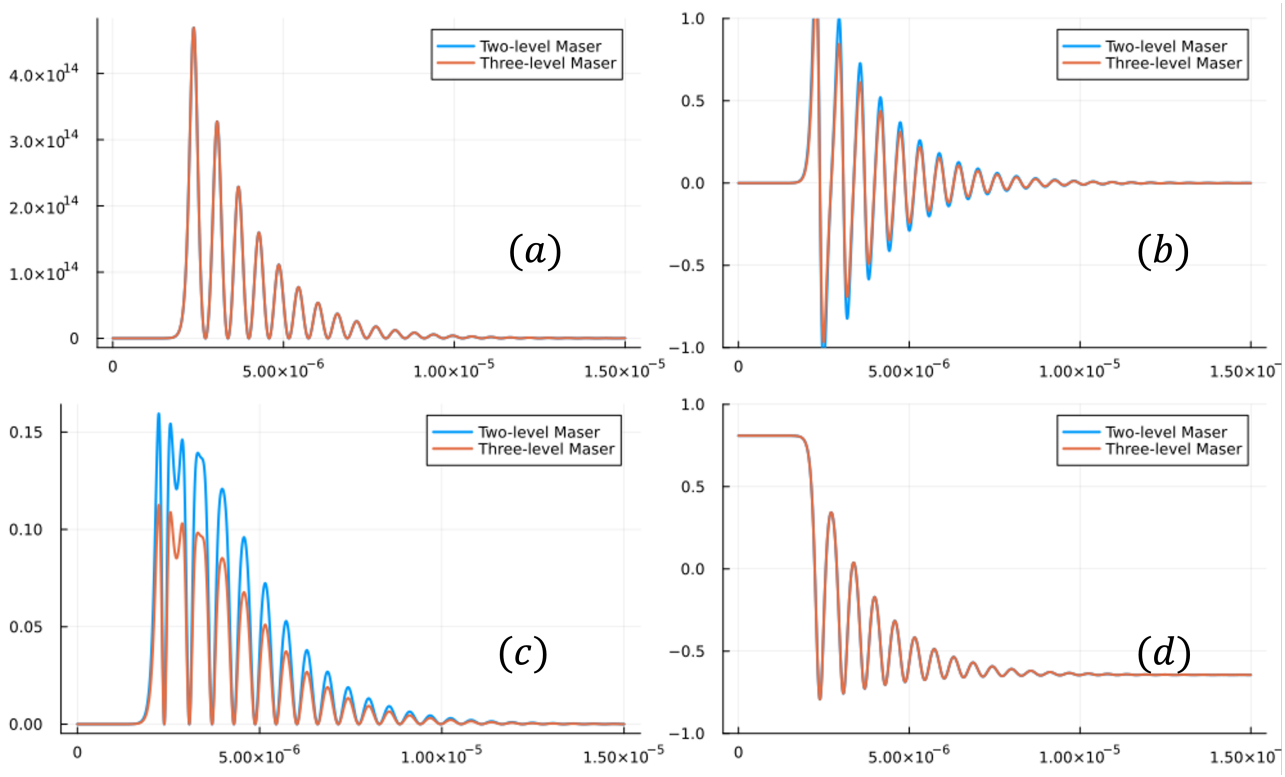


Figure 4.3: The simulation results of the maser dynamics, including (a) number of photons, (b) spin-photon correlation, (c) spin-spin correlation, and (d) inversion, are compared between the two-level and three-level maser models. The results obtained from the two-level maser are coloured blue, while those from the three-level maser are coloured orange. These results show differences in amplitudes between the two results.

of Equation 4.1. Without the RWA, the full expression of the Jaynes-Cummings Hamiltonian would include all these terms:

$$H_{\mathrm{JC}} = \hbar\omega_C a^\dagger a + \frac{1}{2}\hbar\omega_s\sigma_Z + \hbar g_e(\sigma_+ + \sigma_-)(a + a^\dagger) \tag{4.16}$$

This Hamiltonian is too complicated to be analysed using analytical methods.

The RWA is not always a good approximation. It requires the coupling strength between the atom and the field to be much smaller than their transition frequencies, *i.e.*,

$$g_e \ll \omega_C, \omega_s \tag{4.17}$$

In practical terms, the RWA is usually considered accurate when:

$$\frac{g_e}{\omega} \lesssim 10^{-3} \tag{4.18}$$

where ω is ω_C or ω_s. This ratio is approximately 7.6×10^{-4} on masers with Pc:PTP. In addition to weak coupling, the RWA also requires the system to be near resonance, meaning:

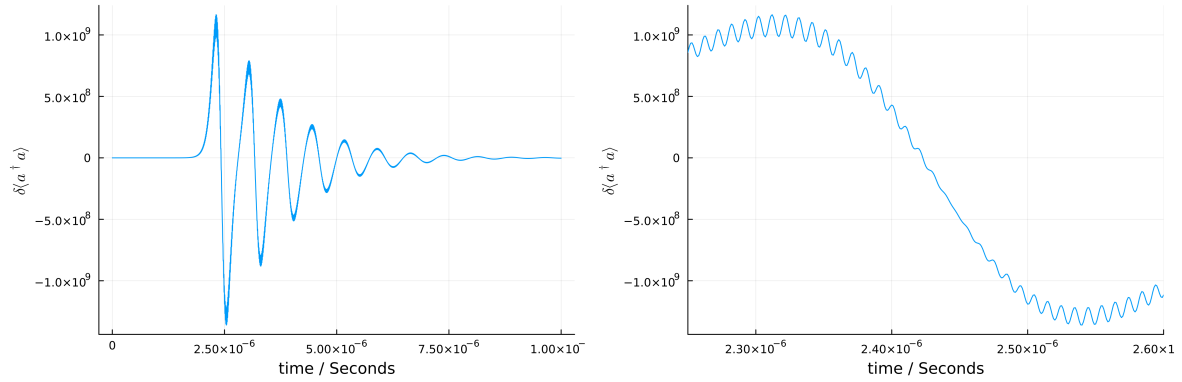
$$|\omega_C - \omega_s| \ll \omega_C + \omega_s \tag{4.19}$$

This ensures that the terms in the interaction Hamiltonian that oscillate very rapidly (with frequencies $\omega_C + \omega_s$) can be neglected. These terms do not contribute significantly to the dynamics over long times, because they average out to zero [73]. In a room-temperature solid-state maser, the second condition is well satisfied.

To validate the accuracy of the RWA, a simulation using the quantum-cumulant method is conducted on the two-level Pc:PTP maser model. The same settings from the previous section are used. The maser signal is simulated using Hamiltonian both with (Equation 4.1) and without (Equation 4.16) the RWA, and the difference between the solutions of the two simulations is calculated to quantify the computational error, denoted as $\delta\langle a^\dagger a\rangle$. The results are illustrated below:

The difference in the simulation results comprises two distinct oscillatory components. The larger oscillation matches the frequency of the maser signal, with its amplitude decaying over time. In contrast, the smaller oscillation occurs at a much higher frequency and maintains a relatively stable amplitude.

The peak amplitude of this difference is approximately 1.2×10^9, which is five orders of magnitude smaller than the maximum value of the maser signal. Therefore, the difference is considered



(a) $t \in [0, 10]\mu$s (b) $t \in [2.25, 2.6]\mu$s

Figure 4.4: (a) An overview of the computational error of the RWA over the time interval from 0 to 10 microseconds. There are oscillations present, with an initial sharp increase followed by oscillatory behaviour that gradually damps out. The oscillations exhibit a significant amplitude initially, which decreases over time. And (b) a detailed view focusing on the time range from 2.25 to 2.6 microseconds. This plot reveals a more stable, finer oscillatory pattern imposed on the larger oscillation.

negligible, confirming the validity of the RWA.

4.4.3 Maser Dynamics of NV Diamond Maser

The purpose of this model is to demonstrate the capability of the quantum-cumulant method, as the complexity of this 7-level system makes it analytically impractical [74]. Besides, instead of the initial population inversion, optical pumping and the intersystem crossing procedures are included in the simulation, for the study of steady states. This additional mechanism makes the simulation even more complicated.

A nitrogen-vacancy (NV) centre is a negatively charged point defect in the diamond lattice, where a nitrogen atom replaces a carbon atom and a vacancy is adjacent to it. The atomic structure of this defect is depicted in Figure 4.6(a). Diamonds with high concentrations of NV centres (hereafter referred to as NV diamonds) have been widely used as maser gain materials [1, 25, 27, 16]. One setup is shown in Figure 4.5.

The Jablonski diagram of NV centres is shown in Figure 4.6(b). Both the triplet states $^3A_2$ and ^3E have three projection numbers $m_s = 0, \pm 1$. The optical pumping process excites the electrons from the triplet ground state $^3A_2$ to the triplet excited state ^3E. Some of these electrons

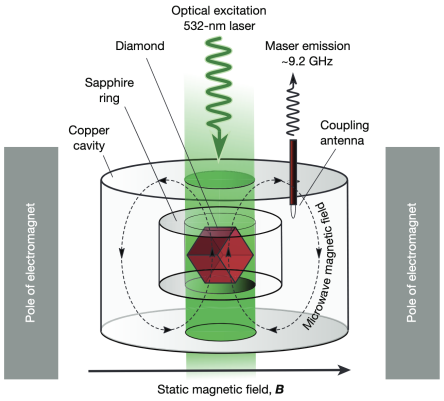


Figure 4.5: A setup of the NV^- diamond maser. The diamond is placed within a hollow cylindrical sapphire dielectric resonator, with both the sapphire resonator and the diamond enclosed in a copper cavity. The diamond is precisely oriented so that one of the NV⟨111⟩ axes is parallel to an externally applied static magnetic field of at least 102.5 mT. A continuous-wave 532 nm Nd:YAG laser is employed for optical pumping, thus polarizing electrons in the NV^- centers. Maser emission is extracted from the cavity using a microwave loop antenna coupled to a transmission line.

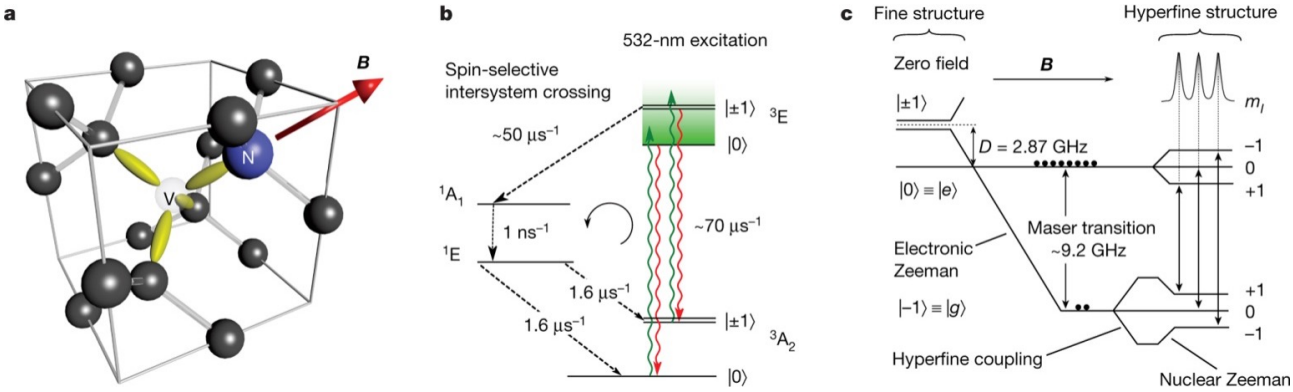


Figure 4.6: (a) The atomic structure of an NV centre in diamond. It consists of a nitrogen atom (blue) situated next to an empty lattice site (light grey) and surrounded by carbon atoms (black). (b) The Jablonski diagram of NV centres. An NV center has a triplet ground state $^3A_2$, a triplet excited state ^3E, and two singlet states $^1A_1$ and ^1E. The ground state has three projection numbers $m_s = 0, \pm 1$ along the NV quantization axis. (c) A magnified plot of the triplet ground state $^3A_2$. The Zeeman effect appears when a magnetic field is present, causing $|+\rangle$ and $|-\rangle$ to differ. Reprinted with permission from [1]. Copyright 2018, Springer Nature.

return to the ground state through spin-conserving radiative processes, while approximately 40% are transferred to the singlet state $^1A_1$ via a non-radiative spin-selective intersystem crossing mechanism. This is followed by a rapid decay to another singlet state ^1E, and then back to the $^3A_2$ state. In this final process, electrons predominantly concentrate on the $|0\rangle$ sublevel, resulting in spin polarization in the triplet ground state.

Unlike Pc:PTP, an external magnetic field is required for building population inversion in NV

centres. With the application of a magnetic field, the energy levels of the sublevels $|+1\rangle$ and $|-1\rangle$ diverge. When the magnetic field strength exceeds 102.5 mT and is oriented correctly, the $|-1\rangle$ state has lower energy than the $|0\rangle$ state, resulting in population inversion. In the maser experiment, a magnetic field is used to create an energy difference of approximately 9.2 GHz between the $|-1\rangle$ and $|0\rangle$ states.

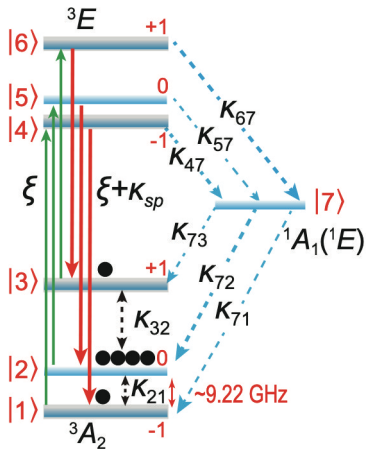


Figure 4.7: The Jablonski diagram of NV centres in the presence of a magnetic field is shown. For modelling purposes, each state and sublevel is assigned an index. The diagram also depicts the pumping and damping rates. Reprinted with permission from [9]. Copyright 2024, China Science Publishing & Media LTD.

To effectively analyze this system in the presence of a sufficient magnetic field, a 7-level system is considered, as illustrated in Figure 4.7. The sublevels $|+1\rangle$, $|0\rangle$, and $|-1\rangle$ in the triplet state $^3A_2$ are labelled as $|1\rangle$, $|2\rangle$, and $|3\rangle$, respectively. Similarly, the sublevels $|+1\rangle$, $|0\rangle$, and $|-1\rangle$ in the triplet state ^3E are labelled as $|4\rangle$, $|5\rangle$, and $|6\rangle$, respectively. For modelling purposes, it is not necessary to distinguish between the two singlet states, $^1A_1$ and ^1E; thus, they are collectively labelled as $|7\rangle$. The primary maser transition occurs between $|1\rangle$ and $|2\rangle$. The following damping and pumping terms are considered (the parameters are presented in Table B.2):

- Cavity loss (a).
- Spin-lattice relaxation:
  - Between $|1\rangle$ and $|2\rangle$ (σ_{12} and σ_{21}) at the rate of k_{21}.
  - Between $|2\rangle$ and $|3\rangle$ (σ_{23} and σ_{32}) at the rate of k_{32}.

- Spin dephasing:
  - From $|3\rangle$ to $|2\rangle$ (σ_{32}) at the rate of χ_{32}.
  - From $|2\rangle$ to $|1\rangle$ (σ_{21}) at the rate of χ_{21}.
- Intersystem crossing from ${}^3E$ to $|7\rangle$:
  - From $|6\rangle$ to $|7\rangle$ (σ_{67}) at the rate of k_{67}.
  - From $|5\rangle$ to $|7\rangle$ (σ_{57}) at the rate of k_{57}.
  - From $|4\rangle$ to $|7\rangle$ (σ_{47}) at the rate of k_{47}.
- Intersystem crossing from $|7\rangle$ to ${}^3A_2$:
  - From $|7\rangle$ to $|3\rangle$ (σ_{73}) at the rate of k_{73}.
  - From $|7\rangle$ to $|2\rangle$ (σ_{72}) at the rate of k_{72}.
  - From $|7\rangle$ to $|1\rangle$ (σ_{71}) at the rate of k_{71}.
- Optical pumping within these pairs of sublevels:
  - Between $|1\rangle$ and $|4\rangle$ (σ_{14} and σ_{41}).
  - Between $|2\rangle$ and $|5\rangle$ (σ_{25} and σ_{52}).
  - Between $|3\rangle$ and $|6\rangle$ (σ_{36} and σ_{63}).

  These processes all occur at the same rate, denoted by ξ.
- Spontaneous emission in these transitions:
  - From $|4\rangle$ to $|1\rangle$ (σ_{41}).
  - From $|5\rangle$ to $|2\rangle$ (σ_{52}).
  - From $|6\rangle$ to $|3\rangle$ (σ_{63}).

  These processes all occur at the same rate, denoted by k_{sp}.

The Hamiltonian for the system includes the photonic energy term and the spin energy terms only relevant to the states $|1\rangle$ and $|2\rangle$. Mathematically, it is expressed as:

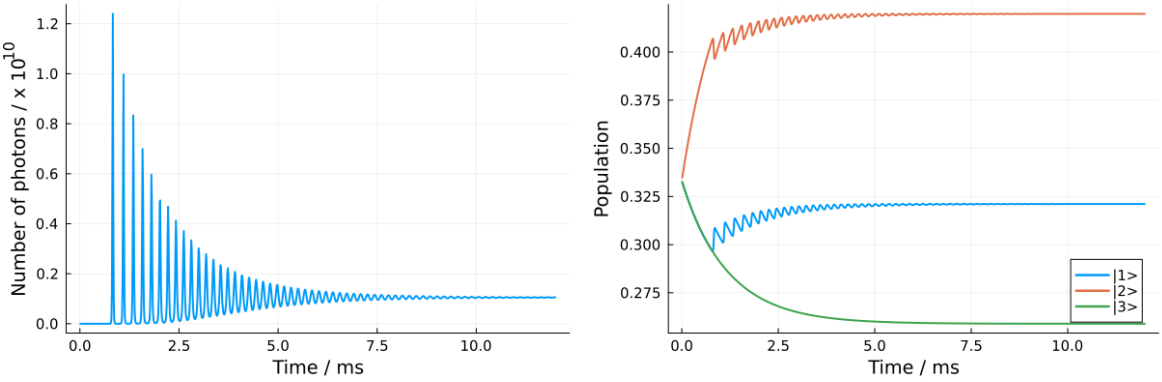
$$H_{\mathrm{NV}} = \omega_{ma} a^\dagger a + \omega_{12} \sum_k^N \left(\sigma_k^{22} - \sigma_k^{11}\right) + g_{12} \sum_k^N \left(a^\dagger \sigma_k^{12} + a\sigma_k^{21}\right) \tag{4.20}$$

where ω_{12} is the transition frequency between $|1\rangle$ and $|2\rangle$, and g_{12} is the coupling strength between the photonic field and the spin states.

The simulation results are analyzed below. The expected values of the following quantities are obtained from the solution:

```
real.(sol[a'*a]) # number of photons
real.(sol[σ(1,1)[1]]) # population in state |1>
real.(sol[σ(2,2)[1]]) # population in state |2>
real.(sol[σ(3,3)[1]]) # population in state |3>
```

Note that `σ(1,1)` is defined as 1 minus the sum of all other transition operators that have identical indices.



(a) Number of photons (b) Population of triplet groundstate $^3A_2$

Figure 4.8: The maser dynamics over 12 ms period for (a) photon number. Oscillation and exponential decay are observed simultaneously. (b) the population of sublevels $|1\rangle$ (blue), $|2\rangle$ (orange), and $|3\rangle$ (green).

Figure 4.8(a) shows the dynamics of the number of photons. The first peak (avalanche) arrives at 1 ms. The number of photons undergoes a series of oscillations that gradually decrease in amplitude over time. After around 8 milliseconds, the number of photons stabilizes at a relatively steady state at approximately 1.2×10^9.

The dynamics of the population of the triplet ground state are illustrated in Figure 4.8. The blue, orange, and green curves represent the sublevels $|1\rangle$, $|2\rangle$, and $|3\rangle$, respectively. Initially, there is a rapid increase in the population of $|1\rangle$, while the populations of $|2\rangle$ and $|3\rangle$ decrease exponentially. Following this phase, the populations of $|1\rangle$ and $|2\rangle$ exhibit a series of oscillations starting around 1 millisecond (the time when the avalanche of photon number arrives). The populations in $|1\rangle$ and $|2\rangle$ show an overall increasing trend, eventually stabilizing at approximately 0.32 and 0.42, respectively. In contrast, the population of $|3\rangle$ continues to decrease and eventually stabilizes at approximately 0.26.

By the time this thesis was completed, another related study had been published by Wen et al. [74]. In their work, the authors proposed simulating the same dynamics using rate equations, which are second-order coupled differential equations derived from the von Neumann equations of motion. Similar to the approach described previously, the NV^- centers were modeled as a seven-level system. However, rather than employing the quantum cumulant method, Wen et al. simplified the analysis by selecting only the non-zero elements of the density matrix. Specifically, they chose 13 relevant elements: seven diagonal terms representing populations of the seven energy levels, and six off-diagonal terms representing coherence between the states $|1\rangle$ and $|4\rangle$, $|2\rangle$ and $|5\rangle$, and $|3\rangle$ and $|6\rangle$. These rate equations were subsequently solved using the Runge-Kutta 23 method. A key advantage of this simplified rate-equation approach is its reduced computational cost, enabling a more detailed exploration of the relationship between the maser configuration and the masing threshold.

4.5 Conclusion

In this chapter, the simulation of maser dynamics has been explored in detail, starting from fundamental theoretical frameworks, the Jaynes-Cummings and Tavis-Cummings models, and progressing through classical methods to the Quantum-Cumulant method. Classical approaches, while effective for simulating simple two-level systems, become impractical when applied to room-temperature solid-state masers. This limitation arises because accurately simulating such

masers requires accounting for large numbers of photons and spins, exceeding the computational capabilities of modern computers. A more advanced computational method is required.

The Quantum-Cumulant method, implemented using the scientific programming language *Julia* and the package *QuantumCumulants.jl*, has been demonstrated as a powerful tool for analyzing maser dynamics. This method leverages cumulant expansions to efficiently solve complex quantum optical systems without significantly compromising accuracy, making it highly suitable for practical maser simulations.

Through simulations of the two-level and three-level Pc:PTP masers, the Quantum-Cumulant method successfully replicated known maser dynamics and validated common simplifications, such as neglecting specific sublevels or applying the RWA. It was shown that the RWA introduces minimal computational error, confirming its wide applicability in room-temperature solid-state maser research.

Furthermore, the simulation of a 7-level NV diamond maser system demonstrated the capabilities of the Quantum-Cumulant method in handling highly complex scenarios that involve many sublevels, additional damping processes, and optical pumping mechanisms. The results aligned well with previous work based on rate-equation approaches, providing confidence in the reliability and effectiveness of the method.

Overall, the Quantum-Cumulant method not only enhances computational efficiency but also significantly expands the scope of possible simulations in maser dynamics. This advancement provides valuable theoretical support for future experimental research and the development of new maser technologies.

Chapter 5

Conclusion

This PhD research has a central question: How can the performance of room-temperature solid-state maser devices be improved? In this thesis, several innovative approaches to advancing room-temperature solid-state masers have been thoroughly investigated.

The proposed piezoelectric maser cavity represents a new and promising alternative to conventional metal cavities. This cavity design has the potential to reduce cavity size by a factor of approximately 10^{-15}, which is critical for decreasing the magnetic mode volume and, as a result, increasing cooperativity. Simulation results indicate that magnetic coupling coefficients for the Rayleigh mode generally remain below 10^{-12}, whereas for the T_{00} torsional mode, these coefficients can increase up to 2.6×10^{-7} at an aspect ratio of 0.1. Initial simulations revealed certain limitations in the efficiency of magnetic energy conversion. However, the newly developed finite-element simulation tool, which goes beyond the limitations of the quasi-static approximation, significantly improves the accuracy of modeling magnetic fields generated by vibrating piezoelectric materials. Additionally, a hybrid simulation method employing more COMSOL modules and fewer weak-form equations was also developed. Although this approach simplified the coding process, it did not substantially enhance the results and therefore was not included in this thesis. Future research could explore additional vibration modes, such as standing waves. Overall, this simulation tool not only meets the immediate requirement of predicting the performance of piezoelectric maser cavities but also provides valuable insights for

broader applications in modeling energy propagation in antennas, resonators, and waveguides.

The application of zero-field time-resolved electron paramagnetic resonance (ZF-trEPR) spectroscopy demonstrated considerable advantages as an effective and reliable technique for quickly characterizing candidate maser gain materials. The detailed experimental studies presented have successfully identified several promising materials, such as diazapentacene-doped paraterphenyl (DAP) and two N-substituted tetracene derivatives (DAT and TrAT2). These materials exhibited notable ZF-trEPR signals, and subsequent experiments confirmed their masing capabilities. Experiments with the N-substituted tetracene derivatives systematically showed that carefully modifying compounds within the azatetracene family results in measurable improvements relevant to maser applications, potentially enabling continuous-wave, high-gain maser devices. Additionally, the analysis of spin dynamic parameters, including spin-lattice relaxation and spin depopulation rates, provided valuable insights into intrinsic material properties affecting maser performance. A lower spin-lattice relaxation rate, equivalent to a longer spin-lattice relaxation time, is preferable, as it enhances cooperativity. Thus, the ZF-trEPR spectroscopy method has proven essential not only for rapidly measuring spintronic parameters but also for guiding the selection of suitable materials for future investigations.

Complementing these experimental findings, the quantum-cumulant modeling method introduced in this thesis provides an accurate and computationally efficient means of simulating maser dynamics in complex quantum systems. By explicitly including key quantum correlations in master equations solved in Lindblad form, this method enabled detailed simulation of various maser configurations. These simulations validated simplifying assumptions, such as reducing the P:TP maser model from three levels to two levels and employing the rotating-wave approximation. Additionally, the successful simulation of a seven-level NV diamond maser demonstrated the capability and versatility of the quantum-cumulant approach in complicated systems. Such computational modeling offers significant advantages for predicting and optimizing maser behaviors, potentially reducing experimental effort.

Ultimately, this thesis establishes a solid foundation for future studies and technological development, paving the way toward robust, efficient, and practically deployable room-temperature

masers. Such devices have diverse applications, including precision frequency references, low-noise amplification, quantum computing, and advanced sensing technologies.

Appendix A

Properties of Some Piezoelectric Materials

These parameters are used in FEM simulations. They were obtained from Reference [34].

A.1 PZT-5H

PZT-5H is a type of lead zirconate titanate (PZT) piezoelectric ceramic material. It has uniaxial symmetry in its xy plane of material coordinate. The stiffness constants are

$$\underline{\underline{\underline{\underline{c}}}} = \begin{bmatrix} c_{11} & c_{12} & c_{13} & 0 & 0 & 0 \\ c_{12} & c_{11} & c_{13} & 0 & 0 & 0 \\ c_{13} & c_{13} & c_{33} & 0 & 0 & 0 \\ 0 & 0 & 0 & c_{44} & 0 & 0 \\ 0 & 0 & 0 & 0 & c_{44} & 0 \\ 0 & 0 & 0 & 0 & 0 & c_{66} \end{bmatrix} \tag{A.1}$$

where

$$c_{11} = 1.27205 \times 10^{11}$$

$$c_{33} = 1.17436 \times 10^{11}$$

$$c_{44} = 2.29885 \times 10^{10}$$

$$c_{12} = 8.02122 \times 10^{10}$$

$$c_{13} = 8.46702 \times 10^{10}$$

$$c_{66} = 2.34742 \times 10^{10}$$

whose units are [Newton/m^2(Pa)].

The piezoelectric stress constants are

$$\underline{\underline{e}} = \begin{bmatrix} 0 & 0 & 0 & 0 & e_{15} & 0 \\ 0 & 0 & 0 & e_{15} & 0 & 0 \\ e_{31} & e_{31} & e_{33} & 0 & 0 & 0 \end{bmatrix} \tag{A.2}$$

where

$$e_{15} = 17.0345$$

$$e_{31} = -6.62281$$

$$e_{33} = 23.2403$$

whose units are [Coulomb/m^2].

The relative dielectric constants are

$$\underline{\varepsilon}_r = \begin{bmatrix} \varepsilon_{r11} & 0 & 0 \\ 0 & \varepsilon_{r11} & 0 \\ 0 & 0 & \varepsilon_{r33} \end{bmatrix} \tag{A.3}$$

where

$$\varepsilon_{r11} = 1704.4$$

$$\varepsilon_{r33} = 1433.6$$

They are dimensionless quantities. In calculation, the vacuum permittivity $\varepsilon_0 = 8.854\times10^{-12}F\cdot m^{-1}$ is also needed as $\underline{\varepsilon} = \underline{\varepsilon}_r\varepsilon_0$

A.2 $LiNbO_3$

Lithium niobate ($LiNbO_3$) is famous for its strong electromechanical coupling. The stiffness constants are

$$\underline{\underline{\underline{\underline{c}}}} = \begin{bmatrix} c_{11} & c_{12} & c_{13} & c_{14} & 0 & 0 \\ c_{12} & c_{11} & c_{13} & -c_{14} & 0 & 0 \\ c_{13} & c_{13} & c_{33} & 0 & 0 & 0 \\ c_{14} & 0 & 0 & c_{44} & 0 & 0 \\ -c_{14} & 0 & 0 & 0 & c_{44} & c_{56} \\ 0 & 0 & 0 & 0 & c_{56} & c_{66} \end{bmatrix} \tag{A.4}$$

where

$$c_{11} = 2.02897 \times 10^{11}$$

$$c_{33} = 2.43075 \times 10^{11}$$

$$c_{44} = 5.99034 \times 10^{10}$$

$$c_{12} = 5.29177 \times 10^{10}$$

$$c_{13} = 7.49098 \times 10^{10}$$

$$c_{14} = 8.99874 \times 10^{10}$$

$$c_{66} = 7.48772 \times 10^{10}$$

$$c_{56} = 8.98526 \times 10^{9}$$

whose units are [Newton/m^2(Pa)].

The piezoelectric stress constants are

$$\underline{\underline{e}} = \begin{bmatrix} 0 & 0 & 0 & 0 & e_{15} & e_{16} \\ -e_{22} & e_{22} & 0 & e_{15} & 0 & 0 \\ e_{31} & e_{31} & e_{33} & 0 & 0 & 0 \end{bmatrix} \tag{A.5}$$

where

$$e_{15} = 3.69594$$

$$e_{16} = -2.53384$$

$$e_{22} = 2.53764$$

$$e_{31} = 0.193644$$

$$e_{33} = 1.30863$$

whose units are [Coulomb/m^2].

The relative dielectric constants are

$$\underline{\varepsilon}_r = \begin{bmatrix} \varepsilon_{r11} & 0 & 0 \\ 0 & \varepsilon_{r11} & 0 \\ 0 & 0 & \varepsilon_{r33} \end{bmatrix} \tag{A.6}$$

where

$$\varepsilon_{r11} = 43.6$$

$$\varepsilon_{r33} = 29.16$$

They are dimensionless quantities. In calculation, the vacuum permittivity $\varepsilon_0 = 8.854 \times 10^{-12} F \cdot$

m^{-1} is also needed as $\underline{\varepsilon} = \underline{\varepsilon}_r \varepsilon_0$

Appendix B

Spintronic Parameters

Spintronic parameters quantitatively describe the behaviour of spins in solid-state masers. These parameters are used in the simulation of zero-field time-resolved electron paramagnetic resonance and maser signals.

B.1 Pc:PTP

Symbols	Quantity	Description
$P_x : P_y : P_z$	0.76:0.16:0.08 [75]	spin polarization
ω	$2\pi \times 1.45$ GHz [2]	resonance frequency
N	7×10^{14} [24]	total number of excitation
k_x	28 kHz [23]	depopulation rate
k_x	6 kHz [23]	depopulation rate
k_x	2 kHz [23]	depopulation rate
k_c	$2\pi \times 0.18$ MHz [24]	cavity mode decay rate
k_s	$2\pi \times 0.11$ MHz [24]	spin dephasing rate
w_{xz}	11 kHz [23]	spin-lattice relaxation rate
w_{yz}	22 kHz [23]	spin-lattice relaxation rate
w_{xy}	4 kHz [23]	spin-lattice relaxation rate
g_s	$2\pi \times 0.042$ Hz [24]	single spin-photon coupling strength
g_e	$2\pi \times 1.1$ MHz [24]	ensemble spin–photon coupling strength

Table B.1: Spintronic parameters of pentacene-doped *para*-terphenyl (Pc:PTP)

B.2 Nitrogen-Vacancy Centres in Diamond

The parameters present below are all from Breeze's work [1].

Symbols	Quantity	Description
ω	$2\pi \times 9.22$ GHz	resonance frequency
N	4×10^{13}	total number of excitation
κ	1.88 MHz	photon damping rate
g_{21}	0.69 Hz	single spin-photon coupling strength
χ_{12}	4 MHz	spin dephasing rate
κ_{32}	208 Hz	spin-lattice relaxation rate
κ_{21}	208 Hz	spin-lattice relaxation rate
κ_{sp}	66 MHz	spontaneous emission rate
κ_{47}	53 MHz	intersystem crossing rate
κ_{67}	53 MHz	intersystem crossing rate
κ_{57}	7.9 MHz	intersystem crossing rate
κ_{73}	0.73 MHz	intersystem crossing rate
κ_{71}	0.73 MHz	intersystem crossing rate
κ_{72}	1 MHz	intersystem crossing rate

Table B.2: Spintronic parameters of nitrogen-Vacancy centres in diamond

Appendix C

Code of the Quantum Cumulant Method

C.1 Two-level Pc:PTP Maser

```
using QuantumCumulants
using Printf, Plots
using OrdinaryDiffEq, ModelingToolkit, DifferentialEquations
using Statistics
using DiffEqBase

# Hilbertspaces
@cnumbers N κc κs γgs ωc ωs
hc = FockSpace(:cavity)
ha = NLevelSpace(:atom, 2)
h = hc ⊗ha

# operators
@qnumbers a::Destroy(h)
σ(α, β, i) = IndexedOperator(Transition(h, :σ, α, β), i)

# indices
i = Index(h, :i, N, ha)
j = Index(h, :j, N, ha)
k = Index(h, :k, N, ha)
```

```
l = Index(h, :l, N, ha)

# Hamiltonian
H = ωc*a'*a + 0.5*ωs*∑((σ(2,2,k) - σ(1,1,k)),k) + gs*∑((a*σ(2,1,k) + a'*σ(1,2,k)), k)

# Jumps
J = [a, σ(2,1,k), σ(1,2,k), σ(2,2,k), 1 - σ(2,2,k)]
rates = [κc, γ, γ, κs, kx]

ops = [a'*a, σ(2,2,j), a'*σ(1,2,j), σ(1,2,j)*σ(2,1,l)]
eqs = meanfield(ops,H,J;rates=rates,order=2)
eqs_e = cumulant_expansion(eqs,2)
eqs_ec = complete(eqs_e)
eqs_esc = scale(eqs_ec)

@named sys = ODESystem(eqs_esc)
N_ = 7e14
κc_ = 2*pi*0.18e6
kx_ = 2*pi*2.8e4
κs_ = 2*pi*0.2e4
γ_ = 0
gs_ = 2*pi*0.042
ωc_ = 2*pi*1.4495e9
ωs_ = ωc

ps = [N, κc, κs, γ, gs, ωc, ωs, kx]
p0 = [N_, κc_, κs_, γ_, gs_, ωc_, ωs_, kx_]

u0 = zeros(ComplexF64, length(eqs_esc))
u0[1] = 4.3e3
u0[2] = 0.76 / (0.76 + 0.08)

dt = 1e-5
alg = RK4()
prob = ODEProblem(sys,u0,(0.0, 15e-6), ps.=>p0)
```

```
sol = solve(prob, alg, dtmax=1e-9)


t = sol.t
print(length(t))
n2 = real.(sol[a'*a])
as2 = imag.(sol[a'*σ(1,2,1)])/1e7
ss2 = real.(sol[σ(1,2,1)*σ(2,1,2)])
s2 = (real.(sol[σ(2,2,1)]).-0.5)*2
p1=plot(t, n2, lw = 4)
p2=plot(t, 2*as2, lw = 4)
p3=plot(t, ss2, lw = 4)
p4=plot(t, s2, ylims=[-1,1], lw = 4)
plot(p1, p2, p3, p4, layout=[2,2], size=(1400,800))
```

C.2 Sevel-level NV Diamond Maser

```
using QuantumCumulants
using OrdinaryDiffEq, SteadyStateDiffEq, ModelingToolkit
using Plots
using Printf

# Hilbertspaces
@cnumbers N ω12 ξksp k47 k57 k67 k73 k72 k71 k32 k23 k12 k21 χ12 χ13 ξ2
@cnumbers ωm g12 κnmth;
hc = FockSpace(:cavity) # Hilbert space of the resonator
hNV = NLevelSpace(:atom, 7)
h = hc ⊗hNV

# operators
@qnumbers a::Destroy(h)
σ(α,β,i) = IndexedOperator(Transition(h, :σ, α, β),i)

# indices
```

```
i = Index(h, :i, N, hNV)
j = Index(h, :j, N, hNV)
k = Index(h, :k, N, hNV)

# Hamiltonian
H = ωm*a'a + ω12*∑((σ(2,2,k) - σ(1,1,k)), k) + g12*∑((a'*σ(1,2,k)+a*σ(2,1,k)), k)

# Jump operators wth corresponding rates
J= [σ(4,1,k),σ(5,2,k),σ(6,3,k),σ(1,4,k),σ(2,5,k),σ(3,6,k),σ(7,4,k),σ(7,5,k),σ(7,6,k),σ(2,7,k),σ(3,7,k)
    σ(2,1,k),σ(2,3,k),σ(1,2,k),σ(3,2,k),σ(3,3,k),σ(2,2,k),a,a']
rates = [ξ,ξ,ξ,ξ2,ξ2,ξ2,k47,k57,k67,k72,k73,k71,k12,k32,k21,k23,χ13,χ12,(1.0+nmth)*κ,nmth*κ]

# build the ODE
ops = [a'*a, σ(2,2,j), σ(3,3,j), σ(4,4,j), σ(5,5,j), σ(6,6,j), σ(7,7,j)]
eqs = meanfield(ops,H,J;rates=rates, order=2)
eqs_c = complete(eqs, order=2)
eqs_sc = scale(eqs_c, h=2, order=2)

@named sys = ODESystem(eqs_sc)

hbar = 1.05457182e-34
kbT = 1.38e-23 * 300 # room temperature
hh = 6.62607015e-34

N_ = 4e13;
ω12_ = 2*pi*9.22e9
ksp_ = 6.6e7
k47_ = 5.3e7
k57_ = 7.9e6
k67_ = 5.3e7
k73_ = 7.3e5
k71_ = 7.3e5
k72_ = 1.0e6
k23_ = k32_ = 208
k12_ = k21_ = 208
```

```
χ12_= χ13_= 4e6;
λp = 532e-9;
σλp = 3.1e-21;
c = 2.99792458e8;
Ap = 1.76e-6;
l = 1.5e-3;
α= 2.3e3;
n1 = 1;
n2 = 2.42;
R =abs((n1*n2)/(n1+n2))^2;
P = 2;
ωm_ = 2*pi*9.22e9;
g12_ = 2*pi*0.11;
κ_ = 2*pi*0.3e6
nmth_ = 1.0/(exp(hbar*ωm_/kbT)-1)
ω12_ = ωm_ = 0

ξ_ = (λp*σλp)/(hh*c*Ap*l*α)*(1-exp(-l*α))*(1-R)*P
ξ2_ = 6.600132204100139e7

p0=[N_,ω12_, ξ_, ξ2_,ksp_,k47_,k57_,k67_,k73_,k72_,k71_,k32_,k23_,
    k12_,k21_, χ12_, χ13_,ωm_,g12_,κ_,nmth_];
ps=[N, ω12, ξ, ξ2,ksp, k47, k57, k67, k73, k72,
    k71, k32, k23, k12, k21, χ12, χ13, ωm, g12, κ, nmth]
u0 = zeros(ComplexF64, length(eqs_sc));
u0[1] = nmth_;
u0[2] =1/3;
u0[3] = 1/3

using OrdinaryDiffEq, ModelingToolkit;using SteadyStateDiffEq;
@named sys = ODESystem(eqs_sc);
prob0 = ODEProblem(sys,u0,(0.0, 12e-3), ps.=>p0, maxiters=2e8);
sol0 = solve(prob0, RK4(), reltol=1e-14);

t0 = sol0.t;
```

```
n = real.(sol0[a'*a]);
P20 = real(sol0[σ(2,2,1)]);
P30 = real(sol0[σ(3,3,1)]);
P40 = real(sol0[σ(4,4,1)]);

t0_ = []
n_ = []
P20_ = []
P30_ = []
P40_ = []
factor = 1000
for ind = 1:1025
    append!(t0_, t0[factor*ind])
    append!(n_, n[factor*ind])
    append!(P20_, P20[factor*ind])
    append!(P30_, P30[factor*ind])
    append!(P40_, P40[factor*ind])
end
length(n)

p1=plot(t0_,n_, lw = 1)
p2=plot(t0_,P20_, lw = 1)
p3=plot(t0_,P30_, lw = 1)
p4=plot(t0_,P40_, lw = 1)
plot(p1, p2, p3, p4, layout=(2,2), size=(1400,600))
```

Appendix D

Code of PyVisa

This code block extracts the results from oscilloscope's screen, reform them to the correct scale, and then plot them out.

```
from numpy.core.shape_base import block
import pyvisa
import time
import numpy as np
from struct import unpack
import matplotlib.pyplot as plt

#for windows 10, please download the NI-VISA driver from labview. The handmade
#on a mac, NI-VISA need to by loaded
#(https://stackoverflow.com/questions/66255391
/pyvisa-and-agilent-823578-on-mac/68447825#68447825?newreg=302fb182521c439d96cf5b2db70334e9)

#default initialization of scope
rm = pyvisa.ResourceManager()
#print(rm.list_resources())

#use 'print(rm.list_resources()) to see connected USBs'
oscn = 'USB0::0x1AB1::0x04CE::DS1ZC224104809::INSTR'
scope = rm.open_resource(oscn) #get this name from
```

```
qq=True
signal_chan = [3, 2]
trigg=False

## name
name='TrAT1_'
nfreq='1755'+'MHz'+"_-8␣dBm"

for chan in signal_chan:
    scope.write(':WAV:SOUR␣CHAN' + str(chan))
    scope.write(':WAV:MODE␣NORM')
    # read the waveform data displayed on the screen
    scope.write(':WAV:FORM␣BYTE')
    # a waveform point occupies one byte (namely 8 bits)
    ymult = float(scope.query(':WAV:YINC?'))
    # Query the vertical scale factor
    yzero = float(scope.query(':WAV:YREF?'))
    # Query the waveform conversion factor
    yoff = float(scope.query(':WAV:YOR?'))
    # Query the vertical offset relative to the vertical reference
    position of the specified channel source in the Y direction.
    xincr = float(scope.query(':WAV:XINC?'))
    # Query the time difference between two neighboring points
    of the specified channel source in the X direction.
    xzero = float(scope.query(':WAV:XOR?'))
    # Query the time from the trigger point to the reference time
    of the specified channel source in the X direction.

    # Now you can get data in two modes:
    1. screengrab current data or
    2. screengrab the next trigg
    # If screengrabbing triggers, you can also choose how many you want to grab

    # taking quadrature or not?
```

```
    ADC_wave = [10 for i in range(1200)]
    while ADC_wave[688] == 10:
        scope.write(':WAV:DATA?')
        data = scope.read_raw()
        headerlen = 2 + int(data[1])
        #header = data[:headerlen] #dont need headers
        ADC_wave = data[11:-1] # from headerlen to the end
        ADC_wave = np.array(unpack('%sB' % len(ADC_wave),ADC_wave)) # (format, buffer)
    Volts = (ADC_wave - yoff - yzero) * ymult
    time.sleep(1.5)

    Time = np.arange(xzero, xzero+xincr * len(Volts), xincr)



    all=np.stack((Time,Volts)).T
    x_zero = np.zeros((len(Volts),), dtype=int)

    chan = str(chan)
    tm = time.strftime("%Y-%m-%d␣%H:%M:%S", time.localtime())
    np.savetxt(name+"_"+nfreq+"_"+"CH"+"␣"+chan+'.csv',all,delimiter=',')
    fig = plt.figure(name+"_"+nfreq+"_"+"Channel"+chan)
    plt.plot(Time*1e6, Volts, linewidth=0.5)
    plt.plot(x_zero, Volts, 'y', linewidth=0.2)
    plt.ylabel('Voltage/V')
    plt.xlabel('Time/$\mu$s')
    plt.title(name+"_"+nfreq+"_"+"Channel"+chan)
    plt.show(block=False)

    fig.savefig(name+"_"+nfreq+"_"+"Channel"+chan+".png", dpi=200)

plt.show()
```

Bibliography

[1] Jonathan D. Breeze, Enrico Salvadori, Juna Sathian, Neil Mc N. Alford, and Christopher W.M. Kay. Continuous-wave room-temperature diamond maser. *Nature*, 555(7697):493–496, 2018.

[2] Mark Oxborrow, Jonathan D. Breeze, and Neil M. Alford. Room-temperature solid-state maser. *Nature*, 488(7411):353–356, 2012.

[3] A. Holm, Q. Stürzer, Y. Xu, and R. Weigel. Investigation of surface acoustic waves on LiNbO3, quartz, and LiTaO3 by laser probing. *Microelectronic Engineering*, 31(1-4):123–127, February 1996.

[4] E. A. G. Shaw. On the Resonant Vibrations of Thick Barium Titanate Disks. *The Journal of the Acoustical Society of America*, 28(1):38–50, January 1956.

[5] Stuart Bogatko, Peter D. Haynes, Juna Sathian, Jessica Wade, Ji-Seon Kim, Ke-Jie Tan, Jonathan Breeze, Enrico Salvadori, Andrew Horsfield, and Mark Oxborrow. Molecular Design of a Room-Temperature Maser. *The Journal of Physical Chemistry C*, 120(15):8251–8260, April 2016.

[6] Wern Ng, Xiaotian Xu, Max Attwood, Hao Wu, Zhu Meng, Xi Chen, and Mark Oxborrow. Move Aside Pentacene: Diazapentacene-Doped *para* -Terphenyl, a Zero-Field Room-Temperature Maser with Strong Coupling for Cavity Quantum Electrodynamics. *Advanced Materials*, 35(22):2300441, June 2023.

[7] Max Attwood, Xiaotian Xu, Michael Newns, Zhu Meng, Rebecca Ingle, Hao Wu, Chen Xi, Weidong Xu, and Mark Oxborrow. N-heteroacenes as an organic gain medium for Masers.

[8] J Robert Johansson, Paul D Nation, and Franco Nori. Qutip: An open-source python framework for the dynamics of open quantum systems. *Computer Physics Communications*, 183(8):1760–1772, 2012.

[9] Qilong Wu, Yuan Zhang, Hao Wu, Shi-Lei Su, Kai-Kai Liu, Mark Oxborrow, Chong-Xin Shan, and Klaus Mølmer. Theoretical study of superradiant masing with solid-state spins at room temperature. *Science China Physics, Mechanics & Astronomy*, 67(6):1–10, 2024.

[10] Anthony E Siegman and HJ Hagger. Microwave solid-state masers, 1964.

[11] Liang Jin, Matthias Pfender, Nabeel Aslam, Philipp Neumann, Sen Yang, Jörg Wrachtrup, and Ren-Bao Liu. Proposal for a room-temperature diamond maser. *Nature Communications*, 6(1):1–8, 2015.

[12] Erinn van Wynsberghe and Ayse Turak. Candidate materials as gain media in organic, triplet-based, room-temperature masers targeting the ism bands. *Optoelectronics-Advanced Device Structures*, pages 213–231, 2017.

[13] M Fischer, A Sperlich, H Kraus, T Ohshima, GV Astakhov, and V Dyakonov. Highly efficient optical pumping of spin defects in silicon carbide for stimulated microwave emission. *Physical Review Applied*, 9(5):054006, 2018.

[14] Rodney Loudon. *The quantum theory of light*. OUP Oxford, 2000.

[15] Hermann Haken and Hans Christoph Wolf. *The physics of atoms and quanta: introduction to experiments and theory*. Springer Science & Business Media, 2006.

[16] Alexander Sherman, Oleg Zgadzai, Boaz Koren, Idan Peretz, Eyal Laster, and Aharon Blank. Diamond-based microwave quantum amplifier. *Science Advances*, 8(49):eade6527, December 2022.

[17] Christian Hintze, Ulrich E. Steiner, and Malte Drescher. Photoexcited Triplet State Kinetics Studied by Electron Paramagnetic Resonance Spectroscopy. *ChemPhysChem*, 18(1):6–16, January 2017.

[18] Sabine Richert, Claudia E Tait, and Christiane R Timmel. Delocalisation of photoexcited triplet states probed by transient epr and hyperfine spectroscopy. *Journal of Magnetic Resonance*, 280:103–116, 2017.

[19] Maxie M Roessler and Enrico Salvadori. Principles and applications of epr spectroscopy in the chemical sciences. *Chemical Society Reviews*, 47(8):2534–2553, 2018.

[20] Charles P Poole Jr, Horacio A Farach, and William K Jackson. Standardization of convention for zero field splitting parameters. *The Journal of Chemical Physics*, 61(6):2220–2221, 1974.

[21] Kazuyuki Takeda, K Takegoshi, and Takehiko Terao. Zero-field electron spin resonance and theoretical studies of light penetration into single crystal and polycrystalline material doped with molecules photoexcitable to the triplet state via intersystem crossing ARTICLES YOU MAY BE INTERESTED IN. *J. Chem. Phys*, 117:4940, 2002.

[22] David J. Sloop, Hsiang-Lin Yu, Tien-Sung Lin, and S. I. Weissman. Electron spin echoes of a photoexcited triplet: Pentacene in p-terphenyl crystals. *The Journal of Chemical Physics*, 75(8):3746–3757, 10 1981.

[23] Hao Wu, Wern Ng, Shamil Mirkhanov, Arman Amirzhan, Supamas Nitnara, Mark Oxborrow, Harvard John, and A Paulson. Unraveling the Room-Temperature Spin Dynamics of Photoexcited Pentacene in Its Lowest Triplet State at Zero Field. 2019.

[24] Jonathan D. Breeze, Enrico Salvadori, Juna Sathian, Neil McN. Alford, and Christopher W. M. Kay. Room-temperature cavity quantum electrodynamics with strongly coupled Dicke states. *npj Quantum Information*, 3(1):1–5, 2017.

[25] Daan M. Arroo, Neil McN. Alford, and Jonathan D. Breeze. Perspective on room-temperature solid-state masers. *Applied Physics Letters*, 119(14):140502, October 2021.

[26] Wern Ng, Yongqiang Wen, Neil Alford, and Daan M Arroo. Portable diamond maser with reduced magnetic field through orientation. *arXiv preprint arXiv:2404.05000*, 2024.

[27] Wern Ng, Hao Wu, and Mark Oxborrow. Continuous Cooling of a Microwave Mode on a Benchtop using Hyperpolarized NV$^-$ Diamond. *arXiv:2110.12105 [physics, physics:quant-ph]*, October 2021. arXiv: 2110.12105.

[28] Wern Ng, Hao Wu, and Mark Oxborrow. Quasi-continuous cooling of a microwave mode on a benchtop using hyperpolarized nv- diamond. *Applied Physics Letters*, 119(23), 2021.

[29] Hao Wu. Room-Temperature Quasi-Continuous-Wave Pentacene Maser Pumped by an Invasive Ce:YAG Luminescent Concentrator. 2020.

[30] Mark Oxborrow. Maser assembly, patent no. us9608396b2, 2017. Patent.

[31] Hao Wu, Xiangyu Xie, Wern Ng, Seif Mehanna, Yingxu Li, Max Attwood, and Mark Oxborrow. Room-Temperature Quasi-Continuous-Wave Pentacene Maser Pumped by an Invasive Ce : YAG Luminescent Concentrator. *Physical Review Applied*, 14(6):064017, December 2020.

[32] Howard J. Carmichael. *Statistical Methods in Quantum Optics 1: Master Equations and Fokker-Planck Equations*. Springer Berlin Heidelberg, Berlin, Heidelberg, 1999.

[33] Wern Ng, Yongqiang Wen, Max Attwood, Daniel C Jones, Mark Oxborrow, Neil McN Alford, and Daan M Arroo. "maser-in-a-shoebox": A portable plug-and-play maser device at room temperature and zero magnetic field. *Applied Physics Letters*, 124(4), 2024.

[34] B. A. Auld. *Acoustic Fields and Waves in Solids*. Wiley, New York ;, 1973. Publication Title: Acoustic fields and waves in solids.

[35] Martin V. Gustafsson, Thomas Aref, Anton Frisk Kockum, Maria K. Ekström, Göran Johansson, and Per Delsing. Propagating phonons coupled to an artificial atom. *Science*, 346(6206):207–211, October 2014.

[36] Mark A. Kemp, Matt Franzi, Andy Haase, Erik Jongewaard, Matthew T. Whittaker, Michael Kirkpatrick, and Robert Sparr. A high Q piezoelectric resonator as a portable VLF transmitter. *Nature Communications*, 10(1), 2019.

[37] Jonathan Breeze, Ke Jie Tan, Benjamin Richards, Juna Sathian, Mark Oxborrow, and Neil Mc N. Alford. Enhanced magnetic Purcell effect in room-temperature masers. *Nature Communications*, 6(1):1–6, 2015.

[38] Chin-Chong Tseng. Elastic Surface Waves on Free Surface and Metallized Surface of CdS, ZnO, and PZT-4. *Journal of Applied Physics*, 38(11):4281–4284, October 1967.

[39] James McKenna, Garry D. Boyd, and Robert N. Thurston. Plate Theory Solution for Guided Flexural Acoustic Waves Along the Tip of a Wedge. *IEEE Transactions on Sonics and Ultrasonics*, 21(3):178–186, 1974.

[40] Stepan P. Timošenko and Sergius Woinowsky-Krieger. *Theory of plates and shells*. Engineering societies monographs. McGraw-Hill, New York, 2. ed., reissued edition, 1987. OCLC: 256657700.

[41] Xiaotian Xu, Michael Newns, and Mark Oxborrow. Simulating the magnetic fields generated by piezoelectric devices using FEM software: Beyond the quasistatic approximation. *Journal of Applied Physics*, 132(20):205107, November 2022. Publisher: American Institute of Physics.

[42] Woldemar Voigt. *Lehrbuch der kristallphysik:(mit ausschluss der kristalloptik)*, volume 34. BG Teubner, 1910.

[43] R. D. Mindlin. Electromagnetic radiation from a vibrating quartz plate. *International Journal of Solids and Structures*, 9(6):697–702, June 1973.

[44] Warren Perry Mason. *Physical acoustics and the properties of solids*. van Nostrand, 1958.

[45] Mark Oxborrow. Traceable 2-D finite-element simulation of the whispering-gallery modes of axisymmetric electromagnetic resonators. *IEEE Transactions on Microwave Theory and Techniques*, 55(6):1209–1218, 2007.

[46] Jian-Ming Jin. *The Finite Element Method in Electromagnetics*. Wiley, New York, 2nd ed. edition, 2002.

[47] R. M. White and F. W. Voltmer. Direct piezoelectric coupling to surface elastic waves. *Applied Physics Letters*, 7(12):314–316, December 1965. Publisher: American Institute of Physics.

[48] Chin-Chong Tseng and R. M. White. Propagation of Piezoelectric and Elastic Surface Waves on the Basal Plane of Hexagonal Piezoelectric Crystals. *Journal of Applied Physics*, 38(11):4274–4280, 1967.

[49] F.W. Voltmer, E.P. Ippen, R.M. White, T.C. Lim, and G.W. Farnell. Measured and calculated surface-wave velocities. *Proceedings of the IEEE*, 56(9):1634–1635, 1968.

[50] A. Holm, R. Weigel, P. Russer, and W. Ruile. A laser probing system for characterization of SAW propagation on LiNbO/sub 3/, LiTaO/sub 3/, and quartz. In *1996 IEEE MTT-S International Microwave Symposium Digest*, volume 3, pages 1541–1544, San Francisco, CA, USA, 1996. IEEE.

[51] A.C. Dent, C.R. Bowen, R. Stevens, M.G. Cain, and M. Stewart. Effective elastic properties for unpoled barium titanate. *Journal of the European Ceramic Society*, 27(13-15):3739–3743, January 2007.

[52] Till Biskup. Structure–function relationship of organic semiconductors: detailed insights from time-resolved epr spectroscopy. *Frontiers in Chemistry*, 7:10, 2019.

[53] Aharon Blank and Haim Levanon. Interaction between Polarized Triplets and Stable Radicals in Liquid Solutions. *The Journal of Physical Chemistry A*, 105(20):4799–4807, May 2001.

[54] Aharon Blank and Haim Levanon. Optimal magnetization in liquids, generated by triplet—doublet interaction. *Molecular Physics*, 100(9):1477–1488, May 2002.

[55] Adrian Mena, Sarah K Mann, Angus Cowley-Semple, Emma Bryan, Sandrine Heutz, Dane R McCamey, Max Attwood, and Sam L Bayliss. Room-temperature optically detected coherent control of molecular spins. *Physical Review Letters*, 133(12):120801, 2024.

[56] Kuan-Cheng Chen, Alberto Collauto, Ciarán J Rogers, Shang Yu, Mark Oxborrow, and Max Attwood. Unlocking the potential of photoexcited molecular electron spins for room temperature quantum information processing. *arXiv preprint arXiv:2408.16743*, 2024.

[57] Hideto Matsuoka, Marius Retegan, Lisa Schmitt, Sigurd Höger, Frank Neese, and Olav Schiemann. Time-resolved electron paramagnetic resonance and theoretical investigations of metal-free room-temperature triplet emitters. *Journal of the American Chemical Society*, 139(37):12968–12975, 2017.

[58] Lorenza Viola and Seth Lloyd. Dynamical suppression of decoherence in two-state quantum systems. *Physical Review A*, 58(4):2733, 1998.

[59] E. L. Hahn. Spin echoes. *Phys. Rev.*, 80:580–594, Nov 1950.

[60] Hill Paul, Horowitz Winfield. *The Art of Electronics*. 1962.

[61] David J Ingram. *Spectroscopy at radio and microwave frequencies*. Springer Science & Business Media, 2012.

[62] Harald T Friis. Noise figures of radio receivers. *Proceedings of the IRE*, 32(7):419–422, 1944.

[63] Anna Bychek, Christoph Hotter, David Plankensteiner, and Helmut Ritsch. Superradiant lasing in inhomogeneously broadened ensembles with spatially varying coupling. *arXiv*, 1:73, September 2021. arXiv:2105.11023 [quant-ph].

[64] Michael Tavis and Frederick W. Cummings. Exact Solution for an N -Molecule—Radiation-Field Hamiltonian. *Physical Review*, 170(2):379–384, June 1968.

[65] E.T. Jaynes and F.W. Cummings. Comparison of quantum and semiclassical radiation theories with application to the beam maser. *Proceedings of the IEEE*, 51(1):89–109, 1963.

[66] Christopher C Gerry and Peter L Knight. *Introductory quantum optics*. Cambridge university press, 2023.

[67] Jun John Sakurai and Jim Napolitano. *Modern quantum mechanics*. Cambridge University Press, 2020.

[68] Goran Lindblad. On the generators of quantum dynamical semigroups. *Communications in Mathematical Physics*, 48:119–130, 1976.

[69] Xiaotian Xu. *Simulations of Quantum Spin Dynamics in a Maser Cavity*. PhD thesis, 2020.

[70] Jeff Bezanson, Alan Edelman, Stefan Karpinski, and Viral B Shah. Julia: A fresh approach to numerical computing. *SIAM review*, 59(1):65–98, 2017.

[71] David Plankensteiner, Christoph Hotter, and Helmut Ritsch. QuantumCumulants.jl: A Julia framework for generalized mean-field equations in open quantum systems. *Quantum*, 6:617, January 2022.

[72] Ryogo Kubo. Generalized cumulant expansion method. *Journal of the Physical Society of Japan*, 17(7):1100–1120, 1962.

[73] Myungshik Kim. *Quantum Information – Autumn 2019*. 2020.

[74] Yongqiang Wen, Philip L Diggle, Neil McN Alford, and Daan M Arroo. Exploring the spin dynamics of a room-temperature diamond maser using an extended rate equation model. *Journal of Applied Physics*, 134(19), 2023.

[75] David J Sloop, Hsiang-Lin Yu, Tien-Sung Lin, and SI Weissman. Electron spin echoes of a photoexcited triplet: Pentacene in p-terphenyl crystals. *The Journal of Chemical Physics*, 75(8):3746–3757, 1981.